

Dynamics of laser-induced cavitation bubble during expansion over sharp-edge geometry submerged in liquid – an inside view by diffuse illumination

Matej Senegačnik^a, Kohei Kunimoto^b, Satoshi Yamaguchi^b, Koki Kimura^b, Tetsuo Sakka^b, Peter Gregorčič^{a,*}

^a Faculty of Mechanical Engineering, University of Ljubljana, Aškerčeva 6, 1000 Ljubljana, Slovenia

^b Department of Energy and Hydrocarbon Chemistry, Kyoto University, Nishikyo, Kyoto 615-8510, Japan

ARTICLE INFO

Keywords:

Laser ablation in liquids
Cavitation bubble
Illumination
Shadowgraphy
Nanoparticle production
Re-entrant jet

ABSTRACT

Laser ablation in liquids is growing in popularity for various applications including nanoparticle production, breakdown spectroscopy, and surface functionalization. When laser pulse ablates the solid target submerged in liquid, a cavitation bubble develops. In case of “finite” geometries of ablated solids, liquid dynamical phenomena can occur inside the bubble when the bubble overflows the surface edge. To observe this dynamics, we use diffuse illumination of a flashlamp in combination with a high-speed videography by exposure times down to 250 ns. The developed theoretical modelling and its comparison with the experimental observations clearly prove that this approach widens the observable area inside the bubble. We thereby use it to study the dynamics of laser-induced cavitation bubble during its expansion over a sharp-edge (“cliff-like” 90°) geometry submerged in water, ethanol, and polyethylene glycol 300. The samples are 17 mm wide stainless steel plates with thickness in the range of 0.025–2 mm. Bubbles are induced on the samples by 1064-nm laser pulses with pulse durations of 7–60 ns and pulse energies of 10–55 mJ. We observe formation of a fixed-type secondary cavity behind the edge where low-pressure area develops due to bubble-driven flow of the liquid. This occurs when the velocity of liquid overflow exceeds $\sim 20 \text{ m s}^{-1}$. A re-entrant liquid injection with up to $\sim 40 \text{ m s}^{-1}$ velocity may occur inside the bubble when the bubble overflows the edge of the sample. Formation and characteristics of the jet evidently depend on the relation between the breakdown-edge offset and the bubble energy, as well as the properties of the surrounding liquid. Higher viscosity of the liquid prevents the generation of the jet.

1. Introduction

The field of laser ablation in liquids (LAL) has exhibited significant development since the beginning of the 21st century due to its implementation in a broad range of applications, including laser-induced breakdown spectroscopy [1–3], surface functionalization [4–7], and nanoparticle production [8–11]. Although numerous studies have been devoted to clarification of the laser-induced cavitation bubble dynamics, some aspects of bubble development and nanoparticle formation still remain poorly understood. In this context, some authors suggest that the nanoparticles are generated in the liquid environment outside of the bubble [12], while others propose that they form inside the bubble during its expansion phase [13].

Most of the studies consider the dynamics of bubbles that are induced in infinite [14,15] and semi-infinite liquid environments (i.e., containing a large flat liquid/solid [16,17] or liquid/liquid [18,19] interface). In case of laser-induced breakdown near a solid (rigid) boundary that is immersed into liquid, the cavitation bubble collapses asymmetrically and multiple reports of liquid injections inside the cavitation bubble can be found in the literature [16–18,20–23]. Extensive studies of this phenomenon were mainly performed to improve the understanding of the prevalent mechanism that is responsible for damage caused by cavitation [24,25]. Bubbles in these studies were thereby induced in close proximity of an “infinitely” large flat rigid surface. In this case, a liquid jet with “tip” velocity in the order of 100 m s^{-1} develops towards the solid surface during the collapse phase. The formation of the jet is

Abbreviations: PEG, polyethylene glycol.

* Corresponding author.

E-mail address: peter.gregorcic@fs.uni-lj.si (P. Gregorčič).

<https://doi.org/10.1016/j.ultsonch.2021.105460>

Received in revised form 21 October 2020; Accepted 28 December 2020

Available online 9 January 2021

1350-4177/© 2021 The Author(s). Published by Elsevier B.V. This is an open access article under the CC BY license (<http://creativecommons.org/licenses/by/4.0/>).

generally explained by reduced bubble wall velocity adjacent to the rigid surface [20]. Recent studies also show that the evolution of the cavitation bubble and its collapse can be additionally influenced by the geometry of the solid surrounding the breakdown [26,27]. Specifically, it was demonstrated that ablation of unconventional deformable geometry, such as a thin wire [28], results in a “spring board” effect [29], so that the collapse of the laser-induced cavitation bubble takes place away from the irradiated surface [30]. In this case, an increased nanoparticle productivity was reported [31] and explained by the decreased redeposition of laser-generated nanoparticles to the donor surface during the bubble collapse.

One of the most common and straightforward methods used to study cavitation bubbles in the aforementioned studies is shadowgraphy [14,18,32–36]. Here, the main idea is to illuminate the bubble from the back and thereby cast its shadow onto an imaging sensor, which is usually in form of an industrial or high speed camera. Since the bubble wall is essentially a liquid-gas interface that separates two phases with different optical densities, the direction of illuminating light is altered upon crossing this interface. This effect is conveniently utilized by imaging techniques including schlieren photography [17,37,38] and laser-beam deflection [39–42] or transmission [36,43] probes, which acquire the signal based on the refractive index gradient. These methods enable fairly uncomplicated tracking of the overall bubble dynamics (i.e., observation of the movement and shape of its wall). However, for capturing the liquid dynamics *inside* the cavitation bubble (e.g., liquid injections and particle movement), different optical densities at the liquid-gas interface forming the bubble wall prove undesirable as significant amount of illuminating light incident on the bubble wall is deviated out of the objective’s aperture. This can be overcome by using X-ray illumination, since the real part of the refractive index of liquid and vapor is not drastically different for this part of the light spectrum. Thus, time resolved X-ray techniques including radiography [44] and small-angle X-ray scattering [13,45] have been implemented in the studies of laser nanoparticle formation in liquids due to their good selectivity for condensed phases and high atomic weight materials [46]. This is specifically suitable for determining the presence, location, and size of noble metal nanoparticles. On the other hand, the disadvantage of these methods lies in the relatively weak signal during the measurements. Longer exposure times and/or averaging of many repetitions, therefore, need to be implemented, resulting in decreased temporal and spatial resolution of the acquired images.

The first aim of this paper is to show that a diffuse light source in the visible spectrum can be used to cope with the reflection and refraction of the illuminating light at the bubble wall. Our results prove that a diffuse light source increases the amount of light that is “transmitted” through the bubble. This widens the observable area inside the bubble and enables the tracking of *internal* liquid dynamics. For better understanding of the bubble imaging with visual light illumination, the first part of this paper is dedicated to a theoretical and experimental comparison of different illuminating conditions and their effects on perception of the cavitation bubbles.

Several studies have already demonstrated that using (unconventional) thin samples with 100 μm –1 mm thickness [27–31] for ablation can prove beneficial to nanoparticle production by altering the bubble oscillation dynamics. In this case, if the maximum diameter of the laser-induced cavitation bubble is larger than the size of the irradiated solid

surface (bubbles induced by laser pulses with pulse energy in the range of several mJ are often of millimeter-size [14]), bubble overflow of the sample is inevitable. Thus, the second aim of this study is to gain a more detailed insight into dynamics following such “enwrapping” of a solid by a cavitation bubble. In the second part of this paper, we focus on phenomena that occur when the bubble expands over a sharp rigid edge. Instead of irradiating a conventional “infinitely” large flat solid surface, the irradiated samples exhibit a “cliff-like” 90° edge distanced 12.5 μm –1.7 mm away from the position of optical breakdown. Subsequent dynamics is observed from different sides. With implementation of appropriate diffuse illumination, the liquid dynamics *inside* the bubbles is monitored and evaluated. As the laser-induced cavitation bubble expands over the sharp edge of the solid surface, re-entrant injection of liquid into the bubble is captured by using high-speed videography. Our results also reveal a secondary cavity that is developed behind the sharp edge due to low pressure area formed as a result of bubble-driven flow of the surrounding liquid. To clarify the effects of liquid properties on formation and characteristics of the jets and cavities, the experiments are performed in water, ethanol, and polyethylene glycol 300.

2. Experimental

2.1. Materials and liquids

The cavitation bubble was induced by focusing a nanosecond laser pulse on the top face of a stainless-steel (SS) sample in close proximity to a “cliff-like” 90° solid edge (see Fig. S1). Dimensions of the samples equaled $\sim 17 \times 6 \text{ mm}^2$ (width \times height) with thicknesses ranging from 25 μm to 2 mm. During irradiation, samples were submerged into water, ethanol, or polyethylene glycol 300 (PEG) approximately 10 mm below the liquid surface. The most relevant physical properties of the liquids used in the experiments are presented in Table 1.

The ablated surface of the sample was parallel to the liquid surface (see Fig. S1). The distance between breakdown position and the sharp edge, l , was varied by changing the position of the laser spot on the sample surface, as schematically shown in Fig. S1. Chemical composition of the samples was analyzed after the experiments using an X-ray fluorescence spectrometer (Thermo Scientific Niton XL3t GOLDD+) and is shown in Table 2 along with the corresponding sample thickness.

2.2. Setups for measuring bubble dynamics

Two different experimental setups, one with diffuse flashlight illumination and another with collimated ps-laser-light illumination were used to observe the shock wave and bubble dynamics as well as the dynamics of re-entrant liquid injection that may appear when the bubble expands over the edge of the sample.

Setup for cinematography by diffuse illumination is shown in Fig. 1a, and is labeled as experimental setup #1. It was built and located at the Department of Energy and Hydrocarbon Chemistry, Kyoto University (Japan). As an excitation source we used a Nd:YAG laser with 1064 nm wavelength and pulse duration (FWHM) of 60 ns. The pulses with energy between 10 mJ and 55 mJ were reflected off a hot mirror to enable simultaneous observation of the sample from the top by a CMOS camera (Ximea, MQ022MG-CM, 2048 \times 1088 pixel) for positioning. Two photographic flashes with $\sim 1 \text{ ms}$ light pulse (the temporal intensity

Table 1
Properties of liquids (at 20 °C) used in the experiments.

Liquid	Density /g mL ⁻¹	Kinematic viscosity /mm ² s ⁻¹	Vapor pressure /Pa	Refractive index ($\lambda = 532 \text{ nm}$)
Water [47,48]	0.998	1.00	2.34×10^3	1.334
Ethanol [49–51]	0.789	1.44	5.89×10^3	1.361
PEG 300 [52]	1.124	~ 85	<1	1.465

Table 2
Thickness and chemical composition of the SS samples used in the experiments.

Sample	Thickness d /mm	Chemical composition /wt.%							
		Cr	Ni	Mn	Cu	Mo	V	Si	Fe
S1	0.025	16.0	10.5	1.5	0.35	1.5	0.09	0.50	balance
S2	0.38	18.5	8.1	1.7	0.51	0.38	0.13	0.30	balance
S3	1.0	17.3	8.8	0	0.21	0.1	0.1	2.98	balance
S4	1.6	16.8	10.0	1.8	0.41	2.1	0.11	0.52	balance
S5	2.0	15.3	0.28	0.69	0	0	0	0	balance

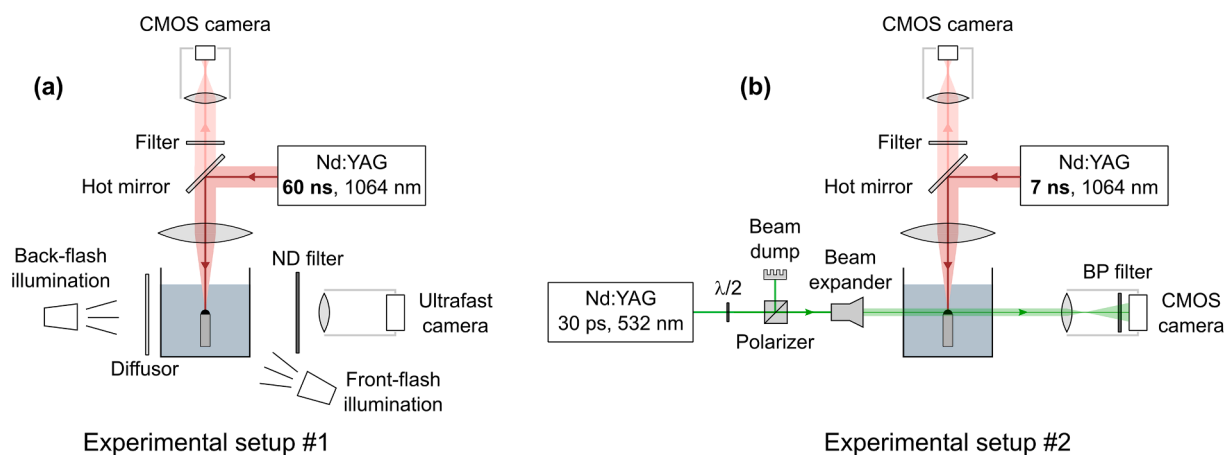


Fig. 1. Experimental setups for (a) cinematography by diffuse illumination and for (b) ultrashort shadowgraphy by collimated illumination.

profile is shown in Fig. S2), one from the back and another from the front were used for illumination. A diffuser was placed between the back illumination source and glass cuvette for a more homogenous and diffuse illumination. The bubble dynamics was captured by an ultrafast camera (Shimadzu HPV-2A with Mitutoyo MY10X-803 objective) at 500 kHz frame rate and shutter time of 250 ns. A neutral density (ND) filter was also implemented in front of the objective to reduce overexposure due to bright plasma.

This kind of high-speed cinematography enables the capturing of the whole bubble dynamics within a single shot, but with temporal resolution of only 250 ns, which does not allow to measure some very fast phenomena, such as initial bubble dynamics or a shock wave. As will be theoretically explained in the next section, the diffuse illumination is essential for seeing phenomena *inside* the cavitation bubble.

Setup for ultrashort shadowgraphy by collimated illumination is shown in Fig. 1b, and is labeled as experimental setup #2. It was developed and located at the Faculty of Mechanical Engineering, University of Ljubljana (Slovenia) to measure the very early stage ($<3 \mu\text{s}$) of the bubble expansion, where the bubble wall velocity exceeds 100 m s^{-1} . A Nd:YAG laser with 1064 nm wavelength and 7-ns pulses (FWHM) with energy of 10.6 mJ was used as an excitation source. Since the exposure time of the ultrafast camera used for the cinematography within experimental setup #1 is not sufficient to obtain sharp images with resolution below micrometer per pixel, the second harmonic ($\lambda = 532 \text{ nm}$) of another Nd:YAG laser (Ekspla, Lithuania, PL2250-SHTH) with pulse duration (FWHM) of 30 ps was used for illumination. The images were captured by a CMOS camera (Ximea, MQ013MG-ON, 1280×1024 pixels with Ricoh FL-CC5028-2 M objective) with long exposure ($\sim 1 \text{ ms}$), similarly as already described in Ref. [53]. An attenuator, consisting of a half-wave plate ($\lambda/2$), polarizing beam-splitter, and a beam dump, was used to set the appropriate intensity of the illumination that was led through a beam expander to enable homogeneous illumination of the observed area. A narrow band-pass (BP) filter ($532 \pm 10 \text{ nm}$) was placed between the objective and the camera to minimize the irradiation emitted by the laser-induced plasma. Here, the exposure time is defined by the duration of illumination pulse, while the delay between optical

breakdown and time of illumination is set by the delay between triggering signals from the signal generator (Tektronix, US, AFG 3102, 1GS/s, 100 MHz) for excitation and illumination lasers. The jitter of this synchronization equals $\pm 0.3 \mu\text{s}$, since the excitation laser is passively Q-switched. Thus, the accurate delay between the excitation and illumination pulse was measured by using two photodiodes with 1 GHz bandwidth.

Ultra short exposure time enables the capturing of fast laser-induced phenomena, such as shock waves, but only one image can be acquired from an individual breakdown event. Considering the speed of sound in water (1.5 km s^{-1}), the theoretical spatial resolution with 30-ps illumination equals $0.05 \mu\text{m}$. However, this approach requires multiple shots to acquire the whole bubble dynamics at different times after the optical breakdown, which calls for high repeatability of the observed phenomena.

3. Role of illumination diffusivity in bubble imaging

Optical observation of cavitation bubbles is important for studying acoustic [21,54], hydrodynamic [55,56] and laser-induced cavitation [14,18,40,43,57,58], as well as to develop different applications including nanoparticle production [8,9,28,30], underwater breakdown spectroscopy [59], enhanced heat transfer with nucleate boiling [60], refrigeration [61,62], microfluidics [63] and laser biomedical procedures [64]. Understanding the influence of illumination on their perception and interpretation can sometimes prove difficult, since it involves refraction and multiple reflection of light at the interface of media with different optical densities. This section is, therefore, dedicated to a theoretical insight into illumination of a spherical bubble with light sources of different diffusivity. As will be shown, the increased diffusivity is essential for observing liquid injections *inside* the cavitation bubble.

The magnification, resolution, depth of field, and the measuring range of the image acquired by the sensor depend on the properties and relationship between the object, objective lens, and the imaging sensor (schematically presented in Fig. 2). However, special care should be

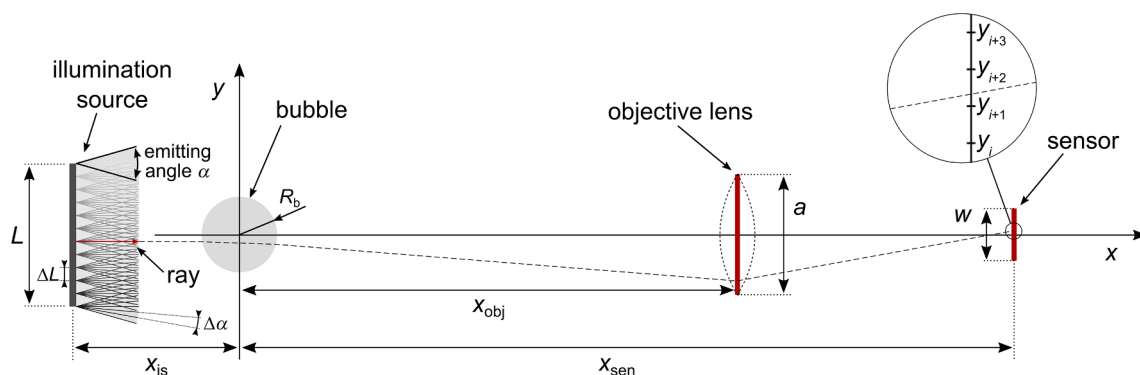


Fig. 2. Numerical modeling of illumination in bubble imaging.

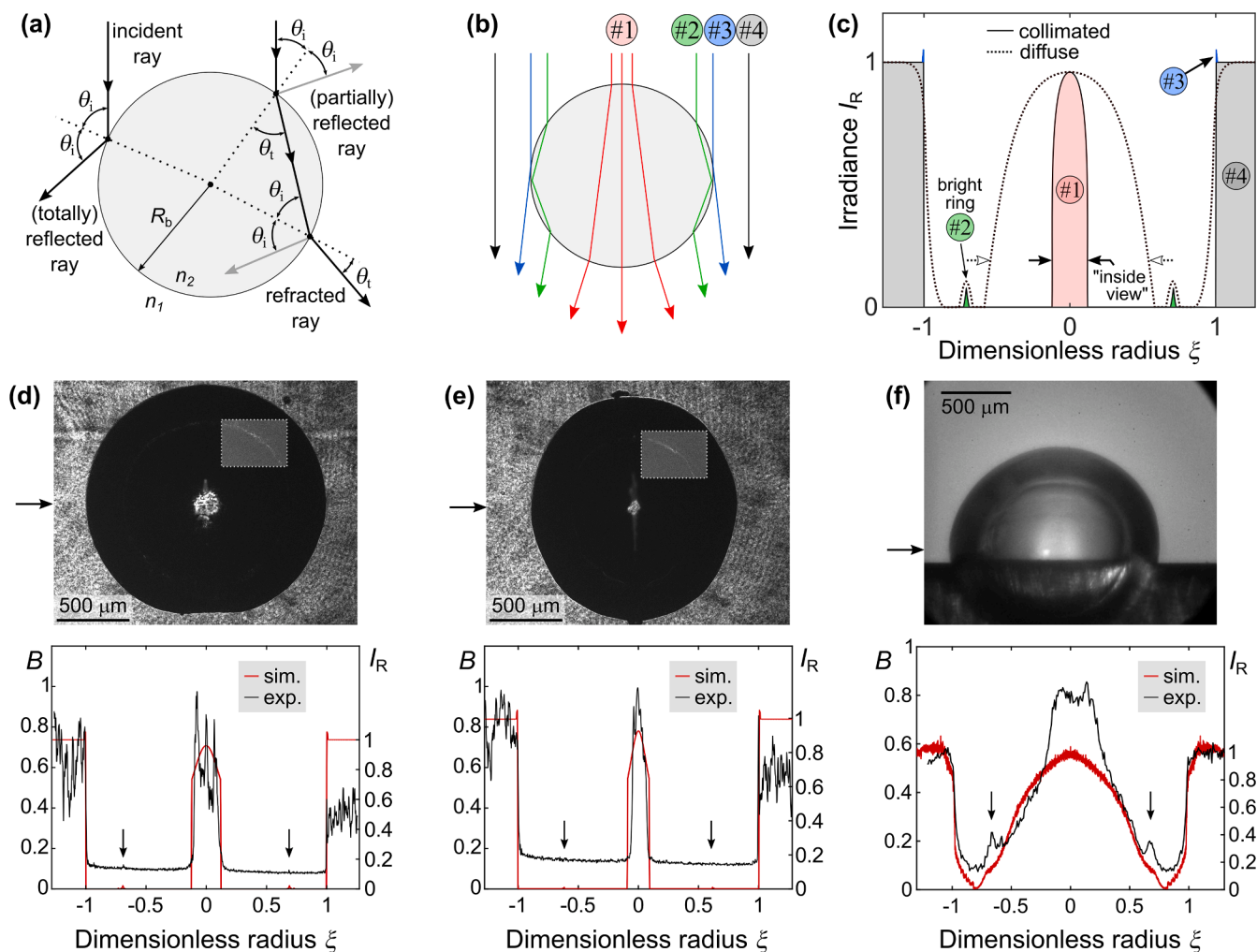


Fig. 3. (a) Reflection and refraction of rays at the bubble wall. Angles of incidence and refraction are denoted by θ_i and θ_t , respectively. (b) Different types of illuminating rays in a vapor bubble with (c) schematically shown corresponding contribution to irradiance profile. (d)–(f) Images of laser-induced cavitation bubbles acquired by experimental setup #2 in (d) water ($n = 1.33$) and (e) PEG ($n = 1.465$) and by (f) experimental setup #1 in water. The arrows on the left-hand side of the acquired images mark the position of the (experimental) irradiance profile in the corresponding bottom graphs, which compare simulation results with experiments. Image brightness B is relevant to experimental profiles, while irradiance I_R is relevant to simulated profiles.

taken when observing media that are transparent for illumination spectrum and contain interfaces between different optical densities [65]. One of such examples is observing two phase phenomena, where the interface between the solid-liquid and/or liquid-gas environment alters the direction of light rays due to light reflection and refraction at the interface, as depicted in Fig. 3a. The perception of such phenomena

is, therefore, not as straightforward and requires proper interpretation [66].

Illumination of a bubble for capturing its image by a digital sensor can be modeled as sketched in Fig. 2. Here, the illumination source is located at a distance x_{is} from the bubble center. The source of dimension L is modeled by discrete point sources (separated by ΔL), each of them

radiating rays within an emitting angle α . The emitting angle is discretized by intervals of $\Delta\alpha$. When α equals zero, the light source is considered *collimated*. The rays from the illumination source are gathered by an objective lens, located x_{obj} from the bubble center, where the lens dimension a represents its aperture. An image is acquired by a digital sensor, positioned in the image plane at x_{sen} from the bubble center. Numerical values of these parameters, considered in the model, are listed in Table S1 of the Supporting Information.

Even a seemingly simple example of illuminating a *static* vapor bubble that floats inside liquid environment proves difficult to describe analytically due to high complexity of the problem [65]. We, therefore, developed a numerical ray tracing model (Fig. 2 and Section S2 of the Supporting Information) based on the laws of geometrical optics to demonstrate and clarify the effect of illumination on perception of cavitation bubbles. Assuming cylindrical symmetry with respect to the optical axis, the problem is reduced to a plane. The cross-section of the vapor bubble is defined as a circle, while the starting illuminating rays are represented by coplanar lines with desired direction (within emitting angle α). Irradiance profile that reaches the sensor is then approximated for different illumination sources considering (total and partial) reflection and refraction of rays at the liquid-gas interface. Intensity of the rays is determined by Fresnel equations [Eqs. (S8)–(S10)].

The bubble with radius R_b is assumed to contain vapor with refractive index $n_2 = 1$, while the liquids considered in the simulations are water and PEG with refractive indices $n_1 = 1.33$ and $n_1 = 1.465$, respectively. The assumptions and basic principles of the model are presented in higher detail in Section S2 of the Supporting Information.

Fig. 3b and c schematically show the contribution of different types of incident rays to the irradiance profile in case of a collimated ($\alpha = 0^\circ$, solid line) and diffuse (dotted line) illumination source. Illumination rays can be generalized as:

- *type #1 rays* that travel through the bubble and are refracted twice – when entering and when exiting the bubble;
- *type #2 rays* that are reflected inside the bubble (also more than once, as schematically shown in Fig. 3b);
- *type #3 rays* that are reflected at the outer bubble wall; and
- *type #4 direct rays* that do not intersect the bubble.

At this point, it is helpful to define irradiance on the sensor I_R as the incident irradiance normalized by the average irradiance of the illumination source. Irradiance I_R of the image background should, therefore, equal 1. Furthermore, for clearer explanation of the observed image, it is convenient to introduce the dimensionless radius ξ from the sensor's center as the distance from the sensor's center y normalized by the bubble radius in the image plane R_{bi}

$$\xi = \frac{y}{R_{\text{bi}}} \quad (1)$$

where R_{bi} can be easily calculated as a product of bubble radius R_b and optical magnification of the system M .

As can be seen from Fig. 3c, each of the four generalized rays contributes to a specific part of the irradiance profile, shown in further detail in Fig. S9. Rays that do not intersect the bubble (type #4) form the bright background around the bubble image ($|\xi| > 1$). Considering merely type #4 rays, the emitting angle α of the illumination source (in combination with the objective's aperture a) influences the gradient of irradiance profile at the bubble wall, i.e. around $|\xi| = 1$. As the emitting angle α is increased (i.e., the illumination is turned from collimated towards diffuse; dotted line in Fig. 3c), the bubble wall becomes blurred (e.g., see also image in Fig. 3f) due to rays traveling beside the bubble wall not collinearly with the optical axis.

Rays that reflect at the outer bubble wall (type #3) also contribute to the irradiance profile around $|\xi| = 1$. In case of a collimated source ($\alpha = 0^\circ$), these rays result in a slight increase of irradiance at the outer side

of the bubble interface ($|\xi| > 1$), albeit the effect is not very pronounced as the collimated rays are quickly reflected out of the aperture of the objective lens. However, as the emitting angle α of the source is increasing, more of these reflected rays reach the sensor, leading to increased irradiance also at $|\xi| < 1$ (further detail in Figs. S11 and S12). In this way, the perceived bubble appears smaller [65], which should certainly be considered when the accurate determination of bubble size is the target.

Rays that reflect inside the bubble (type #2) result in appearance of a bright ring inside the bubble. The position of the ring with respect to bubble wall depends on the ratio of refractive indices outside and inside the bubble n_1/n_2 . Increasing this ratio causes the ring to appear closer to the bubble center, while increasing the source emitting angle α makes the ring wider.

Finally, the rays that travel through the bubble without reflection (type #1) manifest as bright area in the center of the bubble. These rays are crucial for observing phenomena that occur *inside* the vapor/cavitation bubbles. The diameter of the central illuminated area or “inside view”, schematically marked by horizontal arrows in Fig. 3c, depends both on the ratio of refractive indices, as well as on the emitting angle of the illumination source α (in combination with objective's aperture a). In case of collimated source, such as a laser, this diameter is fairly small compared to the radius of the bubble (pink area in Fig. 3c), making observations of fluid dynamics inside the bubble practically impossible. On the contrary, using a diffuse source such as a flashlamp enables the light to enter the bubble at various angles, which significantly increases the observable area inside the vapor bubble.

Modelling of the bubble illumination was validated by comparison of the theoretical and experimental results, shown in Figs. 3d–f. Experimental setup #2 with collimated ps-laser illumination was used to capture images in Figs. 3d, e, while experimental setup #1 with a diffuse light source (utilized by a photographic flash with significantly wider emitting angle and a diffusor) was used for acquiring the image in Fig. 3f. The experimental profiles (black curves in Figs. 3d–f) show image brightness B (left-hand scale on y axes) calculated by normalizing the average brightness value of 5 consecutive lines of pixels (locations marked by horizontal arrows in Figs. 3d–f) with 255, since the images were captured in 8-bit gray scale. This yields brightness B ranging from 0 (black) to 1 (white). These profiles are compared to the simulated irradiance I_R , where a value of 1 represents the irradiance of illumination source – background.

To show the effect of liquid's optical density, water (Fig. 3d) with refractive index 1.33 and PEG (Fig. 3e) with refractive index 1.465 were used in the experiments. Influence of the emitting angle of the light source was determined in water, shown in Fig. 3f (with simulated emitting angle $\alpha = 46^\circ$). Bubbles in Figs. 3d and e were produced in infinite liquid, while the bubble in Fig. 3f was induced on a thin metal sample.

In case of collimated illumination (Figs. 3d, e), the experiments agree with the theoretical simulation very well. The increased noise of the background compared to flash illumination is due to coherence of the laser beam leading to interference effects forming a speckle pattern. Irradiance of the background is decreasing from left to right, as the illuminating laser beam was not perfectly aligned with the optical axis of the imaging system. The measured irradiance of the background (at $\xi \gg 1$), therefore, differs from the predicted profile, as the model does not account for this. Bright rings that arise from reflections inside the bubble (due to type #2 rays), indicated by vertical arrows in Figs. 3d–f, are detected and their position with respect to the bubble wall is theoretically predicted. For better visibility of the ring, a (rectangular) part of the bubble in Figs. 3d and e is brightened and increased in contrast. The brightness of the ring is fairly dependent on the reflectivity at the bubble wall, since it arises from the rays that reflect inside the bubble (type #2).

Governed by Fresnel relations [Eqs. (S8)–(S10)], reflectivity depends on angles of incidence and refraction, as well as orientation of illuminating-light *polarization* with respect to the plane of incidence. As

shown in Section S2 of the Supporting Information (Fig. S10), linear polarization of the illuminating source leads to symmetrical brightness variation of the ring, while background and central illuminated area of the bubble remain fairly similar. The size of the central illuminated area inside the bubble (area #1 in Fig. 3c) also fits the model well. One can see that higher optical density of the liquid (Fig. 3e) decreases the diameter of this area compared to lower optical density (Fig. 3d), while the appearance of the bright ring moves closer to the bubble center. By using collimated illumination in experimental setup #2, the peak of the bright ring (indicated by vertical arrows in Figs. 3d and e) is detected at $|\xi| \sim 0.69$ in water and at $|\xi| \sim 0.61$ in PEG.

On the contrary, it is much harder to closely predict the theoretical irradiance profile in case of diffuse illumination due to difficult characterization of the illuminating source. Albeit the diffusor being placed between the flash and the bubble, the illumination is not homogenous and equally radiant in all angles, which is the model assumption. Furthermore, reflections from surroundings including glass cuvette walls as well as object surfaces outside the cuvette are significantly greater compared to collimated laser illumination, but neglected in the simulation for sake of simplicity. Nevertheless, we have found that the bright ring from reflections inside the bubble forms in the same position, but is wider compared to laser illumination.

The most important conclusion that follows from the described

theoretical modelling of illumination is the confirmation that the bright (i.e., illuminated) central area of the bubble, that is crucial for observation of the phenomena *inside* the bubble, increases by increasing the illumination source diffusivity that is characterized by the emitting angle. Thus, diffuse illumination enables observations of the dynamics of liquid jets inside the bubble (e.g., that occur when the cavitation bubble expands over a sharp edge) with high spatial and temporal resolution.

4. Results and discussion

When a high-intensity laser pulse hits the solid-liquid interface (here, it is assumed that the liquid is dielectric and transparent for the excitation-laser light), part of the light is reflected, while the rest is absorbed in the solid. Reflection and absorption depend on the polarization of light, angle of incidence, and refractive indices of the solid target and the liquid. The absorption occurs within a solid-surface layer of thickness that equals the optical penetration depth, defined as $\delta_p = \lambda/4\pi\kappa$. Here, κ and λ stand for the extinction coefficient of the solid and the wavelength of light, respectively. In metals, the laser beam is absorbed within the skin layer, since the optical penetration depth for metals (at $\lambda = 1064$ nm) typically ranges from ~ 10 nm to ~ 20 nm.

The interaction between a nanosecond laser pulse and solid metal results in photon coupling of the electronic and vibrational modes of the

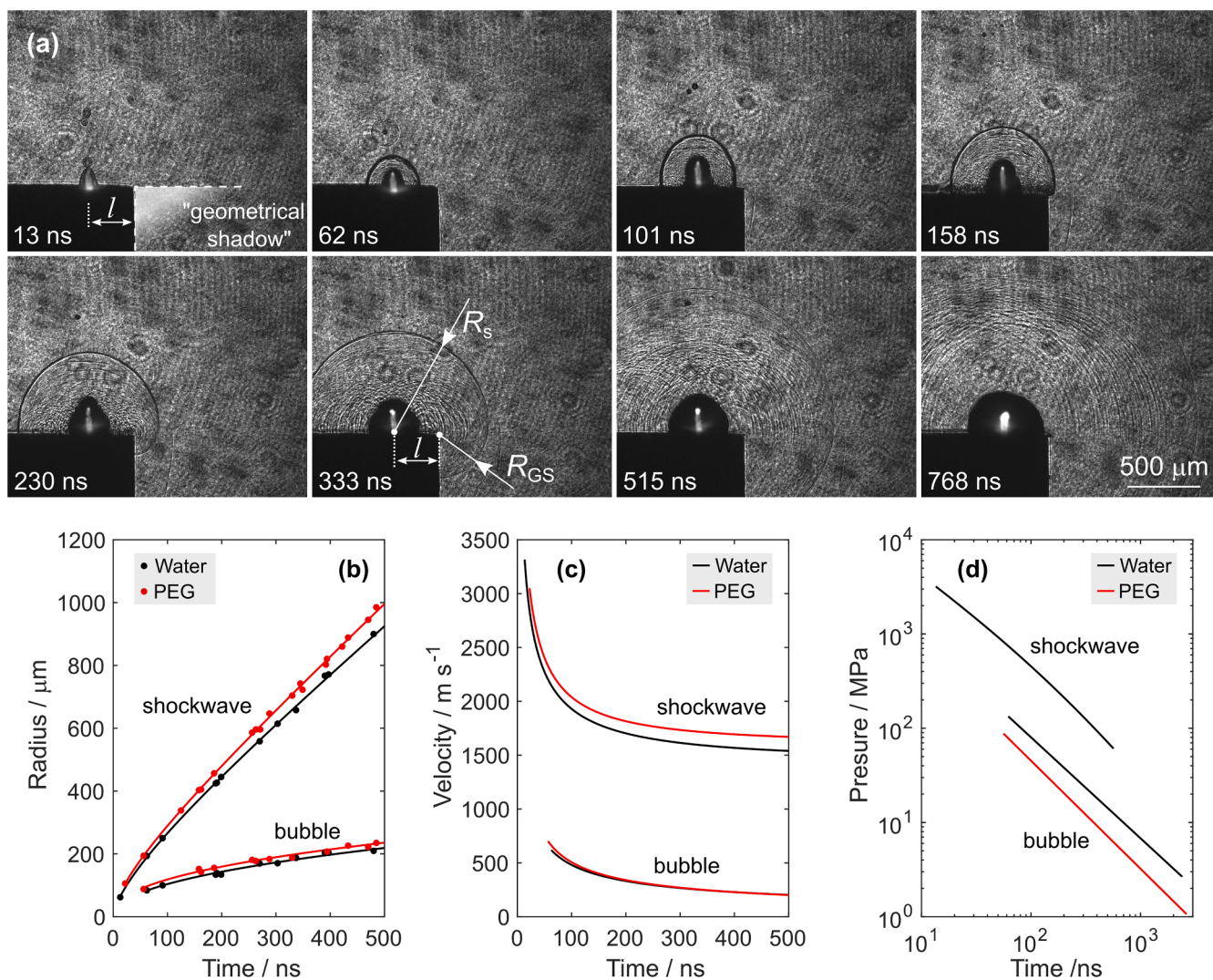


Fig. 4. (a) Evolution of the shockwave in water after breakdown of stainless steel at $l = 0.3$ mm from the edge (experimental setup #2). Geometrical shadow in the first image is intentionally and artificially white-blurred. Temporal profiles of shockwave and bubble wall (b) radius, (c) velocity, and (d) pressure after laser induced breakdown in water and PEG.

target material [67]. The electron–electron coupling leads to increased electron temperature and vaporization of the transiently heated target followed by the expansion of the evaporated atoms, ions, and electrons [68]. The surrounding liquid confines the vapor plume, while the remaining part of the excitation nanosecond-laser pulse further vaporizes the target material, generates additional hot electrons by the absorption of photons, and heats the nascent plasma by inverse Bremsstrahlung [9]. Thus, the plasma plume contains neutral atoms, ions, and electrons from the solid target. The strong confinement by liquid environment results in plasma that is characterized by temperatures of several thousand Kelvins and high pressures up to 10^9 Pa. The laser-induced plasma adiabatically expands at a supersonic velocity and due to liquid confinement generates a shock wave that propagates into the liquid [69] (see also Figs. 4a and S13), while the recoil during plasma expansion generates an elastic ultrasonic wave within the solid target [70,71].

As the plasma cools down, it undergoes a phase transition into vapor (cavitation bubble) followed by liquid phase. However, the mechanisms of this transition still remain unclear [9]. At the beginning (<200 ns after the excitation pulse), the cavitation bubble is elongated with the shape similar to the plasma plume outline (see Figs. 4a and S13). When the bubble is induced on a flat target surface, its shape later takes an approximately hemispherical form. If the distances between the bubble center and the edges of this flat surface are significantly larger than the maximum radius of the bubble ($R_{b,max} \ll l$), the bubble expands, collapses, and rebounds several times (typical oscillation time for the bubble induced by ns pulse of several mJ is in the range of several hundred microseconds) and usually ends with long-life (i.e., in the millisecond to second range) persistent microbubbles remaining above the solid surface [9]. In case of irradiating a flat metal surface, the light-to-bubble conversion efficiency is highest when the excitation-beam focus is positioned slightly below the target surface [26]. However, the aim of our experiments is to observe the dynamics when bubble radius is comparable to or larger than the distance between the bubble center and the edge ($R_{b,max} > l$), resulting in bubble overflowing the edge of the solid surface (see Fig. S1).

4.1. Initial evolution of the shockwave and cavitation bubble

The dynamics of the shock wave and cavitation bubble during the initial several microseconds following optical breakdown in close proximity (distance l) to the edge was evaluated using the experimental setup for ultrashort shadowgraphy (experimental setup #2). Since this setup allows acquisition of laser-induced phenomena only in a single time instance, multiple events at different time intervals after the excitation pulse were captured to obtain a temporal evolution. Typical sequence of images with a clearly visible shock wave and cavitation bubble within first eight hundred nanoseconds in water is shown in Fig. 4a, while Fig. S13b shows typical images for PEG (the raw data are available in Ref. [72]).

The measured radii of the observed phenomena as a function of time after irradiation are presented by the dots in Fig. 4b (and Figs. S14 and S16). They were obtained by fitting a circle to the acquired images with $1.6 \mu\text{m}/\text{px}$ resolution. Curves (solid lines in Fig. 4b) defined by Eqs. (S12) and (S15) were fit to discrete experimental measurements of radii in order to obtain continuously derivable functions. The corresponding velocity profiles could then be calculated by simple derivation of these functions (see details in Section S3 of the Supporting Information).

As visible from Figs. 4c and S15, shockwaves in both liquids propagate supersonically with velocity exceeding 2 km s^{-1} at 50 ns after optical breakdown. By time, shockwave velocity converges to the speed of sound, which can be estimated in both liquids as a fitting parameter in Eq. (S12) (see also Table S2). We estimated the shockwave velocities to 1.4 km s^{-1} for water and 1.6 km s^{-1} for PEG. These results are in good agreement with the values reported in the literature, i.e., 1483 m s^{-1} for water [73] and 1615 m s^{-1} for PEG [74].

Velocity of the shockwave propagation was also investigated in the “geometrical shadow” (see the intentionally shaded area in Fig. 4a at 13 ns). Here, the measuring range is $<0.5 \text{ mm}$ (i.e., the distance from the sample edge to the bottom of the captured images), while the shockwave velocity is in the order of 1.5 km s^{-1} . Thus, the shockwave front in the “geometrical shadow” is observable only within a very narrow time gap of $\sim 0.3 \mu\text{s}$, which is difficult to obtain with the jitter of experimental setup #2. Therefore, from the acquired images we can only roughly estimate that the velocity remains similar to the remaining (i.e., outside the geometrical shadow) part of the shockwave. However, the curvature radius of the part of the shockwave front that propagates in the geometrical shadow, R_{GS} (see definition in Fig. 4a), is smaller than the radius of the (remaining) shockwave R_s due to breakdown being induced away from the edge. The absolute difference in these radii is constant with time and equals approximately the distance between the breakdown spot and sample edge, i.e., $R_s - R_{GS} \sim l$ (see Fig. 4a at 333 ns).

Bubble velocity is difficult to determine during the first 50 ns after the breakdown, as the interface between liquid and vapor is not yet clearly defined due to supercritical state of the liquid. After expansion, when the temperature and pressure decay lead to transition from supercritical to gaseous (vapor) state, bubble wall forms. The first measurable velocity (at 65 ns after optical breakdown) was estimated to 600 m s^{-1} for water and 650 m s^{-1} for PEG (Figs. 4c and S17). It should be noted, that more precise velocity measurements could be collected by using two or more consecutive laser pulses for multi exposure of the shockwave/bubble within several nanoseconds (e.g., by using similar approach as described in Ref. [35]).

As has been shown by Vogel et al., there is a strong correlation between the shockwave velocity u_s and the shockwave pressure p_s , which can be described by the following relation [14].

$$p_s = c_1 \rho_0 u_s (10^{(u_s - c_0)/c_2} - 1) + p_0 \quad (2)$$

In Eq. (2), c_0 stands for the local speed of sound and was determined from the fit [Eq. (S12)], while p_0 is the ambient pressure of the liquid (assumed to be 100 kPa). For water, constants c_1 and c_2 equal 5190 m s^{-1} and 25306 m s^{-1} [14], respectively. The constants c_1 and c_2 were obtained by Rice and Walsh [75] from the Rankine-Hugoniot relations and an analytical fit of the experimental Hugoniot curve data for water. Due to lack of these constants for PEG, shockwave pressure was only estimated for water and is shown by the black curve in Fig. 4d. As the velocity approaches the speed of sound, the shockwave converts into an acoustic wave and its pressure decreases towards the ambient pressure of the liquid.

The bubble dynamics for incompressible and nonviscous liquid can be described by the Rayleigh-Plesset equation that is derived from the continuity equation and the Navier-Stokes equation as [76]

$$\Delta p = \rho_0 \left(\frac{3}{2} \dot{R}_b^2 + R_b \ddot{R}_b \right) \quad (3)$$

In Eq. (3), R_b stands for the bubble radius as a function of time, dot represents a time derivative, and ρ_0 is the density of the liquid. The pressure difference at the bubble wall Δp equals

$$\Delta p = p_b - p_0 \quad (4)$$

where p_0 denotes the pressure of the surrounding liquid and p_b is the pressure at the bubble wall that can be expressed by the bubble vapor pressure p_v as $p_b = p_v - 2\sigma/R_b - 4\eta\dot{R}_b/R_b$. The terms corresponding to the surface tension σ and viscosity η can be neglected, as they do not play a significant role in bubble dynamics in case of millimeter-scale bubbles [77]. Thus, the pressure difference at the bubble wall in Eq. (3) simply equals $\Delta p = p_v - p_0$.

We calculated the bubble pressure difference by deriving the temporal bubble radius evolution (obtained by fitting Eq. (S15) to discrete radius measurements) and incorporating the first and second derivative into Eq. (3), as described in Section S3.2 of the Supporting Information.

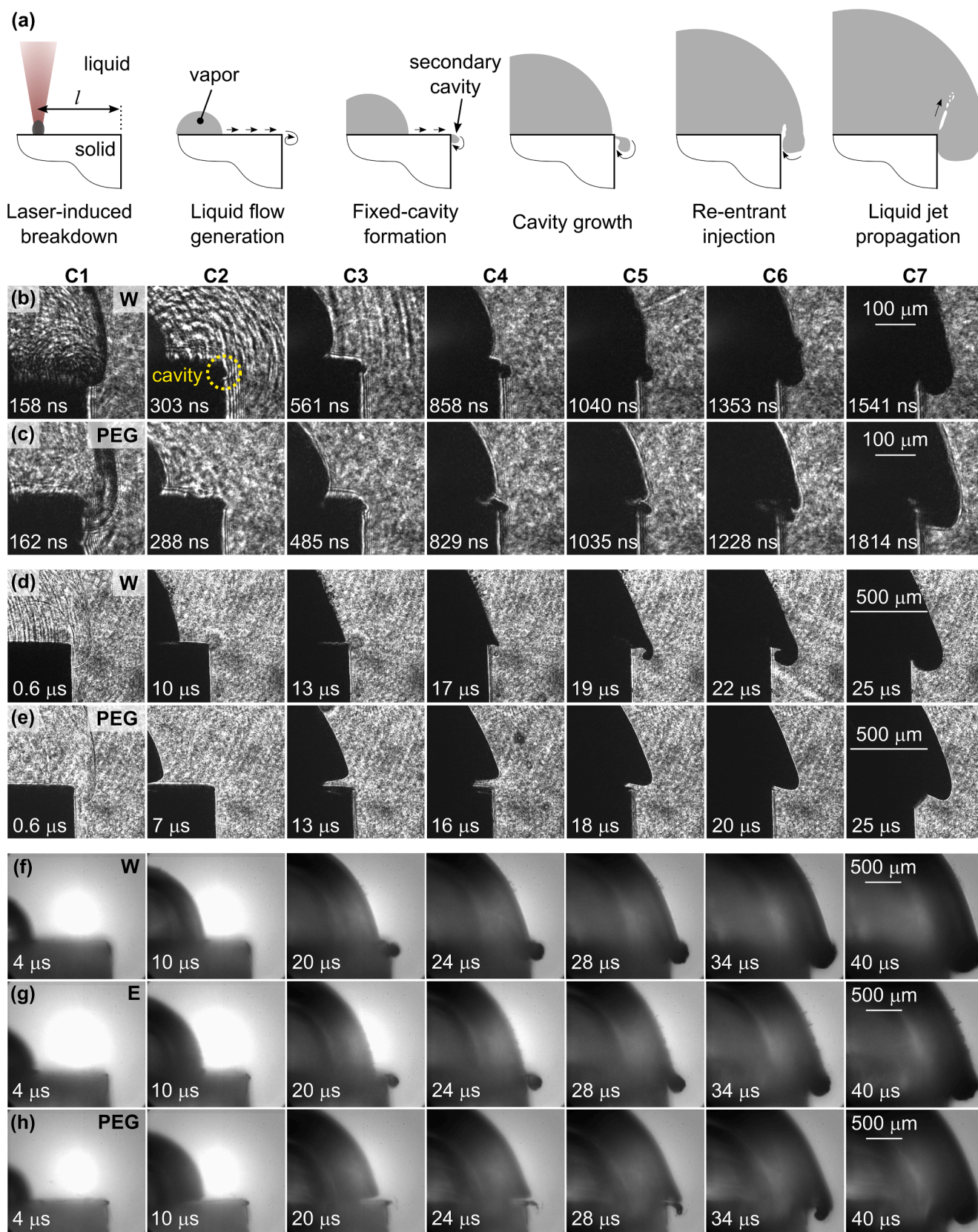


Fig. 5. (a) Schematic presentation of the bubble-induced flow evolution over a “cliff-like” 90° edge in case of secondary cavity formation. Bubble overflow was induced at (b), (c) $l = 0.3$ mm, (d), (e) $l = 1$ mm, and (f)–(h) $l = 1.7$ mm from the edge in water (W), ethanol (E), and PEG. Pulse energy equals 10.6 mJ for (b–e) and 55 mJ for (f–h).

By doing this, the initial pressure difference at the cavitation bubble wall (at 65 ns after breakdown) could be estimated to 1.3×10^3 bar in water and 0.7×10^3 bar in PEG (see Figs. 3d and S18). These results are found consistent with the work of Vogel et. al, who studied optical breakdown in infinite water [14]. Similarly, Lam et al. [77] and De Giacomo et al. [28] calculated the vapor pressure inside the bubble on the basis of temporal radius evolution that was measured by ultrafast videography. Due to longer time intervals between consecutive images, their first measurements begin at 5 μ s after excitation, at which time the estimated pressure p_v is in the order of 100 bars, presuming constant pressure of surrounding liquid p_0 . In comparison, our results do not make this assumption but rather consider the overall pressure difference $\Delta p = p_v - p_0$ at the bubble wall. However, since the surrounding pressure p_0 is usually assumed in the order of several bars [77], the difference between p_v and Δp (assuming constant p_0) should only be noticeable when pressure inside the bubble decreases below 100 bars. Taking this into account, our results propose the decrease of pressure difference to the value of 100 bars sooner (compared to [28,77]), i.e., 700 ns after excitation in water and 400 ns in PEG. The inconsistency could perhaps be attributed to significantly higher temporal resolution and number of images obtained in the first microsecond with our setup, which increases the validity of radii measurements during that short initial period.

4.2. Development of the cavitation bubble on finite geometry

The majority of existing LAL studies on solids deal with “infinite” flat geometries of the ablated surfaces [20,32,77,78], where the maximum bubble radius is significantly smaller than the distance between the bubble center and the nearest edge of the flat solid surface ($R_{b,max} \ll l$). On the contrary, in this study we deliberately induce breakdown in close proximity to the edge of the flat surface in order to study phenomena on finite geometry. We achieved this by either (i) irradiating a very thin sample (Fig. S1a) or (ii) positioning the breakdown spot close to the sample’s edge (Fig. S1b). In the first case, 17 mm wide samples with

thicknesses from 25 μ m to 2 mm were clamped in an “H” configuration (see Fig. S1a). Thus, the direction of the longer (17 mm) dimension remained “infinite” (as it was significantly larger than the maximum radius of the bubble), while the shorter dimension could be classified as “finite”.

In the second case, samples were clamped in an “L” configuration (Fig. S1b). Sample thickness was kept constant and equaled $d = 2$ mm, while the breakdown was positioned between $l = 0.1$ mm and $l = 1.7$ mm away from the edge of the sample (dimension b in Fig. S1b). The bubble thereby reached three (out of four) edges of the sample. Samples with thicknesses over 2 mm were deliberately not used to avoid the shadow resulting from misalignment of the sample surface with the optical axis.

Generally, when the bubble is produced far away from the edge of the solid sample, its radius at maximum size, $R_{b,max}$, is smaller than the distance from the bubble center to the edge ($R_{b,max} \ll l$). In that case, the bubble does not reach the edge and the sample surface can be considered as infinite. Contrarily, when the edge is located in close proximity to the breakdown spot ($l < R_{b,max}$), the liquid–vapor interface (i.e., the bubble wall) expands beyond the solid edge and results in overflow of (first) the liquid that surrounds the bubble and (later) the vapor that is inside the bubble. During the liquid flow (driven by the expansion of the cavitation bubble) over the edge, a secondary bubble (i.e., the so-called secondary cavity) can form just beyond the edge due to formation of a low pressure area in the liquid. Furthermore, a jet of liquid can in some cases penetrate into the laser-induced cavitation bubble when the bubble overflows the edge (see schematics in Fig. 5a). Development of such injection depends on (i) the energy of the bubble (which determines its maximum radius) and (ii) the distance between the bubble center and the edge, as well as (iii) the physical properties of the liquid.

Since the maximum bubble radius, $R_{b,max}$, and the distance of the bubble from the edge, l , are correlated, it is appropriate to introduce the dimensionless distance from the edge as

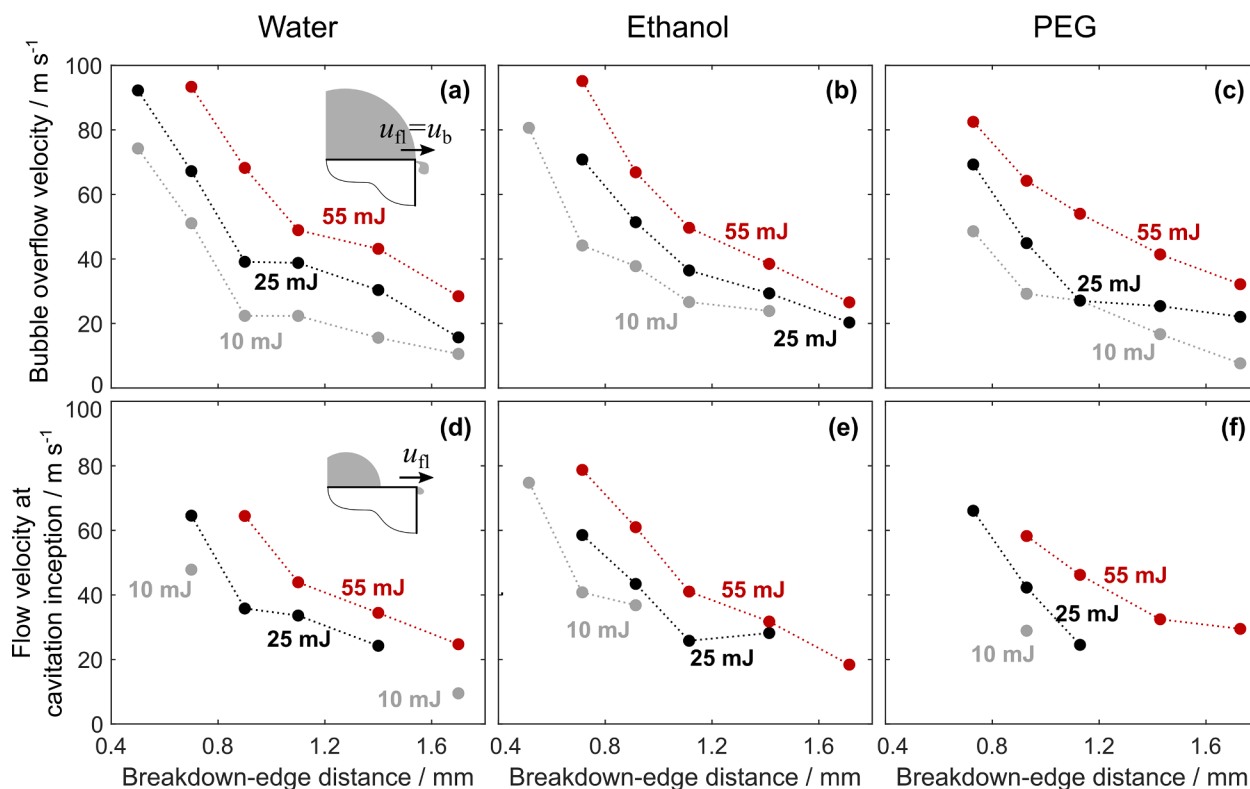


Fig. 6. The bubble overflow velocity over the sharp edge in (a) water, (b) ethanol, and (c) PEG at different breakdown-edge distances and pulse energies (marked in each subfigure). (d-f) Velocity of the liquid flow over the edge at the time of the secondary cavity inception in water, ethanol, and PEG, respectively.

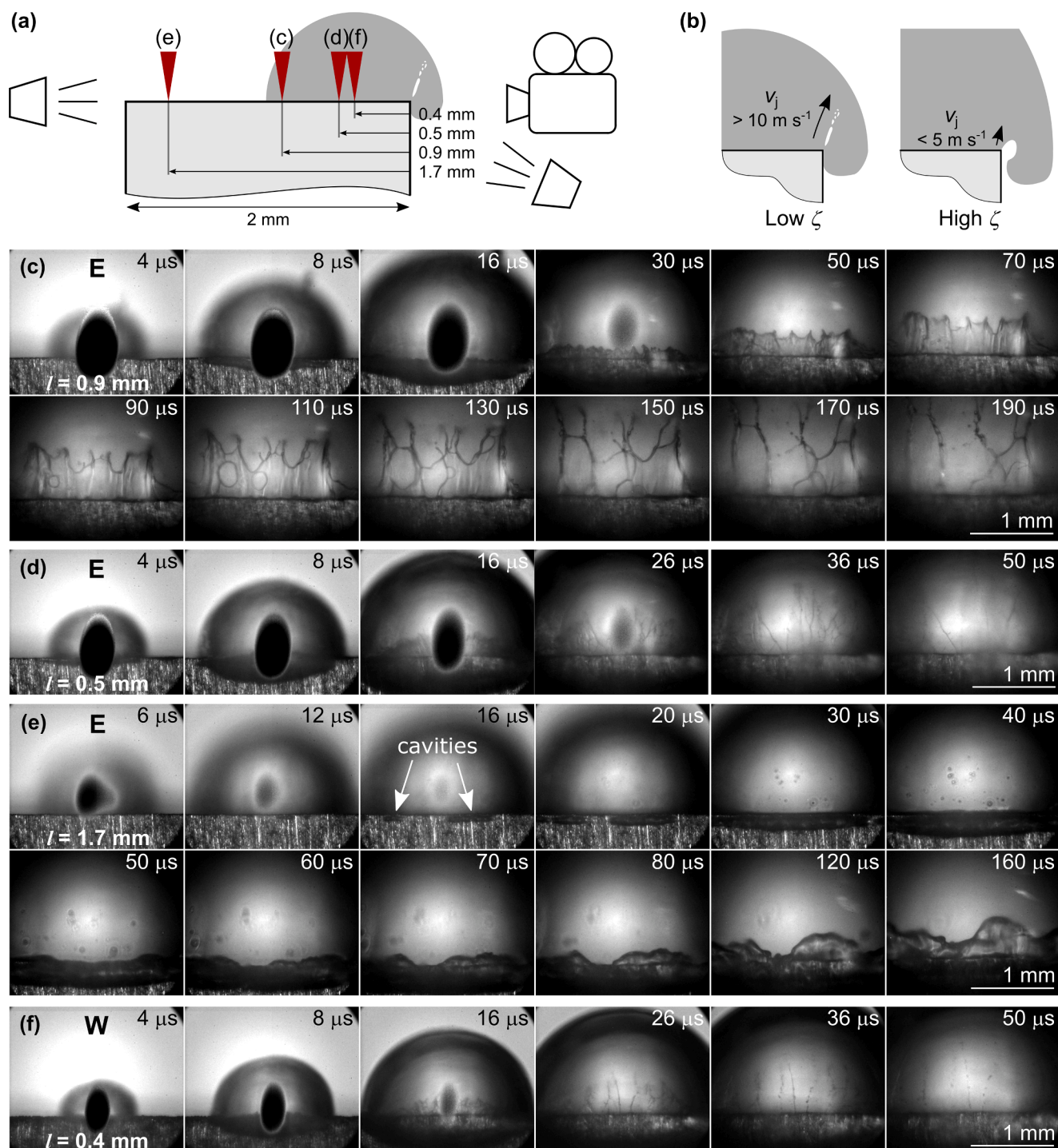


Fig. 7. (a) Schematics showing the breakdown position with respect to the edge. (b) Schematic representation of injection dynamics in case of lower ζ (breakdown closer to the edge) and higher ζ (breakdown farther from the edge). (c–e) Injection of ethanol (E) and (f) water (W) inside the bubble following bubble's expansion over the edge. The breakdown-edge distance l is shown in (a). Pulse energy equals 25 mJ. Black spots in the center of the bubble are due to saturation of the ICCD shortly after plasma formation.

$$\zeta = \frac{l}{R_{b,\max}} \quad (5)$$

However, in our experiments, we were not able to determine the maximum radii of the bubbles with existing experimental setup due to high optical magnification that resulted in smaller viewing area than the bubble at its maximum size. Thus, when needed, $R_{b,\max}$ was roughly estimated from the collapse time of the bubble T_c as [40,79]

$$R_{b,\max} = \frac{T_c}{0.915\sqrt{\rho_0/(p_0 - p_v)}} \quad (6)$$

In Eq. (6), p_v stands for the vapor pressure inside the bubble.

In order to investigate the effects and dynamics of liquid–vapor overflow over a finite geometry, we generated the bubble at different distances l from the edge. In this case, samples S4 and S5 (see Table 2) were used for the experiments with experimental setups #2 and #1,

respectively. During all the measurements, we have not detected any movement of the bubble center (the raw data are available in Ref. [72]).

Typical images of bubble expansion induced at different distances from the edge of the flat surface and in different liquids (water, ethanol, and PEG) are shown in Fig. 5. After the laser-induced breakdown, the expanding bubble generates a liquid flow that is “guided” by the surface of the sample (first two sketches in Fig. 5a). When the liquid overflows the edge of the solid, a low pressure area forms beyond the edge. If the pressure in this area decreases below the vapor pressure of the liquid, vaporization of the liquid occurs. This results in development of a (vapor filled) secondary cavity (third sketch in Fig. 5a) by breaking away of the flow from the guiding surface at the point of low-pressure. Flow velocity in this instant is estimated in Fig. 6d–f. From this point, the main flow of the liquid follows a free trajectory that is determined by the pressure field and usually returns to the surface at some point downstream. The space between the solid-guiding surface and the free-liquid surface is generally classified as a fixed cavity [80–82], since its position – with respect to the rigid boundary upon which it forms – is fixed.

The flow of liquid in most experimental studies of fixed cavitation [82,83] is continuous and, therefore, a somewhat cyclical process develops. The fixed cavity typically undergoes three phases [80,81]: (i) formation and growth, (ii) filling, and (iii) breakoff. It is generally accepted [84] that cavity breakoff is caused by re-entrant injection of liquid, which forms in the high-pressure area at the downstream end of the cavity and flows upstream towards the leading edge. The upstream velocity of this re-entrant jet is proportional to the velocity of the liquid at the cavity interface.

When the flow of supplying liquid is continuous, cloud cavitation [85] is often observed downstream of the attached cavitation, resulting from the abovementioned periodical cavitation process. Contrarily, the flow driven by expansion of the bubble is not continuous, since the supply of liquid is discontinued when the bubble expands over the edge. Consequently, instead of recombining with the main flow and causing cavity breakoff, re-entrant jet propagates further through the vapor bubble, as schematically presented by the fifth and sixth sketch in Fig. 5a (this injection can be clearly observed by using diffuse illumination – Fig. 7). The secondary cavity in the meantime merges with the cavitation bubble, which continues to expand away from the edge.

Experimental observations in water and PEG reveal that the secondary cavity is formed ~ 300 ns after the optical breakdown that is induced by 10.6-mJ laser pulse at $l = 0.3$ mm (Figs. 5b and c, column

C2). Due to significantly higher viscosity of PEG compared to water, bubble detachment from the guiding surface (Fig. 5c, columns C4 and C5) becomes more apparent in PEG than in water, which is consistent with findings of Hupfeld et al. [86]. Bubble wall reaches the edge in both liquids around 0.8–0.9 μ s after the excitation (see Fig. S16). According to temporal velocity profiles in Fig. 4c (see also Fig. S17 for larger timescale), the velocity of the bubble wall at that time equals around 150 m s^{-1} .

Fig. 5d, e show the bubble dynamics for the same laser pulse energy, but at increased breakdown-edge distance, $l = 1$ mm. Increasing the distance results in lower velocity of the liquid flow (induced by the same pulse energy) over the edge of the sample. Based on the images in Figs. 5d, e, velocity of the liquid when the bubble overflows the edge is estimated to ~ 30 m s^{-1} . Due to lower flow velocity (compared to $l = 0.3$ mm), the pressure behind the edge is no longer sufficiently low to vaporize the liquid. Consequently, the secondary cavity does not form in this case. However, the dynamics of the bubble wall is still affected. In case of water (having low viscosity), the liquid–vapor interface close to the edge follows a spiral like trajectory (Fig. 5d, column C5), while significantly higher viscosity of PEG leads to more gradual “pulling” of the bubble into the low pressure area (C5 in Fig. 5e). The gap resulting from detachment of the bubble wall from the sample surface (C4 in Fig. 5e) is even more apparent at larger breakdown-edge offsets, since the shear flow between the sample surface and the bubble wall is maintained for a longer duration of time. The gap is also briefly noticeable in (less viscous) water (C2 and C3 in Fig. 5d) just before it is overshadowed by the bubble’s expansion beyond the edge.

By increasing the energy of excitation pulse from 10.6 mJ to 55 mJ, the secondary cavity forms even if the breakdown-edge distance is increased to $l = 1.7$ mm (see Figs. 5f–h, as well as Videos S1 and S2 that correspond to images in Figs. 5f and 5h, respectively). This dynamics was captured from a single event (by using experimental setup #1). There is no apparent difference between water and ethanol (Figs. 5f, g), since their properties – especially the vapor pressure and viscosity – are in the same order of magnitude (see Table 1). On the other hand, the secondary cavity that forms in PEG (C4 in Fig. 5h and Video S2) appears thinner and elongated in the direction of the flow. This could be attributed to significantly (three orders of magnitude) lower vapor pressure and significantly (for almost two orders of magnitude) higher viscosity of PEG compared to water and ethanol.

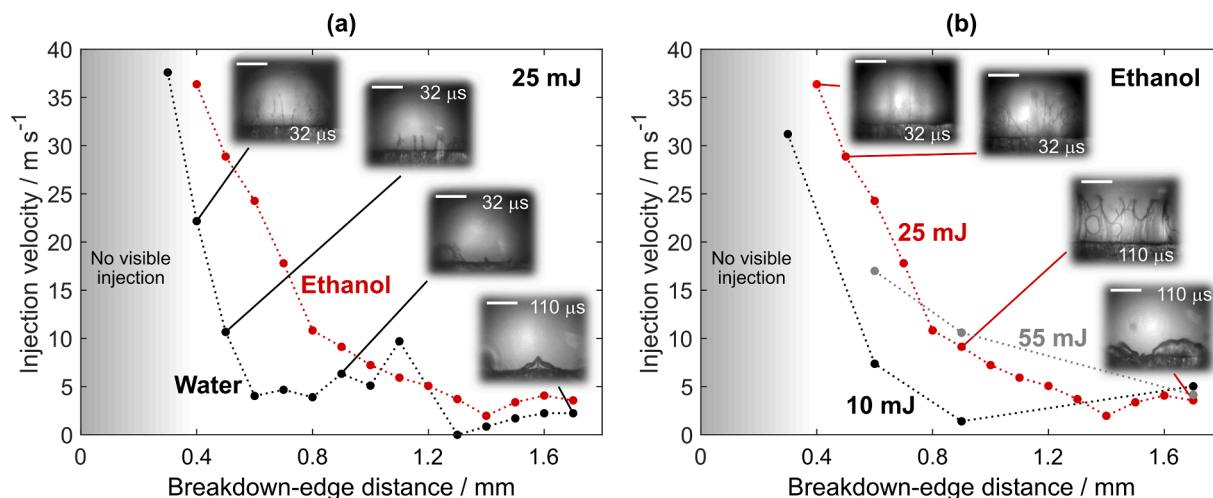
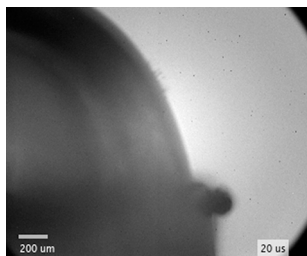
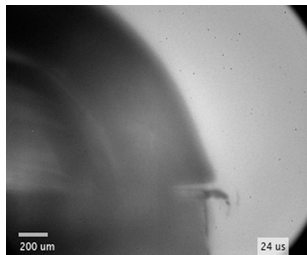


Fig. 8. Velocity of liquid injection inside the bubble, induced at different breakdown-edge distances. (a) Comparison of injection velocity in water and ethanol at constant pulse energy of 25 mJ. (b) Comparison of different pulse energies in ethanol. Note that the red curves in (a) and (b) are the same curve. Inset images in (a) and (b) correspond to injections in water and ethanol (at 0.4 mm, 0.5 mm, 0.9 mm, and 1.7 mm breakdown-edge distances), respectively. Scale bars equal 0.5 mm and time indicates the time after breakdown. (For interpretation of the references to colour in this figure legend, the reader is referred to the web version of this article.)



Video S1. Secondary cavity formation in water.



Video S2. Secondary cavity formation in PEG.

Observation of bubble dynamics from a single event by using experimental setup #1 allows direct estimation of the velocity of liquid flow over the edge u_{fl} (Fig. 6). Here, the bubble wall was tracked to determine its velocity u_b . Considering conservation of mass and assuming incompressible liquid, liquid flow at the edge u_{fl} can be determined as

$$u_{fl} = u_b \frac{R_b^2}{r^2} \quad (7)$$

Fig. 6a-c show the velocity of the bubble when it overflows the edge (see schematics in Fig. 6a) in water, ethanol, and PEG, respectively. Since the bubble radius R_b at this instant equals l , bubble wall velocity u_b (at this moment) is also equal to the velocity of liquid flow over the edge u_{fl} . These results show that increasing the pulse energy increases the velocity of the liquid overflow in the moment that the bubble overflows the edge. Furthermore, it is also clear that this velocity is decreasing by positioning the breakdown farther from the edge (increasing ζ). As $\zeta \rightarrow 1$, the overflow velocity approaches 0, while for $\zeta \rightarrow 0$, the flow velocity at the edge should converge to the very early-stage bubble wall velocity, i.e., several hundred meters per second (see Fig. 4c). However, this cannot be measured by experimental setup #1, since the measurement of bubble wall velocity requires two consecutive frames with a visible bubble wall. Thus, flow velocity could not be determined for the very short breakdown-edge distances, where the bubble wall was visible for less than two frames before overflowing the edge.

Fig. 6d-f present the liquid overflow velocity at the moment that the secondary cavity (cavitation inception) is visually detected in the acquired videos (see schematics in Fig. 6d). Dynamics during a $\pm 4 \mu\text{s}$ time window surrounding the secondary cavity formation is shown in Section S4 of the Supporting Information. From our observations, secondary cavitation was only detected if the liquid overflow velocity exceeded $\sim 20 \text{ m s}^{-1}$. An exception is detected in case of 10 mJ pulse excitation at $l = 1.7 \text{ mm}$ in water (Fig. 6d). In this case, preexisting small bubbles on the sample surface evidently act as cavitation nuclei, reducing this threshold velocity (see raw data in Ref. [72]). Calculated flow velocity at

the point of inception increases at shorter breakdown-edge distances due to a very rapid rise of the bubble wall velocity during bubble formation. Since cavity formation (vaporization) is not instantaneous, the flow velocity at the instance of secondary cavity detection (only a few microseconds after the laser-induced breakdown) is already significantly above the threshold value.

Interestingly, experiments performed with experimental setup #2 in water and PEG at 1 mm breakdown-edge distance (Figs. 5d, e) did not result in secondary cavity formation, even though the estimated flow velocity at the time of the bubble overflow equaled $\sim 30 \text{ m s}^{-1}$. This could perhaps be explained by a different process of sharp-edge preparation (milling in case of samples for experimental system #1 and cutting & polishing in case of experimental system #2), yielding a slight variation of the burr. Results by Petkovšek et al. [55] show that incipient cavitation significantly depends on surface microstructures. Thus, changes in the burr could influence the secondary cavity inception by altering the local flow dynamics and consequently affecting the pressure difference induced at the edge.

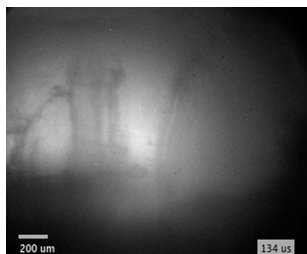
4.3. Liquid injection into the cavitation bubble

By incorporating diffuse illumination to see inside the cavitation bubble, we were able to detect and analyze the propagating liquid jet at various conditions. Qualitative characteristics of liquid jets are summarized in Fig. 7, while their velocities are shown in Fig. 8. These experiments were performed by experimental setup #1 in water, ethanol, and PEG. However, injections of liquid into the bubble were only detected in water and ethanol, presumably due to significantly higher viscosity of PEG (see Fig. S30 for direct comparison), which substantially decreases the velocity of re-entrant injection. At pulse energy of 25 mJ, liquid injections are observed in water when the breakdown-edge distance exceeds the threshold distance $l \geq 0.3 \text{ mm}$, while in ethanol the jets are not visible until this distance increases to $l \geq 0.4 \text{ mm}$.

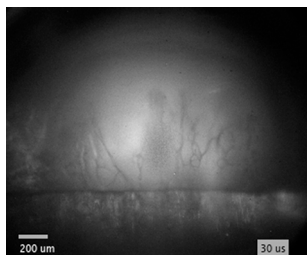
The most pronounced injections were detected in ethanol with pulse energy of 25 mJ at $l = 0.9 \text{ mm}$ (Fig. 7c and Video S3). In this case, velocity and direction of injection shortly after detachment from the edge are fairly uniform from left to right, creating the appearance of a liquid “wall” (Fig. 7c, 70 μs). As the liquid continues to propagate through the cavitation bubble, surface tension transforms this wall into narrow jets and droplets (Fig. 7c, 170 μs). Observation from the side (supplementary Fig. S29 at 120 μs and Video S4) reveals that the direction of injection inside the bubble is in fact not coplanar with the vertical surface of the sample. It is rather directed at a slight angle that points away from the breakdown position, as depicted in the sixth sketch in Fig. 5a. The “tip” velocity of the injection v_j is estimated to $\sim 10 \text{ m s}^{-1}$ (Fig. 8a).



Video S3. Front view of injection in ethanol.



Video S4. Side view of injection in ethanol.

Video S5. Injection at lower ζ (narrow jets and droplets).

By changing the breakdown-edge distance, characteristics of injection change. Moving the optical breakdown closer to the edge (Fig. 7d and Video S5) increases the velocity of the jet, while its shape no longer resembles a wall. Injection velocity in Fig. 7d is estimated to $v_j \sim 30 \text{ m s}^{-1}$ (Fig. 8a). The jet in this case rather consists of very narrow jets and droplets that, compared to Fig. 7c, now “originate” in the “central” part of the bubble and propagate also in the horizontal directions (Fig. 7d, 36 μs). The latter can be explained by smaller radius of the bubble at the moment it reaches the edge (i.e., when $R_b \sim D$), which promotes gradual opposed to simultaneous overflow of the bubble wall along the edge of the sample.

Maximum velocity of injection in water of $v_j \sim 38 \text{ m s}^{-1}$ was detected at $l = 0.3 \text{ mm}$ (Fig. 8a). In ethanol, highest velocity of the jet equal to $v_j \sim 36 \text{ m s}^{-1}$ and was observed at $l = 0.4 \text{ mm}$. When breakdown-edge distance was decreased below these values ($l < 0.3 \text{ mm}$ in water, Fig. S31a; $l < 0.4 \text{ mm}$ in ethanol, Fig. S31b, both at pulse energy 25 mJ), the injection was not visible anymore. This might be due to significantly lower volume of injection and its dispersion into smaller droplets with high velocity (possibly exceeding 40 m s^{-1}) that makes such detection more difficult – as the image contrast is limited due to necessity of diffuse illumination to see inside the bubble.

Another possible explanation is that the bubble wall reaches the edge too early – when the pressure inside the bubble is still too high to allow the formation of re-entrant jet. Furthermore, smaller radius and, therefore, height of such early stage bubble at the time of (edge) overflow could cause the re-entrant injection to hit the bubble wall instead of propagating through the bubble during its expansion.

Injections were also studied with bubbles being induced in the middle of a thin (25 μm –2 mm wide, see Table 2) sample surface to produce symmetrical “enwrapping” of the solid. Similarly, the injections in such experiments were not visible at thicknesses of the sample below a certain value (<1 mm in water at 25 mJ), leading to similar conclusions (see Section S6 of the Supporting Information).

As the breakdown is induced farther from the edge, ζ increases and the velocity of the injection v_j decreases, as visible in Fig. 8a. As can be seen from Fig. 7e (see also Video S6), the jet is practically floating inside the bubble ($v_j \sim 4 \text{ m s}^{-1}$) without advancing toward the bubble wall. This can be explained by lower velocity of the bubble wall (and consequently liquid flow) at the time of edge overflow (Fig. 6b), which also reduces the velocity of re-entrant injection. Comparison to jet dynamics induced at lower ζ (Figs. 7c, d) is schematically depicted in Fig. 7b. Increasing the breakdown-edge distance also prolongs the time interval before the bubble wall reaches the edge of the sample, which leads to longer exposure of surrounding liquid to low pressure. The secondary cavity

thereby grows larger in diameter and length along the edge (Fig. 7e, 16–40 μs) compared to shorter breakdown-edge offsets. The nuclei that initiate the growth of the secondary cavity at inception were generally found to occur at multiple positions along the edge of the sample (Fig. 7e, 16 μs). Whether they primarily originate from the liquid flow or specific spots on the sample surface/edge was not investigated. However, we detected that small bubbles on the surface remaining from previous experiments in some cases act as nuclei (see raw data in Ref. [72], video of 10 mJ excitation in water at $l = 1.7 \text{ mm}$) and promote formation of a secondary cavity also at higher ζ . The dark spots that are visible at the bubble wall in Fig. 7e at 40 μs are ripples, most likely caused by droplets that originate from the liquid injection at the farther edge of the sample.

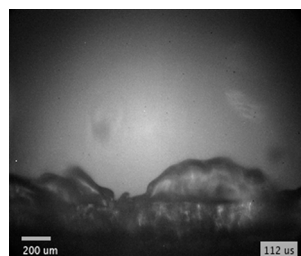
Video S6. Injection at higher ζ (floating injection).

Fig. 8 shows comparisons of injection velocities, v_j , that were observed at different parameters. The data were obtained by manually tracking the “tip” of each injection at three different locations along the edge (raw data in Ref. [72]). The velocity values presented in the graphs are the average of these three measurements.

As can be seen from Fig. 8a, liquid jets in water (Fig. 7f) at the same pulse energy were detected at shorter breakdown-edge distances (already at $l = 0.3 \text{ mm}$) compared to ethanol. Furthermore, the measured velocity of the jet v_j at equal breakdown-edge distances is generally lower in water than ethanol (Fig. 8a). The outlying exception at $l = 1.1 \text{ mm}$ can be explained by slightly asymmetrical bubble overflow of the edge, which resulted in formation of a small injection with relatively high velocity at one side of the edge (see Fig. S32). The inset images of injections induced at equal breakdown-edge distances in water (insets in Fig. 8a) and ethanol (insets in Fig. 8b) additionally reveal that the shape of the injection in water never resembled a “wall” (for full dynamics see Fig. S33). This is most probably due to higher surface tension. Further investigation of underlying causes for differences in jet dynamics induced in water and ethanol is out of the scope of this work. However, in addition to the properties of the liquid, the energy conversion efficiency from the optical pulse energy into the cavitation bubble energy is also important, since it directly influences the maximum bubble radius [26,40] and, consequently, the ratio ζ .

Changing the laser pulse energy (Fig. 8b) exhibited a similar effect as variation of breakdown-edge distance. Increasing solely the pulse energy resulted in higher injection velocity, while the jets became narrower (see Figs. S34 and S35 for comparison). Thus, increasing the pulse energy leads to similar results as decreasing the breakdown-edge distance at the same pulse energy. However, at higher pulse energy, probability of a double breakdown due to impurities in the liquid increases. When this happens, the cavitation bubble energy is decreased. As a result of double breakdown (see Fig. S36 for dynamics), jet velocity in case of 55 mJ excitation in ethanol at $l = 0.6 \text{ mm}$ is lower compared to 25 mJ excitation at the same breakdown-edge distance (Fig. 8b).

The similarity of pulse-energy and breakdown-distance effects further demonstrates the importance of dimensionless parameter ζ , defined by Eq. (5). By using Eq. (6), we estimated the maximum bubble radii in ethanol (as the most noticeable injections were detected there) to $\sim 1.5 \text{ mm}$, $\sim 1.8 \text{ mm}$, and $\sim 2.3 \text{ mm}$ at 10 mJ, 25 mJ, and 55 mJ pulse energy, respectively. From these we can conclude that the injections in ethanol were not visible at $\zeta < 0.2$, while the most pronounced jets (Fig. 7c) were detected at $\zeta \sim 0.5$.

5. Conclusions

We have theoretically and experimentally demonstrated that diffuse illumination (compared to collimated illumination) represents an excellent approach for increasing the observability of fluid dynamics *inside* the cavitation bubbles in the visible spectrum. Thus, diffusive illumination was further used to study the fluid dynamics inside the laser-induced cavitation bubble, when it expands over a 90° sharp solid–liquid boundary, while a high-speed shadowgraphy with ps illumination was used to understand the bubble dynamics within the first several hundred nanoseconds after the laser-induced breakdown. The presented results lead to the following conclusions:

- Bubble-driven overflow of the surrounding liquid in case of a “cliff-like” 90° solid edge may lead to formation of a fixed-type secondary cavity behind the edge. Here, higher pulse/bubble energy and/or breakdown that is induced closer to the edge increase the pressure drop behind the edge and make the conditions more favorable for secondary cavity formation. Secondary cavitation was detected when the liquid overflow velocity exceeded a threshold value of $\sim 20 \text{ m s}^{-1}$. Larger cavities were observed at larger breakdown-edge offsets due to longer-lasting cavity growth (vaporization). In case of insufficient bubble energy and/or excessive breakdown-edge distance, the bubble wall is merely “pulled” into the low pressure area without development of a secondary cavity. The trajectory of this overflow depends on the viscosity of the liquid.
- Re-entrant injection of liquid with velocity of up to $\sim 40 \text{ m s}^{-1}$ inside the cavitation bubble was clearly observed when the bubble is passing over the 90° edge of the solid sample. The obtained results prove that the jet is far more likely to occur in water and ethanol than polyethylene glycol, which indicates a significant role of liquid viscosity and surface tension. The most pronounced injections were observed in ethanol when the breakdown-edge offset equaled approximately half of the maximum bubble radius. In this case, the shape of the liquid injection firstly resembles a wall. During subsequent evolution (inside the bubble), surface tension of the liquid leads to transition of this liquid wall into narrower jets and droplets.
- Experiments on 25 μm –2 mm thick metal foils reveal the existence of a “threshold” thickness of the sample at which the injections become noticeable. For nanosecond pulses with 25 mJ pulse energy in water, this thickness is in the order of several hundred micrometers when a 90° edge of the sample is considered.

The above-listed conclusions represent new fundamental insights into dynamics of laser-induced cavitation bubbles that expand near a sharp solid–liquid boundary. Such boundary conditions in combination with diffuse illumination that allows observation *inside* the cavitation bubble can be utilized in controlling and improving the yield of nanoparticle production. Furthermore, they serve to a more general understanding of bubble dynamics within confined geometries.

6. Funding sources

This research was funded by the Slovenian Research Agency (Projects No. J2-1741 and BI-JP/18-20-004 and research core funding No. P2-0392) and JSPS under the Japan-Slovenia Research Cooperative Program and JSPS KAKENHI Grant Number JP20H02764.

CRedit authorship contribution statement

Matej Senegačnik: Conceptualization, Methodology, Software, Validation, Formal analysis, Investigation, Data curation, Writing - original draft, Writing - review & editing, Visualization. **Kohei Kunitomo:** Investigation. **Satoshi Yamaguchi:** Investigation, Resources. **Koki Kimura:** Investigation. **Tetsuo Sakka:** Conceptualization, Methodology, Investigation, Writing - review & editing, Supervision, Project

administration, Funding acquisition. **Peter Gregorčič:** Conceptualization, Methodology, Validation, Formal analysis, Investigation, Data curation, Writing - original draft, Writing - review & editing, Supervision, Project administration, Funding acquisition.

Declaration of Competing Interest

The authors declare that they have no known competing financial interests or personal relationships that could have appeared to influence the work reported in this paper.

Acknowledgments

M.S and P.G. acknowledge the financial support from the Slovenian Research Agency (Projects No. J2-1741 and BI-JP/18-20-004 and research core funding No. P2-0392). K.Ku, S.Y., K.Ki., and T.S. acknowledge the financial support from JSPS under the Japan-Slovenia Research Cooperative Program and JSPS KAKENHI Grant Number JP20H02764.

Appendix A. Supplementary data

Supplementary data to this article can be found online at <https://doi.org/10.1016/j.ultsonch.2021.105460>.

Research data (original video and imaging data) have been deposited to Mendeley Data and are available at <http://doi.org/10.17632/w8m3z3v3w2.1>.

References

- [1] T. Sakka, S. Iwanaga, Y.H. Ogata, A. Matsunawa, T. Takemoto, Laser ablation at solid–liquid interfaces: An approach from optical emission spectra, *J. Chem. Phys.* 112 (19) (2000) 8645–8653, <https://doi.org/10.1063/1.481465>.
- [2] V. Lazic, F. Colao, R. Fantoni, V. Spizzicchio, Recognition of archeological materials underwater by laser induced breakdown spectroscopy, *Spectrochim. Acta Part B At. Spectrosc.* 60 (7–8) (2005) 1014–1024, <https://doi.org/10.1016/j.sab.2005.06.014>.
- [3] T. Sakka, A. Tamura, T. Nakajima, K. Fukami, Y.H. Ogata, Synergetic effects of double laser pulses for the formation of mild plasma in water: Toward non-gated underwater laser-induced breakdown spectroscopy, *J. Chem. Phys.* 136 (17) (2012) 174201, <https://doi.org/10.1063/1.4709391>.
- [4] Y. Wang, X. Zhao, C. Ke, J. Yu, R. Wang, Nanosecond laser fabrication of superhydrophobic Ti6Al4V surfaces assisted with different liquids, *Colloids Interface Sci. Commun.* 35 (2020) 100256, <https://doi.org/10.1016/j.colcom.2020.100256>.
- [5] E. Stratakis, V. Zorba, M. Barberoglou, C. Fotakis, G.A. Shafeev, Laser writing of nanostructures on bulk Al via its ablation in liquids, *Nanotechnology* 20 (10) (2009) 105303, <https://doi.org/10.1088/0957-4484/20/10/105303>.
- [6] J.S. Hoppius, L.M. Kukreja, M. Knyazeva, F. Pöhl, F. Walther, A. Ostendorf, E. L. Gurevich, On femtosecond laser shock peening of stainless steel AISI 316, *Appl. Surf. Sci.* 435 (2018) 1120–1124, <https://doi.org/10.1016/j.apsusc.2017.11.145>.
- [7] H. Wang, Y. Kalchev, H. Wang, K. Yan, E.L. Gurevich, A. Ostendorf, Surface modification of NiTi alloy by ultrashort pulsed laser shock peening, *Surf. Coat. Technol.* 394 (2020) 125899, <https://doi.org/10.1016/j.surfcoat.2020.125899>.
- [8] D. Zhang, B. Gökce, S. Barcikowski, Laser Synthesis and Processing of Colloids: Fundamentals and Applications, *Chem. Rev.* 117 (5) (2017) 3990–4103, <https://doi.org/10.1021/acs.chemrev.6b00468>.
- [9] A. Kanitz, M.-R. Kalus, E.L. Gurevich, A. Ostendorf, S. Barcikowski, D. Amans, Review on experimental and theoretical investigations of the early stage, femtoseconds to microseconds processes during laser ablation in liquid-phase for the synthesis of colloidal nanoparticles, *Plasma Sour. Sci. Technol.* 28 (10) (2019) 103001, <https://doi.org/10.1088/1361-6595/ab3d8e>.
- [10] V. Amendola, M. Meneghetti, Laser ablation synthesis in solution and size manipulation of noble metal nanoparticles, *Phys. Chem. Chem. Phys.* 11 (2009) 3805–3821, <https://doi.org/10.1039/B906544K>.
- [11] C.L. Sajti, R. Sattari, B.N. Chichkov, S. Barcikowski, Gram scale synthesis of pure ceramic nanoparticles by laser ablation in liquid, *J. Phys. Chem. C* 114 (6) (2010) 2421–2427, <https://doi.org/10.1021/jp906960g>.
- [12] W. Soliman, N. Takada, K. Sasaki, Growth processes of nanoparticles in liquid-phase laser ablation studied by laser-light scattering, *Appl. Phys. Express* 3 (3) (2010) 035201, <https://doi.org/10.1143/APEX.3.035201>.
- [13] S. Ibrahimkutty, P. Wagener, A. Menzel, A. Plech, S. Barcikowski, Nanoparticle formation in a cavitation bubble after pulsed laser ablation in liquid studied with high time resolution small angle x-ray scattering, *Appl. Phys. Lett.* 101 (10) (2012) 103104, <https://doi.org/10.1063/1.4750250>.

- [14] A. Vogel, S. Busch, U. Parlitz, Shock wave emission and cavitation bubble generation by picosecond and nanosecond optical breakdown in water, *J. Acoust. Soc. Am.* 100 (1) (1996) 148–165, <https://doi.org/10.1121/1.415878>.
- [15] M.P. Felix, A.T. Ellis, Laser-induced liquid breakdown—a step-by-step account, *Appl. Phys. Lett.* 19 (11) (1971) 484–486, <https://doi.org/10.1063/1.1653783>.
- [16] M.S. Plesset, R.B. Chapman, Collapse of an initially spherical vapour cavity in the neighbourhood of a solid boundary, *J. Fluid Mech.* 47 (2) (1971) 283–290, <https://doi.org/10.1017/S0022112071001058>.
- [17] A. Vogel, W. Lauterborn, R. Timm, Optical and acoustic investigations of the dynamics of laser-produced cavitation bubbles near a solid boundary, *J. Fluid Mech.* 206 (1989) 299–338, <https://doi.org/10.1017/S0022112089002314>.
- [18] P. Gregorič, R. Petkovšek, J. Možina, Investigation of a cavitation bubble between a rigid boundary and a free surface, *J. Appl. Phys.* 102 (9) (2007) 094904, <https://doi.org/10.1063/1.2805645>.
- [19] U. Orthaber, J. Zevnik, R. Petkovšek, M. Dular, Cavitation bubble collapse in a vicinity of a liquid-liquid interface – Basic research into emulsification process, *Ultrason. Sonochem.* 68 (2020) 105224, <https://doi.org/10.1016/j.ultsonch.2020.105224>.
- [20] W. Lauterborn, H. Bolle, Experimental investigations of cavitation-bubble collapse in the neighbourhood of a solid boundary, *J. Fluid Mech.* 72 (1975) 391–399, <https://doi.org/10.1017/S0022112075003448>.
- [21] W. Lauterborn, C.-D. Ohl, Cavitation bubble dynamics, *Ultrason. Sonochem.* 4 (2) (1997) 65–75, [https://doi.org/10.1016/S1350-4177\(97\)00009-6](https://doi.org/10.1016/S1350-4177(97)00009-6).
- [22] S. Popinet, S. Zaleski, Bubble collapse near a solid boundary: a numerical study of the influence of viscosity, *J. Fluid Mech.* 464 (2002) 137–163, <https://doi.org/10.1017/S002211200200856X>.
- [23] J.R. Blake, D.C. Gibson, Cavitation bubbles near boundaries, *Annu. Rev. Fluid Mech.* 19 (1) (1987) 99–123, <https://doi.org/10.1146/annurev.fl.19.010187.000531>.
- [24] M. Kornfeld, L. Suvorov, On the destructive action of cavitation, *J. Appl. Phys.* 15 (6) (1944) 495–506, <https://doi.org/10.1063/1.1707461>.
- [25] T.B. Benjamin, A.T. Ellis, The collapse of cavitation bubbles and the pressures thereby produced against solid boundaries, *Philos. Trans. Royal Soc. A* 260 (1966) 221–240, <https://doi.org/10.1098/rsta.1966.0046>.
- [26] M. Senegačnik, M. Ježeršek, P. Gregorič, Propulsion effects after laser ablation in water, confined by different geometries, *Appl. Phys. A* 126 (2020) 136, <https://doi.org/10.1007/s00339-020-3309-y>.
- [27] M. Dell'Aglio, A. De Giacomo, S. Kohnsawski, S. Barcikowski, P. Wagener, A. Santagata, Pulsed laser ablation of wire-shaped target in a thin water jet: effects of the plasma features and bubble dynamics on the PLAL process, *J. Phys. D Appl. Phys.* 50 (18) (2017) 185204, <https://doi.org/10.1088/1361-6463/aa652a>.
- [28] A. De Giacomo, M. Dell'Aglio, A. Santagata, R. Gaudioso, O. De Pascale, P. Wagener, G.C. Messina, G. Compagnini, S. Barcikowski, Cavitation dynamics of laser ablation of bulk and wire-shaped metals in water during nanoparticles production, *Phys. Chem. Chem. Phys.* 15 (9) (2013) 3083–3092, <https://doi.org/10.1039/C2CP42649H>.
- [29] S. Kohnsawski, B. Gökce, R. Tanabe, P. Wagener, A. Plech, Y. Ito, S. Barcikowski, Target geometry and rigidity determines laser-induced cavitation bubble transport and nanoparticle productivity—a high-speed videography study, *Phys. Chem. Chem. Phys.* 18 (24) (2016) 16585–16593, <https://doi.org/10.1039/C6CP01232A>.
- [30] M. Dell'Aglio, R. Gaudioso, O. De Pascale, A. De Giacomo, Mechanisms and processes of pulsed laser ablation in liquids during nanoparticle production, *Appl. Surf. Sci.* 348 (2015) 4–9, <https://doi.org/10.1016/j.apsusc.2015.01.082>.
- [31] G.C. Messina, P. Wagener, R. Streubel, A. De Giacomo, A. Santagata, G. Compagnini, S. Barcikowski, Pulsed laser ablation of a continuously-fed wire in liquid flow for high-yield production of silver nanoparticles, *Phys. Chem. Chem. Phys.* 15 (9) (2013) 3093–3098, <https://doi.org/10.1039/C2CP42626A>.
- [32] A. De Bonis, M. Sansone, L. D'Alessio, A. Galasso, A. Santagata, R. Teghil, Dynamics of laser-induced bubble and nanoparticles generation during ultra-short laser ablation of Pd in liquid, *J. Phys. D Appl. Phys.* 46 (44) (2013) 445301, <https://doi.org/10.1088/0022-3727/46/44/445301>.
- [33] J. Tomko, J.J. Naddeo, R. Jimenez, Y. Tan, M. Steiner, J.M. Fitz-Gerald, D.M. Bubb, S.M. O'Malley, Size and polydispersity trends found in gold nanoparticles synthesized by laser ablation in liquids, *Phys. Chem. Chem. Phys.* 17 (25) (2015) 16327–16333, <https://doi.org/10.1039/C5CP01965F>.
- [34] T. Tsuji, Y. Tsuboi, N. Kitamura, M. Tsuji, Microsecond-resolved imaging of laser ablation at solid-liquid interface: investigation of formation process of nano-size metal colloids, *Appl. Surf. Sci.* 229 (1–4) (2004) 365–371, <https://doi.org/10.1016/j.apsusc.2004.02.013>.
- [35] P. Gregorič, J. Možina, High-speed two-frame shadowgraphy for velocity measurements of laser-induced plasma and shock-wave evolution, *Opt. Lett.* 36 (2011) 2782–2784, <https://doi.org/10.1364/OL.36.002782>.
- [36] P. Gregorič, J. Diaci, J. Možina, Two-dimensional measurements of laser-induced breakdown in air by high-speed two-frame shadowgraphy, *Appl. Phys. A* 112 (1) (2013) 49–55, <https://doi.org/10.1007/s00339-012-7173-2>.
- [37] Y. Tomita, A. Shima, Mechanisms of impulsive pressure generation and damage pit formation by bubble collapse, *J. Fluid Mech.* 169 (1986) 535–564, <https://doi.org/10.1017/S0022112086000745>.
- [38] A. Vogel, I. Apitz, S. Freidank, R. Dijkink, Sensitive high-resolution white-light Schlieren technique with a large dynamic range for the investigation of ablation dynamics, *Opt. Lett.* 31 (2006) 1812–1814, <https://doi.org/10.1364/OL.31.001812>.
- [39] P. Gregorič, R. Petkovšek, J. Možina, G. Močnik, Measurements of cavitation bubble dynamics based on a beam-deflection probe, *Appl. Phys. A* 93 (4) (2008) 901–905, <https://doi.org/10.1007/s00339-008-4751-4>.
- [40] R. Petkovšek, P. Gregorič, A laser probe measurement of cavitation bubble dynamics improved by shock wave detection and compared to shadow photography, *J. Appl. Phys.* 102 (4) (2007) 044909, <https://doi.org/10.1063/1.2774000>.
- [41] J. Diaci, J. Možina, A study of energy conversion during Nd: YAG laser ablation of metal surfaces in air by means of a laser beam deflection probe, *J. Phys. C* 7 (1994) C7-737–C7-740, <https://doi.org/10.1051/jp4:19947173>.
- [42] J. Diaci, Response functions of the laser beam deflection probe for detection of spherical acoustic waves, *Rev. Sci. Instrum.* 63 (11) (1992) 5306–5310, <https://doi.org/10.1063/1.1143444>.
- [43] A. Matsumoto, A. Tamura, A. Kawasaki, T. Honda, P. Gregorič, N. Nishi, K.-I. Amano, K. Fukami, T. Sakka, Comparison of the overall temporal behavior of the bubbles produced by short- and long-pulse nanosecond laser ablations in water using a laser-beam-transmission probe, *Appl. Phys. A* 122 (2016) 234, <https://doi.org/10.1007/s00339-016-9755-x>.
- [44] S. Ibrahimkuty, P. Wagener, T.D.S. Rolo, D. Karpov, A. Menzel, T. Baumbach, S. Barcikowski, A. Plech, A hierarchical view on material formation during pulsed-laser synthesis of nanoparticles in liquid, *Sci. Rep.* 5 (1) (2015), <https://doi.org/10.1038/srep16313>.
- [45] P. Wagener, S. Ibrahimkuty, A. Menzel, A. Plech, S. Barcikowski, Dynamics of silver nanoparticle formation and agglomeration inside the cavitation bubble after pulsed laser ablation in liquid, *Phys. Chem. Chem. Phys.* 15 (9) (2013) 3068–3074, <https://doi.org/10.1039/C2CP42592K>.
- [46] V. Amendola, M. Meneghetti, What controls the composition and the structure of nanomaterials generated by laser ablation in liquid solution? *Phys. Chem. Chem. Phys.* 15 (9) (2013) 3027–3046, <https://doi.org/10.1039/C2CP42895D>.
- [47] D.R. Lide, *CRC Handbook of Chemistry and Physics, 84th ed.*, CRC Press, 2004.
- [48] G.M. Hale, M.R. Querry, Optical constants of water in the 200-nm to 200- μ m wavelength region, *Appl. Opt.* 12 (1973) 555–563, <https://doi.org/10.1364/AO.12.000555>.
- [49] W.M. Haynes, *CRC Handbook of Chemistry and Physics, 95th ed.*, CRC Press, Oakville, 2014.
- [50] Chemical Engineering Research Information Center. Pure Component Properties. <https://www.chemic.org/research/kdb/hcprop/showprop.php?cmpid=818> (accessed 8 April 2020).
- [51] S. Kedenburg, M. Vieweg, T. Gissibl, H. Giessen, Linear refractive index and absorption measurements of nonlinear optical liquids in the visible and near-infrared spectral region, *Opt. Mater. Express* 2 (11) (2012) 1588, <https://doi.org/10.1364/OME.2.001588>.
- [52] Sigma Aldrich. Poly(ethylene glycol) 300 product datasheet. <https://www.sigmaaldrich.com/catalog/product/sial/81160?lang=en®ion=SI> (accessed 8 April 2020).
- [53] P. Gregorič, J. Zdravec, J. Možina, M. Ježeršek, Optodynamic energy conversion efficiency during laser ablation on metal surfaces measured by shadow photography, *Appl. Phys. A* 117 (1) (2014) 353–357, <https://doi.org/10.1007/s00339-014-8412-5>.
- [54] W. Lauterborn, T. Kurz, R. Geisler, D. Schanz, O. Lindau, Acoustic cavitation, bubble dynamics and sonoluminescence, *Ultrason. Sonochem.* 14 (4) (2007) 484–491, <https://doi.org/10.1016/j.ultsonch.2006.09.017>.
- [55] M. Petkovšek, M. Hočevar, P. Gregorič, Surface functionalization by nanosecond-laser texturing for controlling hydrodynamic cavitation dynamics, *Ultrason. Sonochem.* 67 (2020) 105126, <https://doi.org/10.1016/j.ultsonch.2020.105126>.
- [56] J. Kosel, M. Suštaršič, M. Petkovšek, M. Zupanc, M. Sežun, M. Dular, Application of (super)cavitation for the recycling of process waters in paper producing industry, *Ultrason. Sonochem.* 64 (2020) 105002, <https://doi.org/10.1016/j.ultsonch.2020.105002>.
- [57] P. Gregorič, M. Ježeršek, J. Možina, Optodynamic energy-conversion efficiency during an Er: YAG-laser-pulse delivery into a liquid through different fiber-tip geometries, *J. Biomed. Opt.* 17 (7) (2012) 0750061, <https://doi.org/10.1117/1.JBO.17.7.075006>.
- [58] J.S. Hoppius, S. Maragkaki, A. Kanitz, P. Gregorič, E.L. Gurevich, Optimization of femtosecond laser processing in liquids, *Appl. Surf. Sci.* 467–468 (2019) 255–260, <https://doi.org/10.1016/j.apsusc.2018.10.121>.
- [59] T. Sakka, A. Tamura, A. Matsumoto, K. Fukami, N. Nishi, B. Thornton, Effects of pulse width on nascent laser-induced bubbles for underwater laser-induced breakdown spectroscopy, *Spectrochim. Acta Part B At. Spectrosc.* 97 (2014) 94–98, <https://doi.org/10.1016/j.sab.2014.05.009>.
- [60] M. Može, M. Senegačnik, P. Gregorič, M. Hočevar, M. Zupancič, I. Golobčič, Laser-engineered microcavity surfaces with a nanoscale superhydrophobic coating for extreme boiling performance, *ACS Appl. Mater. Interfaces* 12 (21) (2020) 24419–24431, <https://doi.org/10.1021/acsami.0c01594>.
- [61] J.L. Xu, Y.X. Li, T.N. Wong, High speed flow visualization of a closed loop pulsating heat pipe, *Int. J. Heat Mass Transfer* 48 (16) (2005) 3338–3351, <https://doi.org/10.1016/j.ijheatmasstransfer.2005.02.034>.
- [62] L. Lorbek, A. Kuhelj, M. Dular, A. Kitanovski, Two-phase flow patterns in adiabatic refrigerant flow through capillary tubes, *Int. J. Refrig.* 115 (2020) 107–116, <https://doi.org/10.1016/j.ijrefrig.2020.02.030>.
- [63] M. Prakash, N. Gershenfeld, Microfluidic bubble logic, *Science* 315 (5813) (2007) 832–835, <https://doi.org/10.1126/science.1136907>.
- [64] A. Vogel, V. Venugopalan, Mechanisms of pulsed laser ablation of biological tissues, *Chem. Rev.* 103 (2) (2003) 577–644, <https://doi.org/10.1021/cr010379n>.
- [65] C. Bongiovanni, J.P. Chevallier, J. Fabre, Sizing of bubbles by incoherent imaging: defocus bias, *Exp. Fluids* 23 (3) (1997) 209–216, <https://doi.org/10.1007/s003480050104>.

- [66] C. Bongiovanni, A. Dominguez, J.-P. Chevillier, Understanding images of bubbles, *Eur. J. Phys.* 21 (6) (2000) 561–570, <https://doi.org/10.1088/0143-0807/21/6/307>.
- [67] M.N.R. Ashfold, F. Claeysens, G.M. Fuge, S.J. Henley, Pulsed laser ablation and deposition of thin films, *Chem. Soc. Rev.* 33 (2004) 23–31, <https://doi.org/10.1039/B207644F>.
- [68] G. YANG, Laser ablation in liquids: Applications in the synthesis of nanocrystals, *Prog. Mater. Sci.* 52 (4) (2007) 648–698, <https://doi.org/10.1016/j.pmatsci.2006.10.016>.
- [69] R. Tanabe, T.T.P. Nguyen, T. Sugiura, Y. Ito, Bubble dynamics in metal nanoparticle formation by laser ablation in liquid studied through high-speed laser stroboscopic videography, *Appl. Surf. Sci.* 351 (2015) 327–331, <https://doi.org/10.1016/j.apsusc.2015.05.030>.
- [70] T. Požar, P. Gregorčič, J. Možina, Optical measurements of the laser-induced ultrasonic waves on moving objects, *Opt. Express* 17 (2009) 22906–22911, <https://doi.org/10.1364/OE.17.022906>.
- [71] T.T.P. Nguyen, R. Tanabe, Y. Ito, Laser-induced shock process in under-liquid regime studied by time-resolved photoelasticity imaging technique, *Appl. Phys. Lett.* 102 (12) (2013) 124103, <https://doi.org/10.1063/1.4798532>.
- [72] M. Senegačnik, K. Kunimoto, S. Yamaguchi, K. Kimura, T. Sakka, P. Gregorčič, Dataset supporting journal publication 'Dynamics of laser-induced cavitation bubble during expansion over sharp-edge geometry submerged in liquid – an inside view by diffuse illumination', *Mendeley Data V1* (2021) <https://doi.org/10.17632/w8mpz3v3w2.1>.
- [73] A. Blanco, A. García-Abuín, D. Gómez-Díaz, J.M. Navaza, I. Vidal-Tato, Influence of temperature and composition upon density, viscosity, speed of sound, and refractive index of aqueous solutions of 1-Ethyl-2-pyrrolidinone, *J. Chem. Eng. Data* 55 (2) (2010) 962–965, <https://doi.org/10.1021/jc9003959>.
- [74] H.E. Hoga, R.B. Torres, P.L.O. Volpe, Thermodynamics properties of binary mixtures of aqueous solutions of glycols at several temperatures and atmospheric pressure, *J. Chem. Thermodyn.* 122 (2018) 38–64, <https://doi.org/10.1016/j.jct.2018.02.022>.
- [75] M.H. Rice, J.M. Walsh, Equation of state of water to 250 kilobars, *J. Chem. Phys.* 26 (4) (1957) 824–830, <https://doi.org/10.1063/1.1743415>.
- [76] M.S. Plesset, The dynamics of cavitation bubbles, *J. Appl. Mech.* 16 (1949) 277–282. <https://resolver.caltech.edu/CaltechAUTHORS:20140808-114249321>.
- [77] J. Lam, J. Lombard, C. Dujardin, G. Ledoux, S. Merabia, D. Amans, Dynamical study of bubble expansion following laser ablation in liquids, *Appl. Phys. Lett.* 108 (7) (2016) 074104, <https://doi.org/10.1063/1.4942389>.
- [78] A. Letzel, M. Santoro, J. Frohleiks, A.R. Ziefuß, S. Reich, A. Plech, E. Fazio, F. Neri, S. Barcikowski, B. Gökce, How the re-irradiation of a single ablation spot affects cavitation bubble dynamics and nanoparticles properties in laser ablation in liquids, *Appl. Surf. Sci.* 473 (2019) 828–837, <https://doi.org/10.1016/j.apsusc.2018.12.025>.
- [79] L. Rayleigh VIII, On the pressure developed in a liquid during the collapse of a spherical cavity, *London, Edinburgh Dublin Philos. Mag. J. Sci.* 34 (1917) 94–98, <https://doi.org/10.1080/14786440808635681>.
- [80] R.T. Knapp, Recent investigations of the mechanics of cavitation and cavitation damage, *Trans. ASME* 77 (1955) 1045–1054, [https://doi.org/10.1016/0043-1648\(58\)90220-5](https://doi.org/10.1016/0043-1648(58)90220-5).
- [81] R. Furness, S. Hutton, Experimental and theoretical studies of two-dimensional fixed-type cavities, *J. Fluids Eng.* 97 (1975) 515–521, <https://doi.org/10.1115/1.3448098>.
- [82] D. De Lange, G. De Bruin, Sheet cavitation and cloud cavitation, re-entrant jet and three-dimensionality, *Appl. Sci. Res.* 58 (1997) 91–114, <https://doi.org/10.1023/A:1000763130780>.
- [83] B. Stutz, J.L. Reboud, Experiments on unsteady cavitation, *Exp. Fluids* 22 (3) (1997) 191–198, <https://doi.org/10.1007/s003480050037>.
- [84] Q. Le, J.P. Franc, J.M. Michel, Partial cavities: global behavior and mean pressure distribution, *J. Fluids Eng.* 115 (1993) 243–248, <https://doi.org/10.1115/1.2910131>.
- [85] Y. Kawanami, H. Kato, H. Yamaguchi, M. Tanimura, Y. Tagaya, Mechanism and control of cloud cavitation, *J. Fluids Eng.* 119 (1997) 788–794, <https://doi.org/10.1115/1.2819499>.
- [86] Tim Hupfeld, Gaétan Laurens, Samy Merabia, Stephan Barcikowski, Bilal Gökce, David Amans, Dynamics of laser-induced cavitation bubbles at a solid–liquid interface in high viscosity and high capillary number regimes, *J. Appl. Phys.* 127 (4) (2020) 044306, <https://doi.org/10.1063/1.5116111>.

Supporting Information

Dynamics of laser-induced cavitation bubble during expansion over sharp-edge geometry submerged in liquid – an inside view by diffuse illumination

Matej Senegačnik¹, Kohei Kunimoto², Satoshi Yamaguchi², Koki Kimura², Tetsuo Sakka²,

Peter Gregorčič^{1}*

1- Faculty of Mechanical Engineering, University of Ljubljana, Aškerčeva 6, 1000 Ljubljana,
Slovenia

2- Department of Energy and Hydrocarbon Chemistry, Kyoto University, Nishikyo, Kyoto
615-8510, Japan

Corresponding author:

** E-mail: peter.gregorcic@fs.uni-lj.si (Peter Gregorčič)*

Table of Contents

S1 Sample positioning and illumination

Fig. S1. Breakdown positioning in case of bubble overflow observation (a) from the front (“H” type clamping of the sample) or (b) from the side (“L” type clamping of the sample). The camera is located at the opposite side of the sample as illumination. Black lines in the corresponding acquired images represent 500 μm .

Fig. S2. Temporal intensity profile of diffuse illumination source (flashlamp) that is used in experimental setup #1.

S2 Ray tracing model

Fig. S3. Determining points of intersection with the bubble wall.

Fig. S4. (a) Total reflection and (b) refraction of a light ray at the bubble wall.

Fig. S5. Reflectivity of light for different angles of incidence when passing from (a) cavitation bubble (water vapor) into liquid (water) and (b) vice versa.

Fig. S6. Determining new rays after reaching the intersection point. Reflectivity R is determined from the Fresnel relations considering polarization orientation.

Fig. S7. Parameters in ray transfer matrix of objective lens.

Fig. S8. Ray tracing simulations of collimated illumination with 50 parallel initial rays. (a) s- and (b) p-polarizations are considered. Brightness of the lines corresponds to relative intensity of the ray, ranging from 0 (white) to 1 (black). Characteristic rays of types #1, #2, and #4 are presented in (a) with red, green, and pink color, respectively.

Fig. S9. (a) Sections (intervals) of collimated illumination source that contribute (by superposition) to (b) the total irradiance profile of the vapor bubble in water. Individual contribution of ray types #1-#4 is shown in (c)-(f), respectively.

Fig. S10. Images of the same static air bubble acquired by (a) p-polarized and (b) s-polarized collimated (laser) back illumination (experimental setup #2). Brightness and contrast of the image are significantly increased in (c) and (d), respectively, for better visibility of the bright ring. Image brightness profiles, deducted from (a) and (b) are shown in (e) and (f), while simulated irradiance profiles are presented in (g) and (h), respectively.

Fig. S11. (a) Ray tracing simulation of collimated illumination incident at 45° (with respect to the horizontal optical axis). Images of the same static air bubble are acquired by collimated back illumination with the angle of incidence equal to (b) 0° and (c) 45° (from the left) with respect to the optical axis. (c) Image brightness profile deducted from (b) and (c) at locations that are marked by the horizontal arrows.

Fig. S12. Images of the same static air bubble in water acquired by (a) collimated (laser) and (b) diffuse (flashlamp) back illumination. Their corresponding image brightness profiles are presented in (c). (d) Comparison between the measured brightness profile [deducted from (b)] and the simulated irradiance profile.

S3 Shockwave and bubble dynamics

Fig. S13. Shockwave evolution over the edge of the stainless steel sample after laser pulse irradiation at $l = 0.3$ mm from the edge. Surrounding liquids are (a) water and (b) PEG. Pulse energy equals 10.6 mJ. White line in the inset image at 162 ns marks 100 μm .

Fig. S14. Shockwave front radius with respect to time after breakdown in water (black) and PEG (red). Dots represent experimentally determined values, while solid lines show the curves fitted by Eq. (S12).

Fig. S15. Shockwave propagation velocity with respect to time after breakdown in water (black) and PEG (red). Curves are derived from the fitted curves in Fig. S14 by using Eq. (S14).

Fig. S16. Bubble radius with respect to time after breakdown in water (black) and PEG (red). Dots represent experimentally determined values, while solid lines show the curves that are fitted by using Eq. (S15).

Fig. S17. Bubble wall velocity as a function of time after breakdown in water (black) and PEG (red).

Fig. S18. Pressure at the shockwave front and at the bubble wall as a function of time after breakdown in water (black) and PEG (red). Results for the bubble are calculated from the curves in Fig. S16 by using Eq. (S17).

Fig. S19. Pressure at the shockwave front and at the bubble wall as a function of radius in water (black) and PEG (red).

Table S2. Free fitting parameters obtained by fitting Eqs. (S12) and (S15) to the experimental measurements of shockwave and bubble radii.

S4 Development of secondary cavity

Fig. S20. Development of secondary cavity in water at 10 mJ pulse energy.

Fig. S21. Development of secondary cavity in water at 25 mJ pulse energy.

Fig. S22. Development of secondary cavity in water at 55 mJ pulse energy.

Fig. S23. Development of secondary cavity in ethanol at 10 mJ pulse energy.

Fig. S24. Development of secondary cavity in ethanol at 25 mJ pulse energy.

Fig. S25. Development of secondary cavity in ethanol at 55 mJ pulse energy.

Fig. S26. Development of secondary cavity in PEG at 10 mJ pulse energy.

Fig. S27. Development of secondary cavity in PEG at 25 mJ pulse energy.

Fig. S28. Development of secondary cavity in PEG at 55 mJ pulse energy.

S5 Liquid injection into the cavitation bubble

Fig. S29. Imaging of the liquid injection in ethanol from the side (same parameters as in Fig. 7c).

Fig. S30. Direct comparison of bubble dynamics induced in (a) water, (b) ethanol, and (c) PEG under same conditions. Image (c) is only illuminated from the back due to technical issues that could not be addressed in due time.

Fig. S31. Bubble dynamics of bubbles induced in (a) water ($l = 0.2$ mm) and (b) ethanol ($l = 0.3$ mm). Laser pulse energy equals 25 mJ.

Fig. S32. Asymmetrical re-entrant injection dynamics in a bubble induced at $l = 1.1$ mm in water. Laser pulse energy equals 25 mJ.

Fig. S33. Re-entrant injection dynamics in bubbles induced at $l = 0.4$ mm – 1.7 mm in (a-d) water and (e-h) ethanol. Laser pulse energy equals 25 mJ. Note the different time scale of (d) and (h) compared to others.

Fig. S34. Comparison of liquid injections in ethanol induced by laser pulses with pulse energies of (a) 10 mJ and (b) 25 mJ. Distance between the breakdown and the edge equals 0.3 mm.

Fig. S35. Comparison of liquid injections in ethanol for pulse energies of (a) 10 mJ, (b) 25 mJ, and (c) 55 mJ. The breakdown-edge distance equals 0.9 mm.

Fig. S36. Double breakdown in ethanol at pulse energy of 55 and $l = 0.6$ mm.

S6 Influence of sample thickness

Fig. S37. Comparison of the bubble dynamics in water at different thicknesses of the samples. Pulse energy equals 25 mJ. Breakdown is induced in the middle of the sample with thickness of (a) 25 μ m, (b) 0.38 mm, (c) 1 mm, and (d) 2 mm.

References

S1 Sample positioning and illumination

Observation of laser-induced cavitation bubble overflow over the edge was performed from two perspectives. In order to observe the dynamics that takes place inside the cavitation bubble, the process was observed *from the front* (Fig. S1a). In this case, the sample was clamped in an “H” configuration and the position of breakdown spot was coincident with the optical axis of the camera. In this configuration, the breakdown-edge distance l equals a .

Bubble expansion over the edge was monitored also *from the side* (Fig. S1b). Here, the breakdown spot was positioned out of the optical axis of the camera, which was collinear with the edge of the sample, as depicted in Fig. S1b. The sample was clamped in an “L” configuration. In this case, the breakdown-edge distance l equals b .

The focus of the image was set depending on desired observation. In case of the side-view, the object plane (i.e., the plane that appears sharp in the image) was set to coincide with the breakdown spot, as this is the plane that casts the shadow in our shadowgraphical experiment. In case of observation from the front, the surface of the sample that is nearer to the camera was set in focus, in order to observe the liquid injections that occur in this plane. Experiments with larger breakdown-edge distance in case of frontal observation therefore exhibit blurry bubble wall due to deliberate defocus (see Figs. S33d,h at 4 μ s).

Dynamics of cavitation bubbles was captured by two different systems, explained in the main text. Illumination was utilized either by 30 ps laser pulses or by diffuse light source with pulse duration of ~ 1 ms. Temporal intensity profile of diffuse illumination source (flashlamp) that was used in experimental setup #1 is presented in Fig. S2.

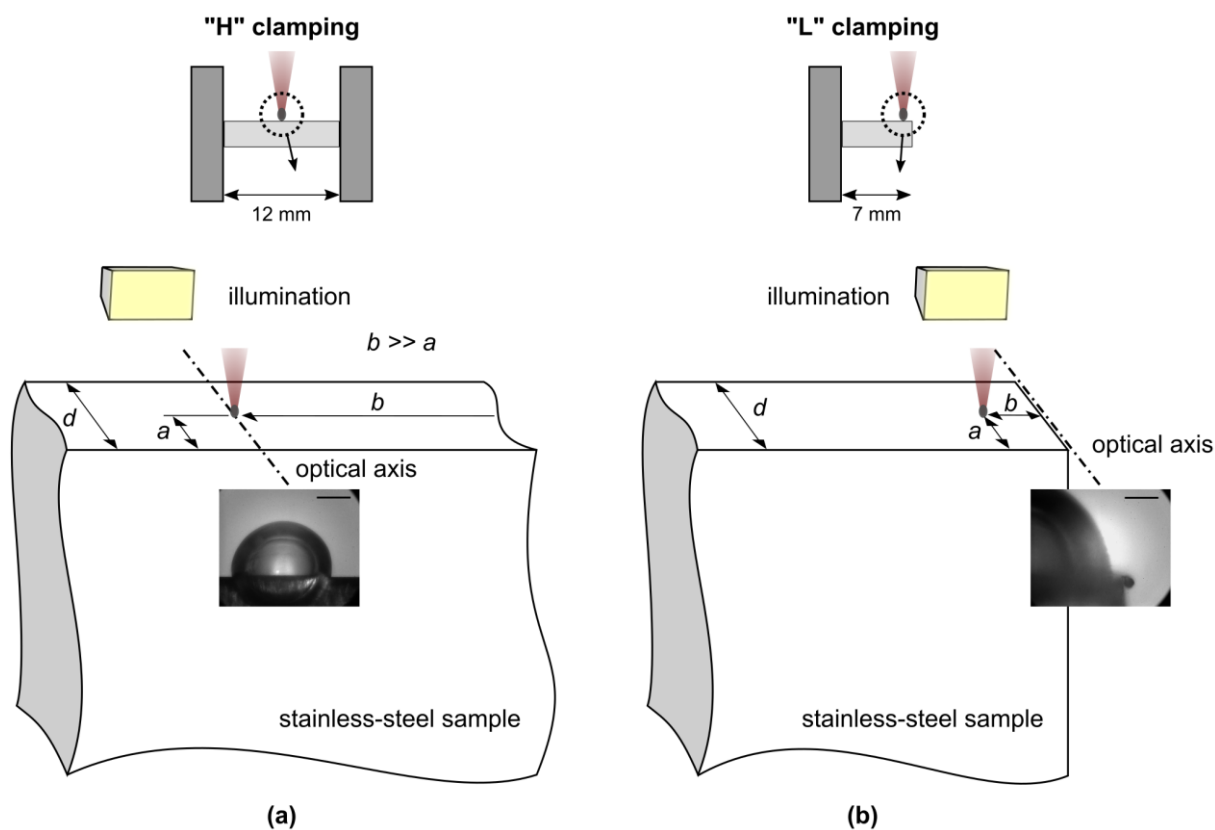


Fig. S1. Breakdown positioning in case of bubble overflow observation (a) from the front (“H” type clamping of the sample) or (b) from the side (“L” type clamping of the sample). The camera is located at the opposite side of the sample as illumination. Black lines in the corresponding acquired images represent 500 μm .

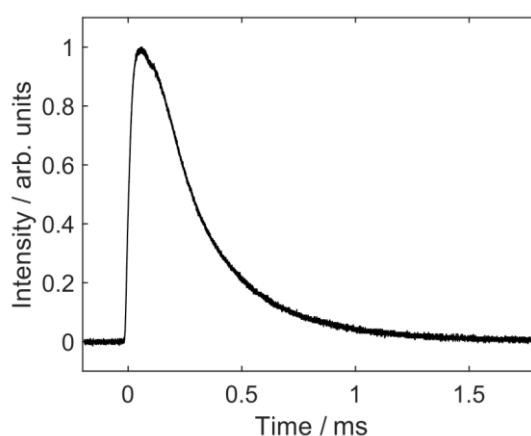


Fig. S2. Temporal intensity profile of diffuse illumination source (flashlamp) that is used in experimental setup #1.

S2 Ray tracing model

For clarifying the role of illumination diffusivity in bubble imaging, we developed a numerical model in Matlab. The model bases on laws of geometrical optics and simulates the trajectories of illuminating rays when passing through interfaces with different optical densities (i.e., bubble-liquid interfaces). The bubble of a radius R_b is assumed to contain vapor with refractive index $n_2 = 1$. Considered surrounding liquids are water and polyethylene glycol 300 (PEG) with refractive indices $n_1 = 1.33$ and $n_1 = 1.465$, respectively.

Rays in the simulation are characterized by the point of origin $O(x, y)$, normalized propagating vector \vec{l} (pointing from the origin in direction of the ray propagation), relative intensity I , and refractive index of the medium the ray originates in. The geometry is defined in Cartesian coordinate system with bubble centered at the origin of the coordinate system, as shown in Fig. S3. Describing the ray by an equation of the geometrical line $y = kx + a$ and bubble wall as a circle with equation $x^2 + y^2 = R_b^2$, the points of intersection can be found from solutions of the quadratic formula

$$x_{1,2} = \frac{-B \pm \sqrt{B^2 - 4AC}}{2A}, \quad (\text{S1})$$

where coefficients A, B, and C are calculated as

$$A = k^2 + 1 \quad (\text{S2})$$

$$B = 2ka \quad (\text{S3})$$

$$C = a^2 - R_b^2 \quad (\text{S4})$$

In general, this gives two solutions (intersection points), where the searched solution represents the point closer to the ray's origin $O(x, y)$.

Once the point of intersection with the bubble wall is determined, the angle of incidence in this point can be calculated. Depending on the ray direction that is described by the normalized vector \vec{l} and the normal of the bubble wall described by the vector \vec{n} , the angle of incidence θ_i equals

$$\theta_i = \cos^{-1}(-\vec{n} \cdot \vec{l}) \quad (\text{S5})$$

where normal \vec{n} is defined by

$$\vec{n} = \frac{(x, y)}{R_b} \quad (\text{S6})$$

and x, y in Eq. (S6) stand for the coordinates of the intersection point at the bubble wall. In this point, the ray can either be totally reflected or refracted depending on the angle of incidence, as depicted in Fig. S4.

In case of total reflection, the reflected ray retains the intensity of the incident ray, while the direction of travel is symmetric with respect to the normal \vec{n} . In case of light refraction, however, part of the ray is reflected with decreased intensity, while the remaining part is refracted inside the opposing medium. The angle of refraction θ_t is described by the Snell's law

$$\theta_t = \sin^{-1}\left(\frac{n_1}{n_2} \sin \theta_i\right). \quad (\text{S7})$$

In case of light refraction, the amount of reflected light depends on the angle of incidence and the ratio of optical densities, as well as the direction of light polarization with respect to the plane of incidence. The reflectivity of s- and p-polarized light is described by Fresnel equations [S1]:

$$R_s = \frac{\sin^2(\theta_i - \theta_t)}{\sin^2(\theta_i + \theta_t)} \quad (\text{S8})$$

$$R_p = \frac{\tan^2(\theta_i - \theta_t)}{\tan^2(\theta_i + \theta_t)}, \quad (\text{S9})$$

in which indices s and p stand for the type of polarization. Here, s-polarization (called also TE) denotes that the electric field is oscillating perpendicular to the plane of incidence, while for p-polarization (called also TM) it oscillates parallel to the plane of incidence. The reflectivity of unpolarized light R_{up} can be calculated as the average reflectivity of both polarization types, yielding

$$R_{\text{up}} = \frac{R_s + R_p}{2} \quad (\text{S10})$$

Reflectivity of light for both types of polarization in dependence of the angle of incidence for cavitation bubble interface in water is presented in Fig. S5.

Following Eqs. (S7)-(S10) and characteristics of the light ray it is straightforward to define new rays with appropriate direction and intensity after the existing ray reaches the interface, as shown in Fig. S6. The process is then repeated for each newly determined ray as long as its intensity is above 1 % of the initial (illumination) ray.

After interacting with the bubble, (some of) the rays travel through the system of objective lens (the others are lost and do not reach the imaging plane). The objective is modeled with a thin lens and simulated by a ray transfer matrix. According to the objective focal length f , distance y and angle θ of the output rays with respect to the optical axis can be described by a system of linear equations as

$$\begin{pmatrix} y_2 \\ \theta_2 \end{pmatrix} = \begin{bmatrix} 1 & 0 \\ -\frac{1}{f} & 1 \end{bmatrix} \begin{pmatrix} y_1 \\ \theta_1 \end{pmatrix}, \quad (\text{S11})$$

where indices 1 and 2 stand for input and output of the lens, respectively (Fig. S7).

The diameter of the lens a (representing also the aperture dimension) and its position with respect to the cavitation bubble x_{obj} were determined by measurements. Similarly, position x_{sen} and width of the sensor w were considered and incorporated into the model, presented in Fig. 2 of the main text. The line of pixels in the sensor is simulated as intervals with the size equal to physical pixel width. Numerical values of these parameters, which were considered in the simulations of diffuse and collimated illumination of experimental systems #1 and #2, are listed in Table S1. By counting the number of rays that intersect with each interval, relative irradiance profile is determined. Due to inconsistent number of rays and their density in the simulations of different illumination sources, the final irradiance profile is normalized to the average irradiance of the background without the bubble.

An example of ray tracing for a collimated illumination through a bubble wall (the red circle) with 50 initial rays is presented in Fig. S8. Both s- and p-polarization are considered in Figs. S8a and S8b, respectively. Typical rays that reach the sensor are labeled only in Fig. S8a. The black points indicate the origins of the starting rays. Brightness of the rays (in grayscale) is

proportional to their intensity, determined from the Fresnel relations [Eqs. (S8)–(S10)]. Black color indicates higher intensity. When simulating the irradiance profile (shown in Fig. 3 in the main text and in Figs. S9, S10, and S12), simulations were performed with a much higher number of initial rays (10^5 – 2×10^6), to minimize the effect of discretization.

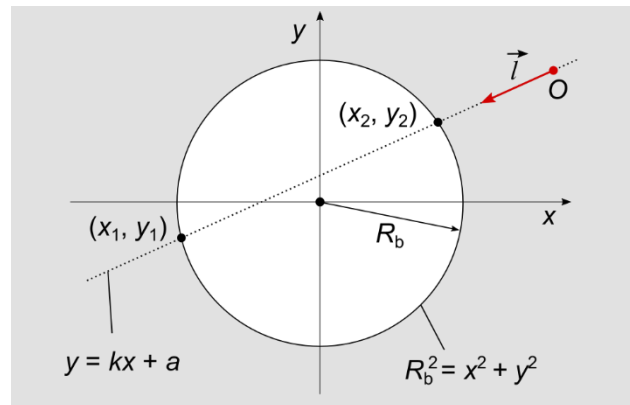


Fig. S3. Determining points of intersection with the bubble wall.

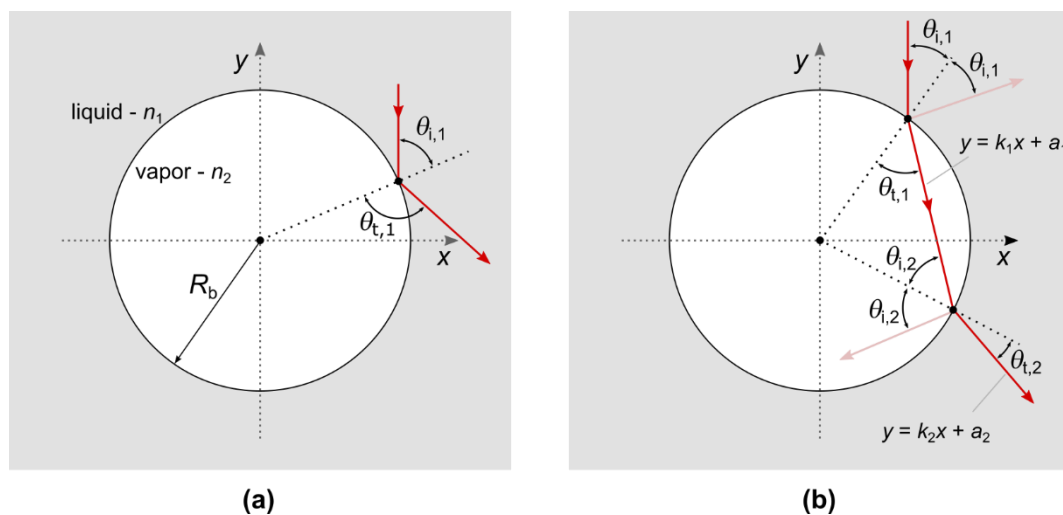


Fig. S4. (a) Total reflection and (b) refraction of a light ray at the bubble wall.

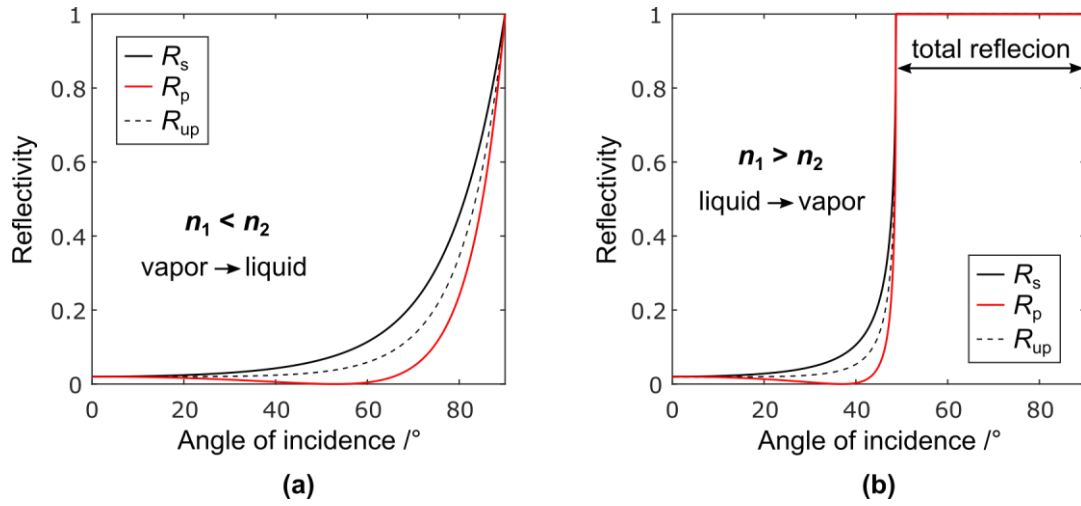


Fig. S5. Reflectivity of light for different angles of incidence when passing from (a) cavitation bubble (water vapor) into liquid (water) and (b) vice versa.

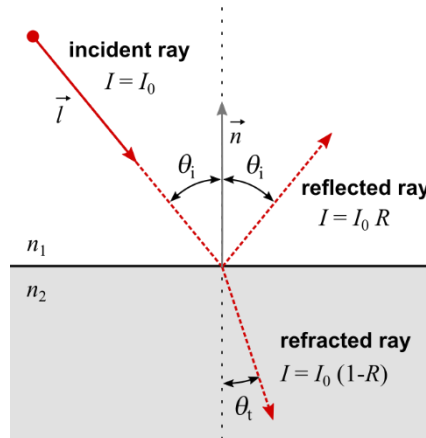


Fig. S6. Determining new rays after reaching the intersection point. Reflectivity R is determined from the Fresnel relations considering polarization orientation.

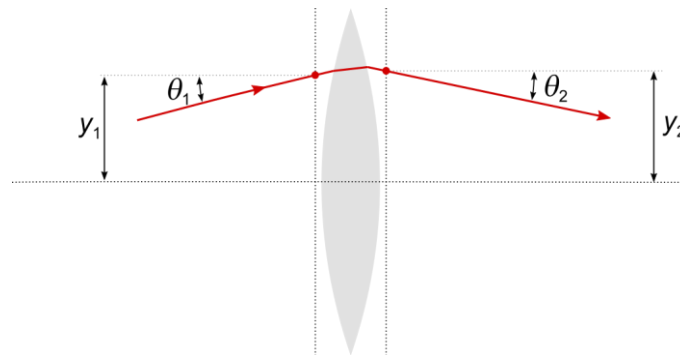


Fig. S7. Parameters in ray transfer matrix of objective lens.

Table S1. Parameters used in modelling of irradiance profiles for diffuse (experimental system #1, Fig. 3f in the main text) and collimated (experimental system #2, Fig. 3d in the main text) illumination of a vapor bubble with $R_b = 0.7$ mm.

Parameter	f /mm	L /mm	ΔL / μm	α /rad	$\Delta\alpha$ /mrad	x_{is} /mm
Diffuse (exp. sys. #1)	20	2.6	87	0.8	16	-0.8
Collimated (exp. sys. #2)	50	2.6	26	0	0	-0.8

Parameter	x_{obj} /mm	x_{sen} /mm	a /mm	w /mm	pixel size / μm
Diffuse (exp. sys. #1)	22	242	11.2	20.8	66.5
Collimated (exp. sys. #2)	67	264	11.2	6.1	4.8

S2.1 Contribution of different ray types

Irradiance profile obtained by collimated unpolarized illumination is presented in Fig. S9, where the total irradiance (Fig. S9b) is decomposed to contributions of each type of rays #1-#4 (Figs. S9c-S9f). In addition to schematic presentation of ray types with different colors, Fig. S9a also shows their corresponding origin in terms of starting coordinate y with respect to the bubble radius R_b . The intervals of origins of different ray types are schematically presented in Fig. S9a by highlighted bands. Illuminating rays that originate outside of these intervals (indicated by vertical arrows in Fig. S9a) are either reflected (section between #2 and #3) or refracted (section between #1 and #2) out of the aperture of the objective lens and therefore do not reach the sensor. Clearly, the intervals of ray types are unique for individual optical setup due to different size proportions, apertures of the objective lens, as well as optical densities of the observed media. Nevertheless, considering our optical setup for collimated illumination (experimental setup #2) and assuming illumination of a vapor bubble with radius $R_b = 1$ mm in water, only the rays that originate from the following coordinates y reach the sensor: $(0 < y < 0.12R_b)$ for rays #1, $(0.69R_b < y < 0.75R_b)$ for rays #2, $(0.999R_b < y < R_b)$ for rays #3, and $(R_b < y)$ for rays #4.

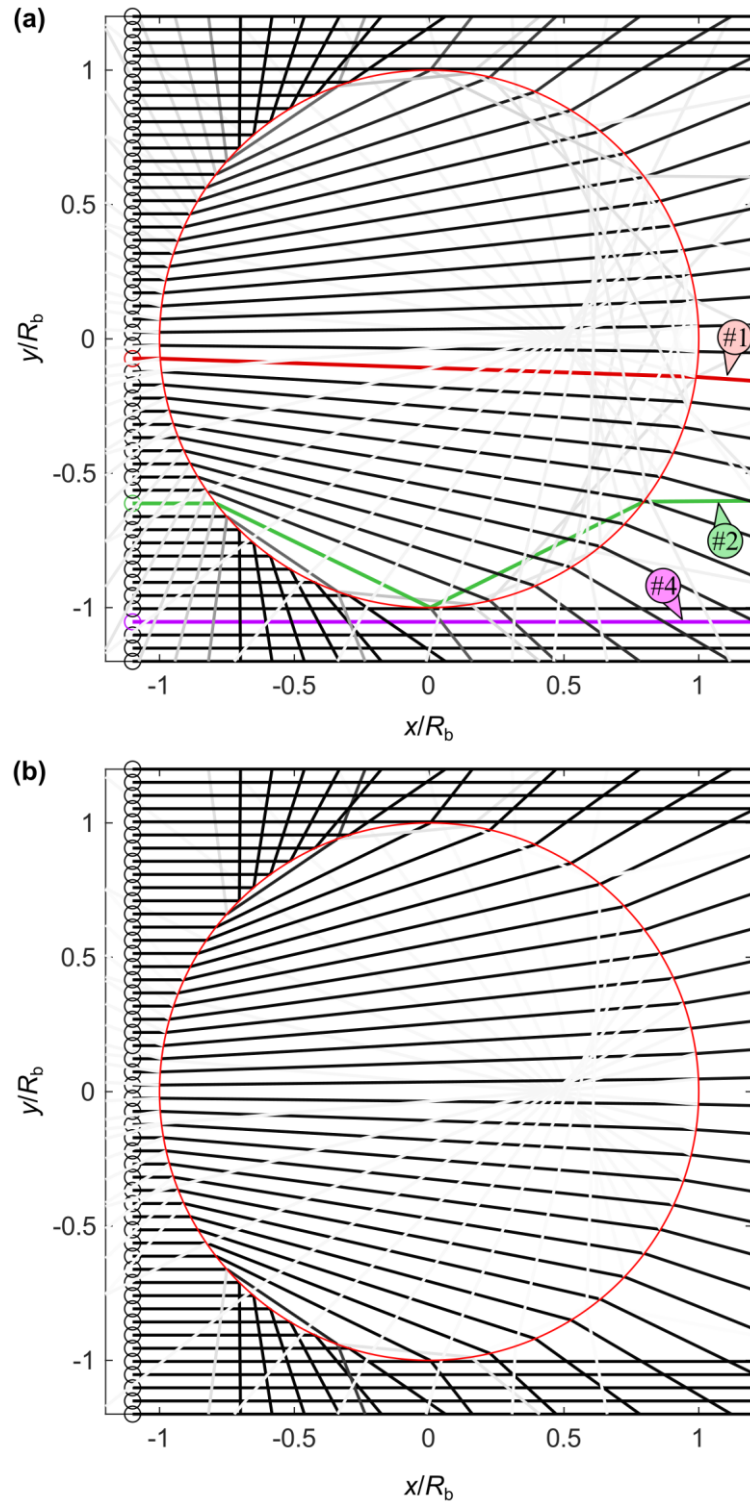


Fig. S8. Ray tracing simulations of collimated illumination with 50 parallel initial rays. (a) s- and (b) p-polarizations are considered. Brightness of the lines corresponds to relative intensity of the ray, ranging from 0 (white) to 1 (black). Characteristic rays of types #1, #2, and #4 are presented in (a) with red, green, and pink color, respectively.

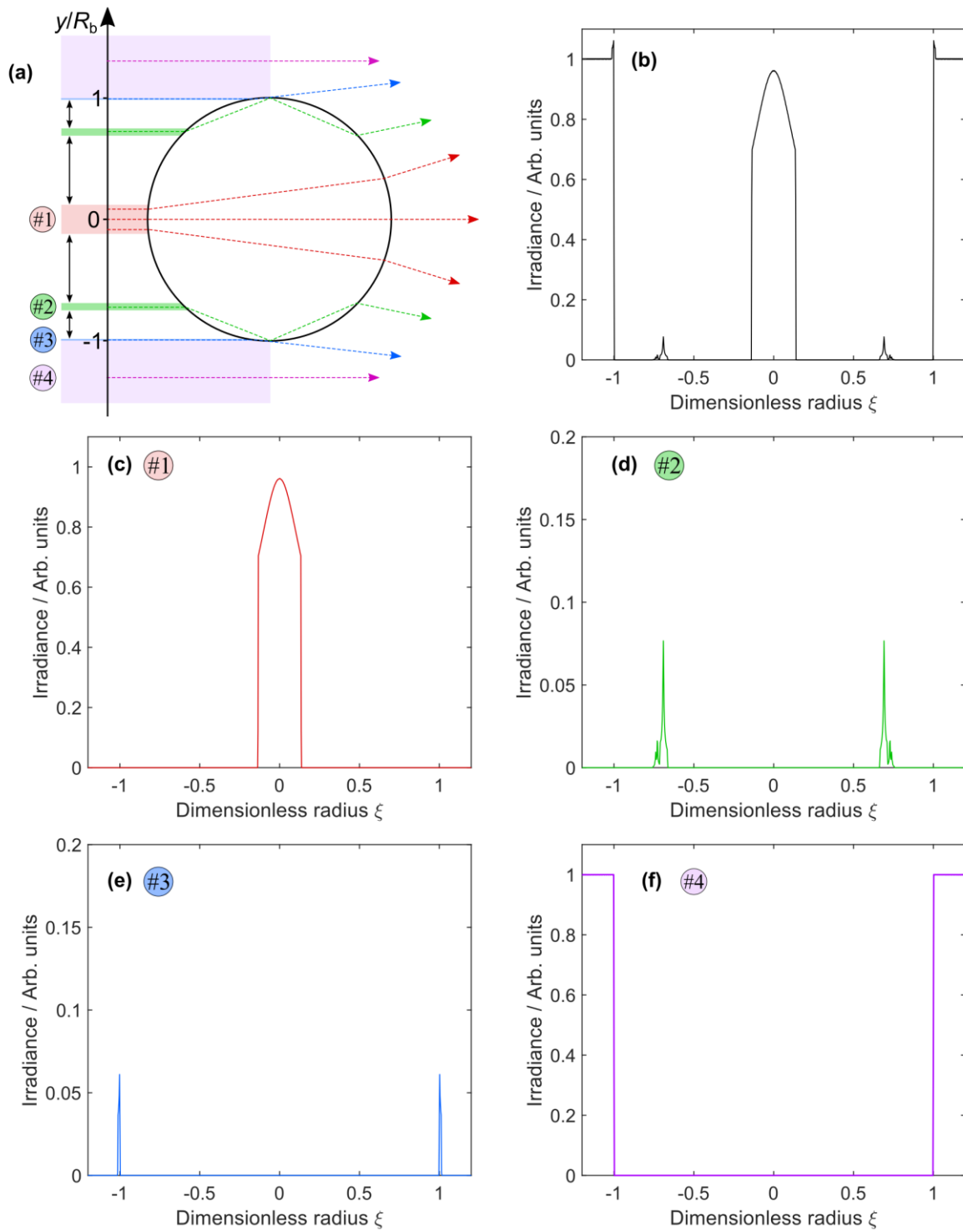


Fig. S9. (a) Sections (intervals) of collimated illumination source that contribute (by superposition) to (b) the total irradiance profile of the vapor bubble in water. Individual contribution of ray types #1-#4 is shown in (c)-(f), respectively.

S2.2 Influence of light polarization

The effect of light polarization is most noticeable in the bright ring that appears due to light reflections inside the bubble (type #2 rays; Fig. S9d). The rays that contribute to formation of the ring are those that reflect inside the bubble multiple times before exiting. Therefore, reflectivity plays an important role in determining the brightness of the perceived ring (shown in Fig. S5a). Considering Fresnel relations [Eqs. (S8)–(S9)], higher reflectivity of the s-polarized light at the bubble wall yields higher intensity of the light “transmitted” through the bubble by reflections, which can be detected as increased brightness of the ring. In case of linearly polarized illumination of a spherical bubble, the brightness of the ring should therefore not be equal all around the ring, but rather symmetrical with respect to polarization. In order to prove this experimentally, a static air bubble was appended to the surface of the sample, held together merely by surface tension. The same bubble was further illuminated with different illumination conditions, making results directly comparable.

The effect of rotating the direction of the linear polarization of illumination light is shown in Fig. S10. Here, the static bubble is illuminated with horizontally (Fig. S10a) and vertically (Fig. S10b) oriented polarizations. Albeit the illumination intensity is not equal in both images, the image brightness profiles were deducted from the acquired images at the location marked by horizontal arrows in Figs. S10a and S10b. It can be seen from corresponding image brightness profiles in Figs. S10e and S10f, that the bright ring (resulting from reflections inside the bubble, marked by vertical arrows at $|\xi| \sim 0.7$) is brighter in case of vertical polarization, which presents s-polarization with respect to the horizontal plane (plane of image brightness profile). Should we deduct the image brightness profile in the vertical direction, very similar results would be obtained, however this time the brighter ring would be detected with horizontal polarization, since horizontal polarization would now represent s-polarization. The latter can be easily distinguished from acquired images with increased brightness and contrast, where the ring in Fig. S10c appears brightest at the top, while in Fig. S10d it is noticeably brighter at the sides. The obtained results also agree with simulated irradiance profiles in Figs. S10g and S10h.

Irradiance of the central part of the bubble is fairly unaffected by direction of polarization due to low angle of incidence of (type #1) illuminating rays at the bubble interface, which results in practically same reflectivity of both types of polarization (Fig. S5, angles of incidence $< 20^\circ$).

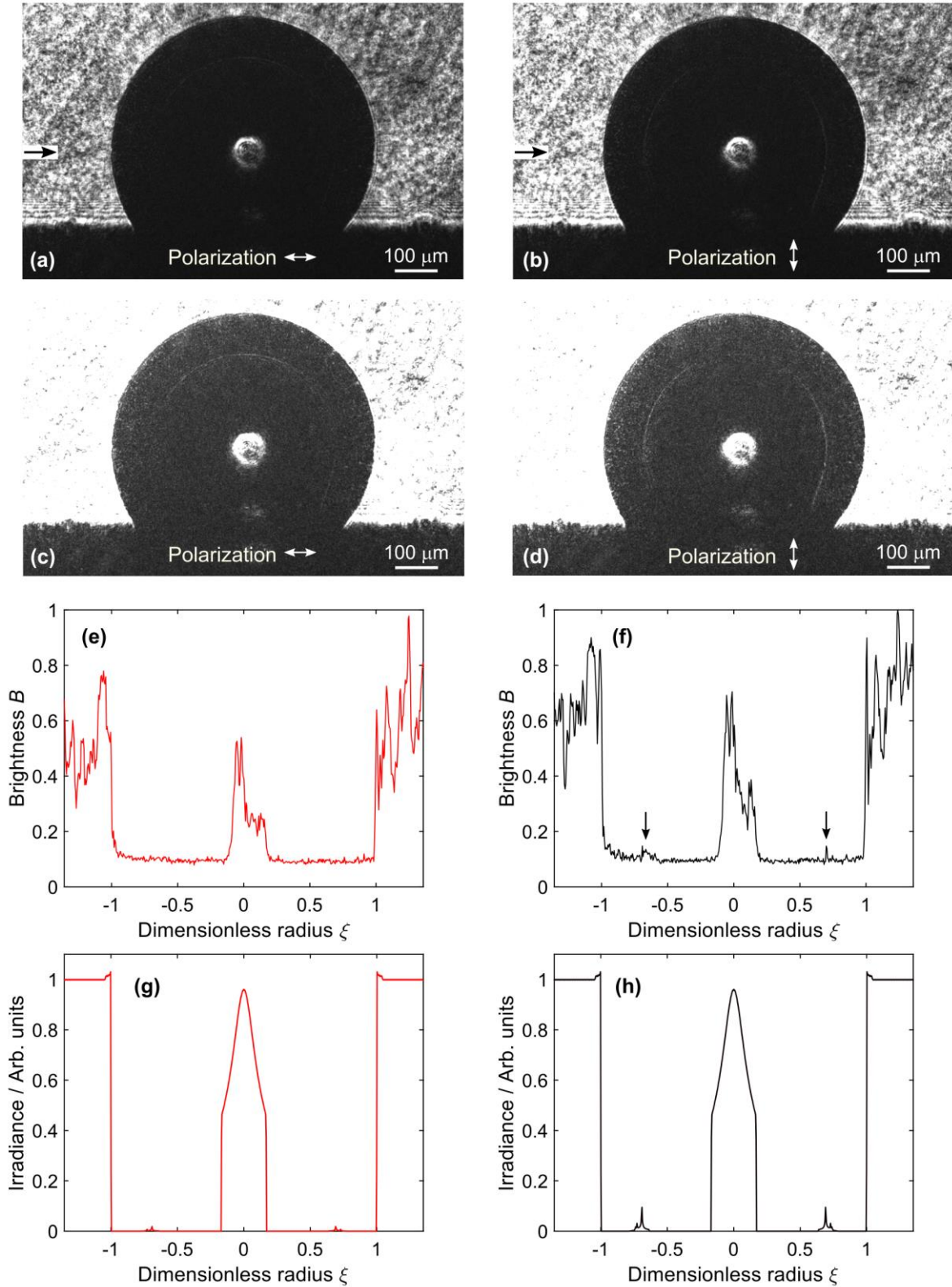


Fig. S10. Images of the *same* static air bubble acquired by (a) p-polarized and (b) s-polarized collimated (laser) back illumination (experimental setup #2). Brightness and contrast of the image are significantly increased in (c) and (d), respectively, for better visibility of the bright ring. Image brightness profiles, deducted from (a) and (b) are shown in (e) and (f), while simulated irradiance profiles are presented in (g) and (h), respectively.

S2.3 Influence of angle of incidence

Similar to previous experiments with different polarizations, a static air bubble appended to the sample surface was observed with different illuminating conditions to enable direct comparison of the results. Figure S11 shows the effect of illuminating a bubble with a collimated light source incident at 0° (Fig. S11b) and 45° (Fig. S11c) with respect to the optical axis. As visible from Fig. S11c, illuminating by an angle of 45° (from the left) leads to formation of only two bright spots in the image sensor. The outer spot (in this case the left one) is caused by total reflection of light rays at the outer bubble wall (ray type #3), as shown in the ray tracing simulation in Fig. S11a. The position of the peak of this bright spot with respect to the bubble wall depends on the angle of incidence – higher angle yields formation of the spot closer to the bubble center. When diffuse illumination source is used for illuminating the bubble, these reflections were shown [S2] to cause a sizing error of up to 30 % for an infinitely large plane source (with emitting angle $\alpha = 180^\circ$). Considering our optical setup for collimated illumination (experimental setup #2) and illumination from 45° , the peak of this “wall reflection” spot is detected at $\xi \sim -0.92$, as seen in Fig. S11d. Should the illumination be incident at the same angle from the right instead of from the left, the result would be equal but mirrored over the vertical axis.

The second bright spot, closer to the center of the bubble (peak at $\xi \sim -0.58$), results from rays that travel through the bubble by either only refraction (type #1) or also reflection at the inner bubble wall (type #2), as shown in Fig. S11a. Compared to rays reflected off the outer bubble wall (type #3), these travel through the bubble and thus increase the illuminated area inside the bubble, broadening the view of phenomena occurring inside. Type #4 rays in the meantime travel out of the aperture of objective due to their large angle of incidence – the background is dark.

A diffuse illumination source can also be considered as a sum of many collimated sources that are incident at different angles, which was also implemented in our ray tracing model. Figure S12 shows experimental comparison of illuminating the same static air bubble with a collimated (i.e., laser) source (Fig. S12a) and a diffuse (i.e., flashlamp) source (Fig. S12b). Deducted image brightness profiles in Fig. S12c confirm the difference in irradiance gradient at the bubble wall ($|\xi| \sim 1$). It is clearly seen that the edge of the bubble in case of diffuse illumination becomes blurred due to contribution of direct (type #4) rays that travel beside the bubble wall at an angle, as well as reflections off the outer bubble wall (type #3), as explained in Fig. S11d. By

measuring only the apparent (darkened) part of the bubble, we estimate up to around 5% error in size determination can be made (with common optical setups, such as our experimental setup #1) due to wrong interpretation of the irradiance profile.

Experiments agree well with the simulated results. Figure S12d shows the simulated irradiance profile compared to the measured one with reduction of background noise (zero irradiance is assumed at brightness level that equals to 0.2). The emitting angle of illumination source considered in the simulation is assumed to equal 0.4 rad with respect to the optical axis. The most significant deviation of the simulated irradiance profile from the experimentally determined one is in the intensity profile of the central irradiated part of the bubble (rays #1). The simulated irradiance in this part exhibits a fairly constant value, while the experimental values show that the intensity decreases from the bubble's center outward. The deviation can be explained by angular intensity distribution of the illumination source, which determines the intensity of rays that are incident at different angles. Since the widening of the central illuminated area in the bubble can be attributed mostly to type #1 rays that are incident at higher angles, the irradiance in this part depends on their intensity. The angular intensity distribution of the source is assumed a "pillbox" distribution in the simulations, meaning constant intensity through all angles of incidence. True angular intensity distribution of the flashlamp illumination used in the experiments, however, most likely decreases with the angle. This leads to a more noticeable decrease in irradiance (at roughly $0.15 < |\zeta| < 0.5$ in Fig. S12d) compared to the simulation.

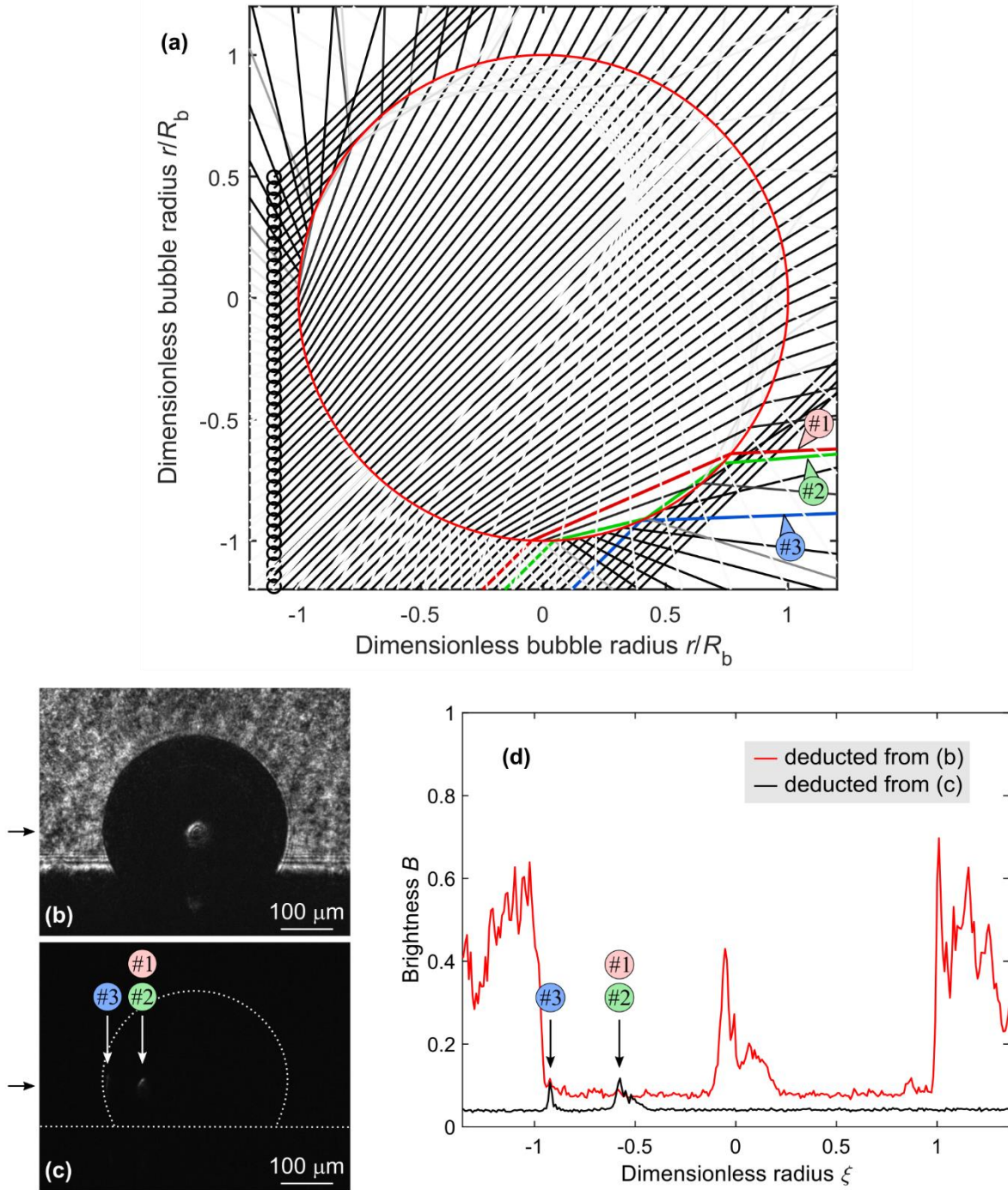


Fig. S11. (a) Ray tracing simulation of collimated illumination incident at 45° (with respect to the horizontal optical axis). Images of the *same* static air bubble are acquired by collimated back illumination with the angle of incidence equal to (b) 0° and (c) 45° (from the left) with respect to the optical axis. (d) Image brightness profile deducted from (b) and (c) at the locations marked by horizontal arrows.

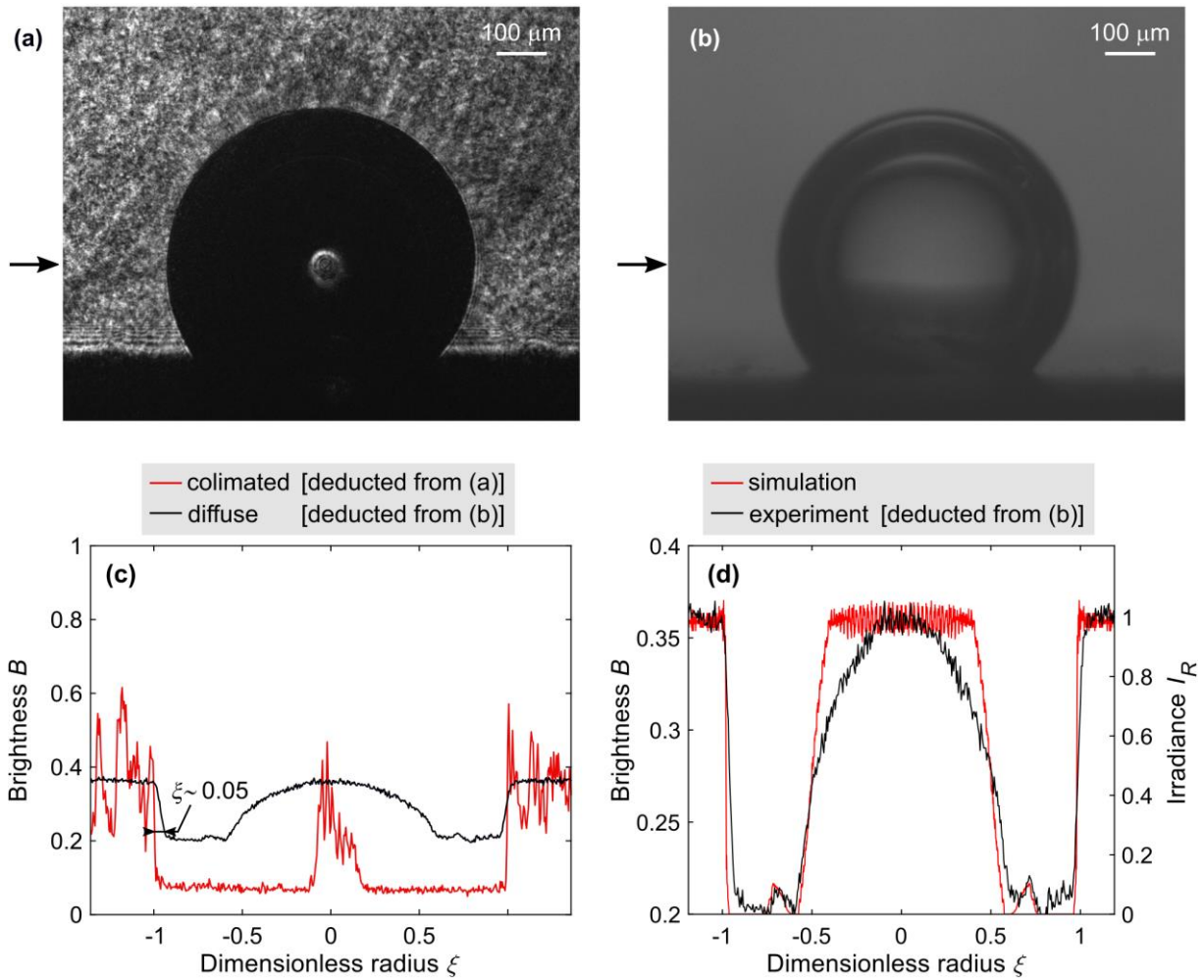


Fig. S12. Images of the *same* static air bubble in water acquired by (a) collimated (laser) and (b) diffuse (flashlamp) back illumination. Their corresponding image brightness profiles are presented in (c). (d) Comparison between the measured brightness profile [deducted from (b)] and the simulated irradiance profile.

S3 Shockwave and bubble dynamics

In order to characterize and evaluate the dynamics occurring within the first few microseconds after the excitation, radii of the shockwave and cavitation bubble were measured from the images (Fig. S13) acquired by experimental setup #2 with great temporal resolution. Multiple breakdown events were captured at different time instances after the excitation pulse to capture a temporal evolution of the laser-induced phenomena. Experiments were performed in water (Fig. S13a) and PEG (Fig. S13b).

A sudden release of energy after an excitation-laser pulse is absorbed in the metal and leads to formation of plasma and, consequently, to explosive expansion of the surrounding medium. This results in *(i)* shockwave formation, which ultrasonically propagates into the liquid outward from the breakdown position and *(ii)* development of a cavitation bubble.

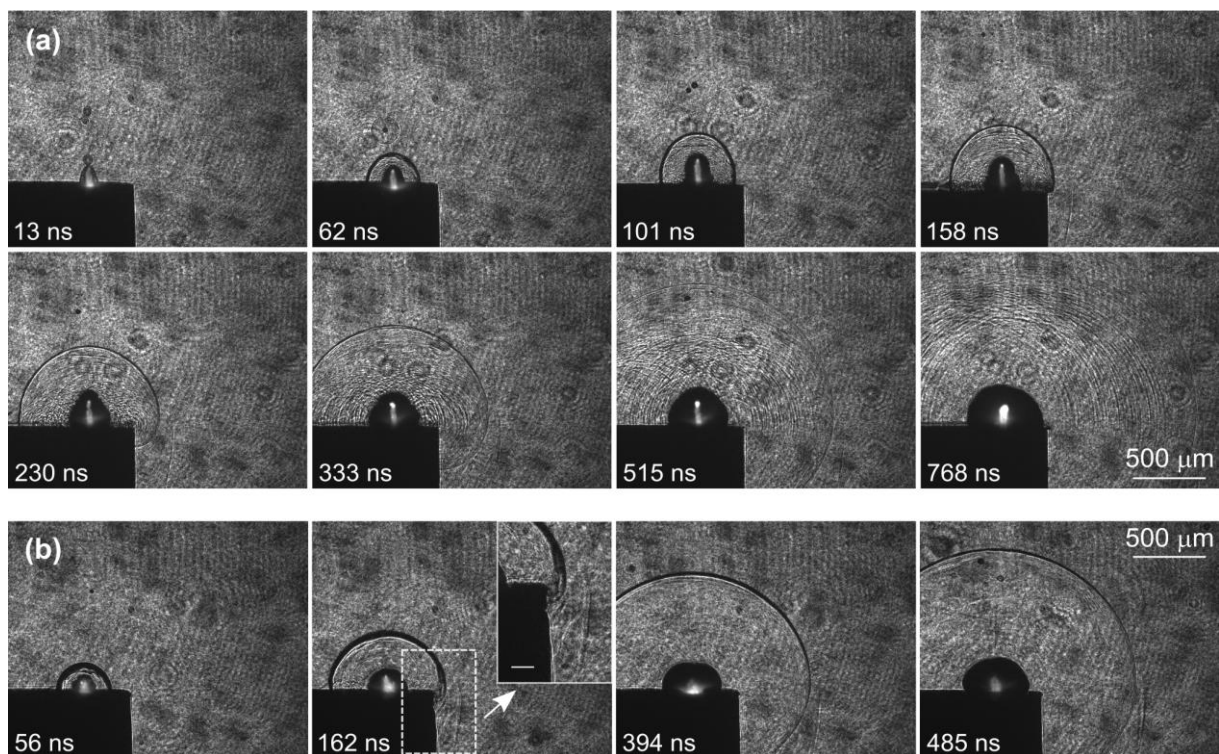


Fig. S13. Shockwave evolution over the edge of the stainless steel sample after laser pulse irradiation at $l = 0.3$ mm from the edge. Surrounding liquids are (a) water and (b) PEG. Pulse energy equals 10.6 mJ. White line in the inset image at 162 ns marks 100 μm .

S3.1 Evaluation of shockwave dynamics

The shockwave radius R_s as a function of time t after the excitation-laser pulse was measured by fitting a circle to the shock wave front that is visible as a thin dark ring in Fig. S13. Slight deviations of the pulse-to-pulse repeatability due to pulse energy variation and/or variation in the optical breakdown do not allow to calculate shockwave velocity by direct derivation of the measured radii that are shown by the dots in Fig. S14. To make this possible, the measured radii were fitted by using the following curve:

$$R_s = R_0 \left[n^{\frac{n}{1-n}} \left(\left(n^{\frac{-1}{1-n}} \left(\frac{c_0}{R_0} t \right) + 1 \right)^n - 1 \right) \right]^{1/n}, \quad (\text{S12})$$

where the characteristic radius R_0 , the speed of sound c_0 , and n , are free fitting parameters. The fitting curve given by Eq. (S12) is derived from the Jones's [S3] generalized trajectory for blast waves with proper limit for the strong blast waves, when $t \rightarrow 0$, $R_s \rightarrow \left(R_0^{\frac{n-1}{n}} c_0^{\frac{1}{2}} t \right)^{1/n} \propto t^{1/n}$ as well as for the acoustic waves, i.e., when $t \rightarrow \infty$, $R_s \rightarrow c_0 t$. The fitted curves [Eq. (S12)] are shown by the solid lines in Fig. S14. The fitted free parameters are listed in Table S2.

The goodness of fit was evaluated as the average relative difference between the measured and fitted value through the following equation:

$$\sigma = \frac{1}{N} \sqrt{\sum_{i=1}^{i=N} \left(\frac{\Delta R_i}{R_{i,\text{fit}}} \right)^2}, \quad (\text{S13})$$

where ΔR_i stands for the radius difference between the i -th measurement (point) and the fitted radius $R_{i,\text{fit}}$ at the same time and N equals the number of the all measured points. For shockwave radius in water and PEG, this average relative difference was estimated to $\pm 1\%$ and $\pm 0.9\%$, respectively.

From the temporal evolution of the shockwave radius, its velocity u_s can be determined simply by deriving

$$u_s = \frac{dR_s}{dt} . \quad (\text{S14})$$

Results for the shockwave velocity in water and PEG are presented in Fig. S15.

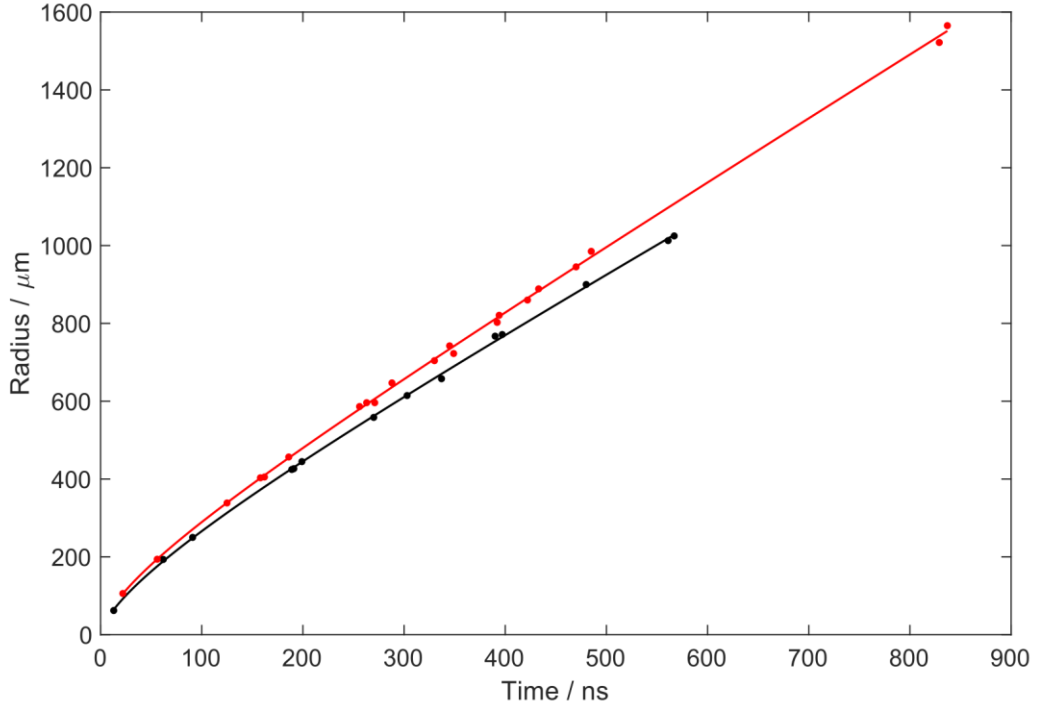


Fig. S14. Shockwave front radius with respect to time after breakdown in water (black) and PEG (red). Dots represent experimentally determined values, while solid lines show the curves fitted by Eq. (S12).

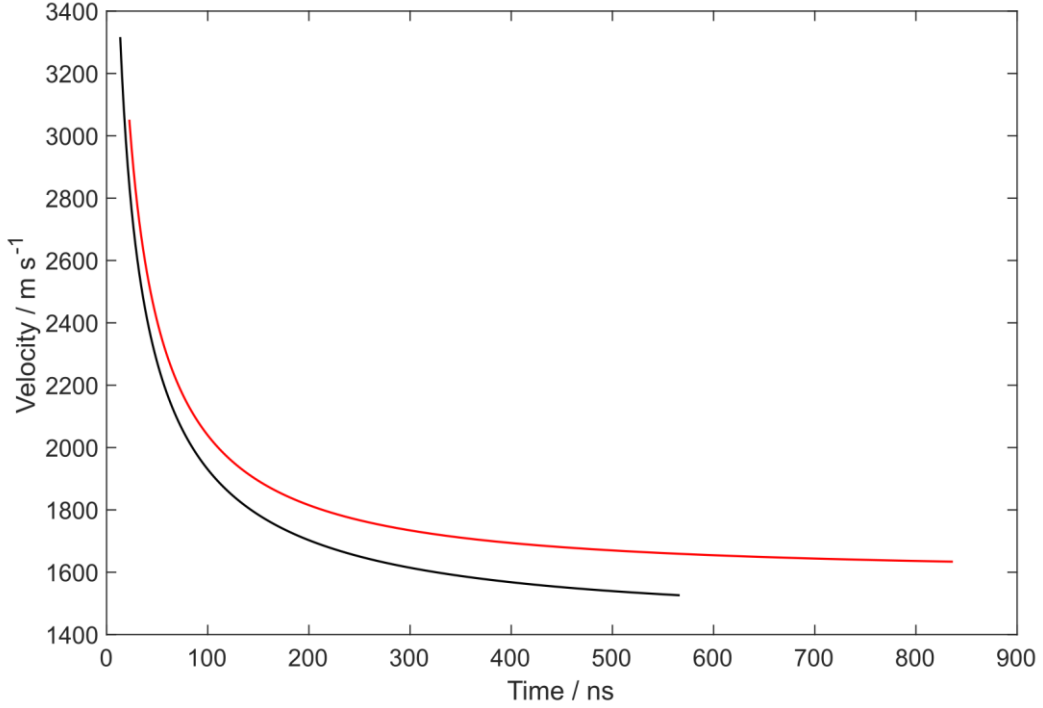


Fig. S15. Shockwave propagation velocity with respect to time after breakdown in water (black) and PEG (red). Curves are derived from the fitted curves in Fig. S14 by using Eq. (S14).

S3.2 Evaluation of bubble dynamics

With the experimental setup #2, we captured single images of bubbles from single excitation-laser pulses. In this way, we measured the radii of *individual* (different) bubbles as a function of time (the dots in Fig. S16). The first and second temporal derivative of radius as a function of time are needed to calculate the pressure difference (see Eq. (3) in the main text). Thus, we fitted the following curve (solid lines in Fig. S16) to the measured data:

$$R_b(t) = r_0 \left(\frac{t}{t_0} \right)^n. \quad (\text{S15})$$

Fitting parameters r_0 , t_0 , and n are listed in Table S2. The average relative difference between the measured bubble radius and its fitted value at the corresponding time [Eq. (S13)] was estimated to $\pm 3\%$ and $\pm 2\%$ in water and PEG, respectively. To calculate the pressure difference at the bubble wall, Δp , first and second derivative of the fitting curve [Eq. (S15)] should be calculated as

$$\begin{aligned}\dot{R}_b(t) &= \frac{r_0 n}{t_0^n} t^{n-1} \\ \ddot{R}_b(t) &= \frac{r_0 (n^2 - n)}{t_0^n} t^{n-2}.\end{aligned}\tag{S16}$$

Thereby, the pressure difference can be estimated from the fitted data as:

$$\Delta p = \rho_0 \frac{r_0^2 n^2}{t_0^{2n}} \left(\frac{5}{2} - \frac{1}{n} \right) t^{2n-2}\tag{S17}$$

Figure S17 shows the velocity of the bubble wall as a function of time, calculated from the first equation in Eq. (S16). Pressure as a function of time is shown in Fig. S18, while Fig. S19 shows the pressure as a function of radius.

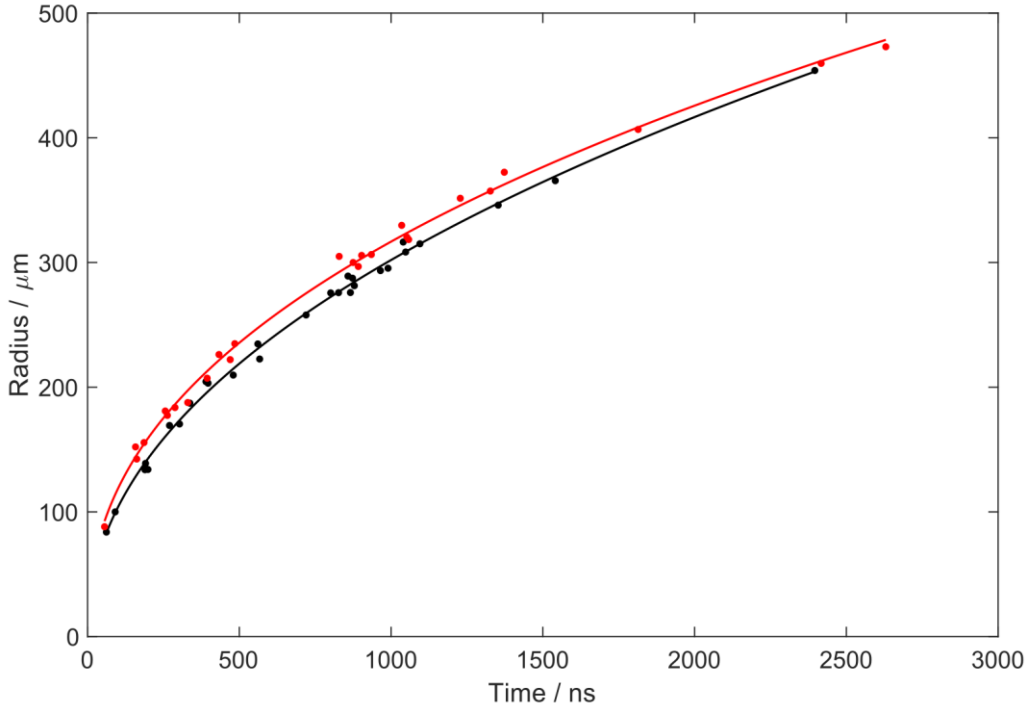


Fig. S16. Bubble radius with respect to time after breakdown in water (black) and PEG (red). Dots represent experimentally determined values, while solid lines show the curves that are fitted by using Eq. (S15).

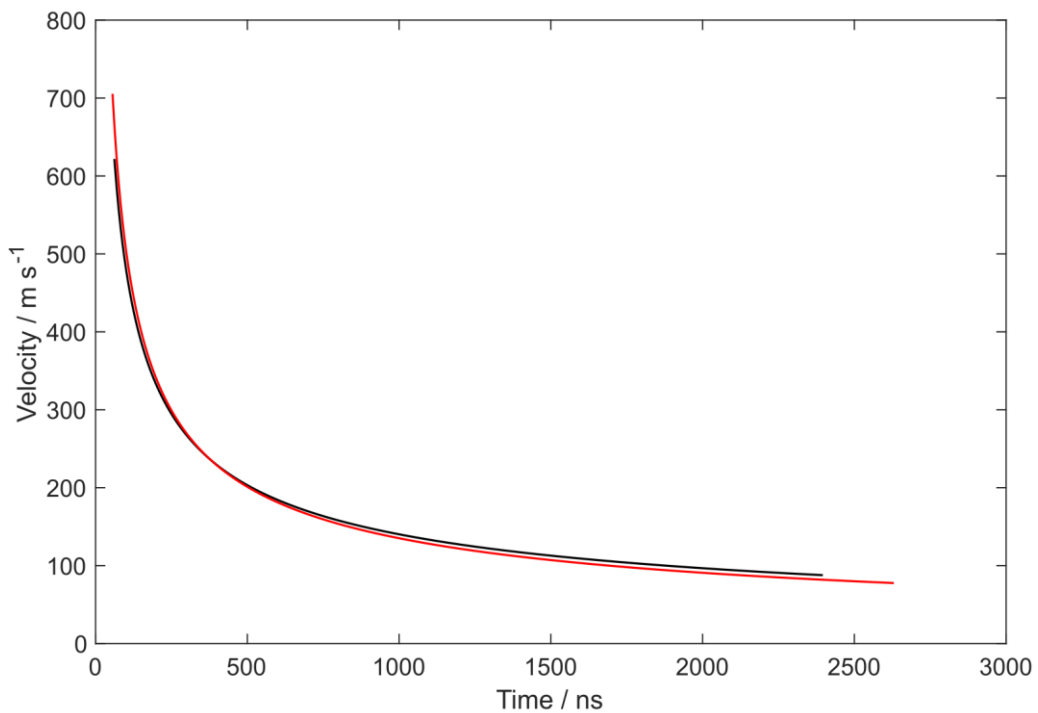


Fig. S17. Bubble wall velocity as a function of time after breakdown in water (black) and PEG (red).

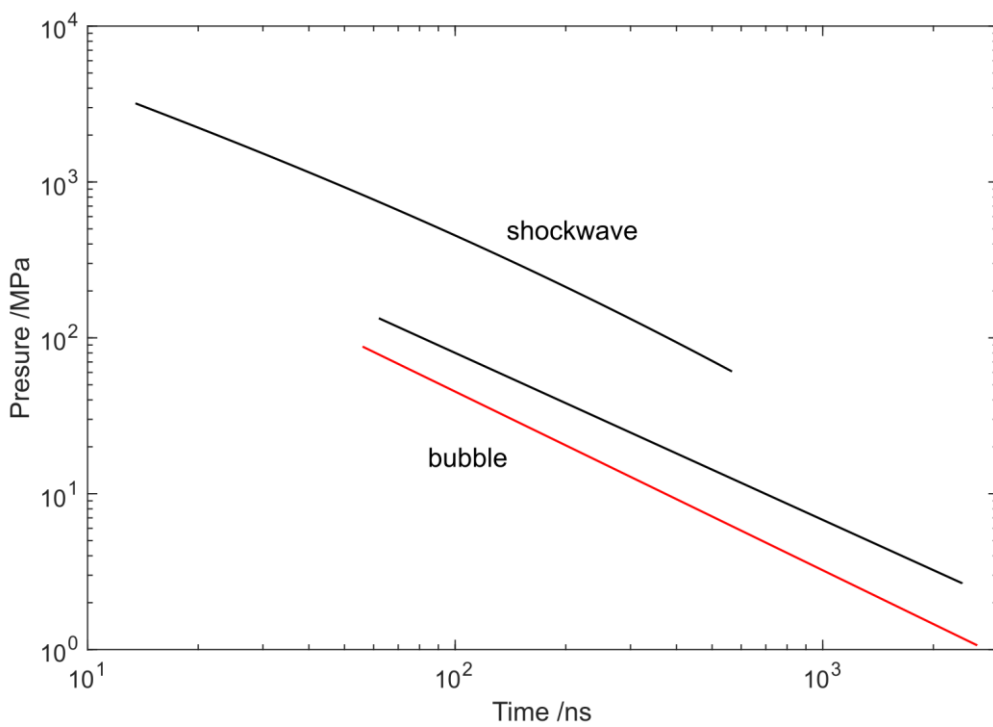


Fig. S18. Pressure at the shockwave front and at the bubble wall as a function of time after breakdown in water (black) and PEG (red).

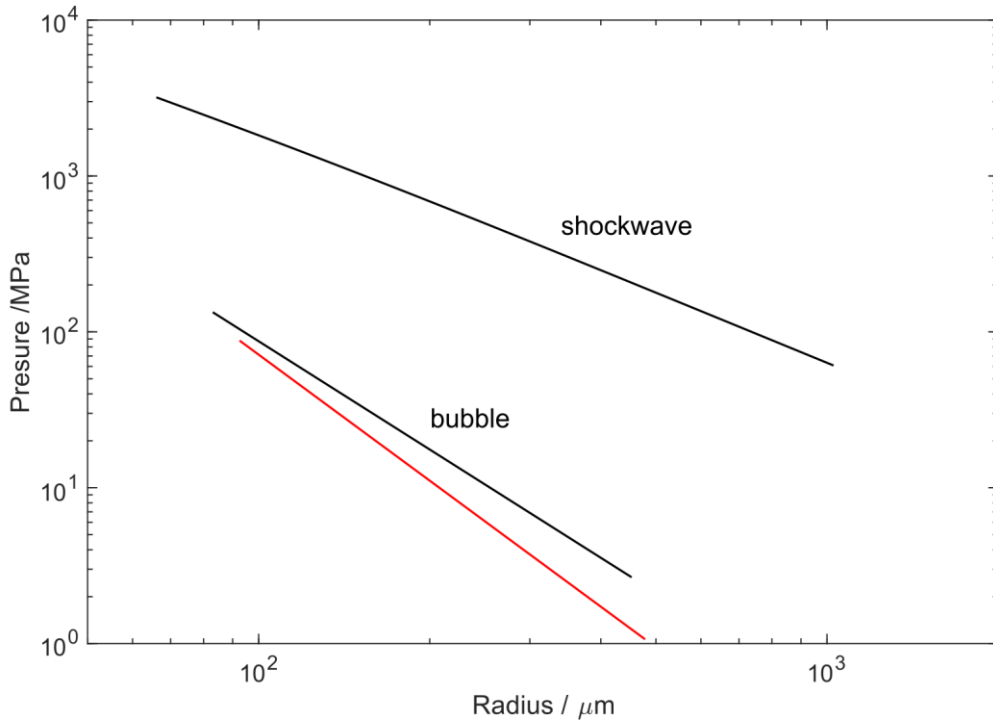


Fig. S19. Pressure at the shockwave front and at the bubble wall as a function of radius in water (black) and PEG (red).

Table S2. Free fitting parameters obtained by fitting Eqs. (S12) and (S15) to the experimental measurements of shockwave and bubble radii.

Liquid	Shockwave – Eq. (S12)			Bubble – Eq. (S15)		
	$R_0 / \mu\text{m}$	$c_0 / \text{km s}^{-1}$	n	$r_0 / \mu\text{m}$	t_0 / ns	n
Water	752.6	1.44	0.99	9.75	0.62	0.46
PEG	592.2	1.60	1.22	14.77	0.76	0.43

S4 Development of secondary cavity

In this section, we present the side observation of dynamics occurring $\pm 4 \mu\text{s}$ after formation (inception) of the secondary cavity. The point of inception was determined manually by finding the first frame within video with a visible secondary cavity. In Figs. S20-S28, this frame is shown in the third consecutive image of each row. The number on the top of these images denotes the liquid flow velocity over the edge at this instance. Time in the left bottom corner denotes time after breakdown. Values on the left of each row represent breakdown-edge distance l .

S4.1 Water

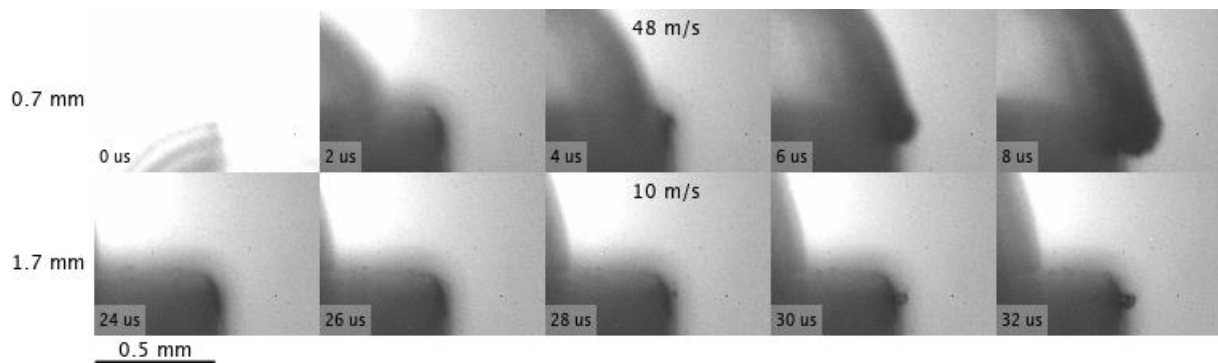


Fig. S20. Development of secondary cavity in water at 10 mJ pulse energy.

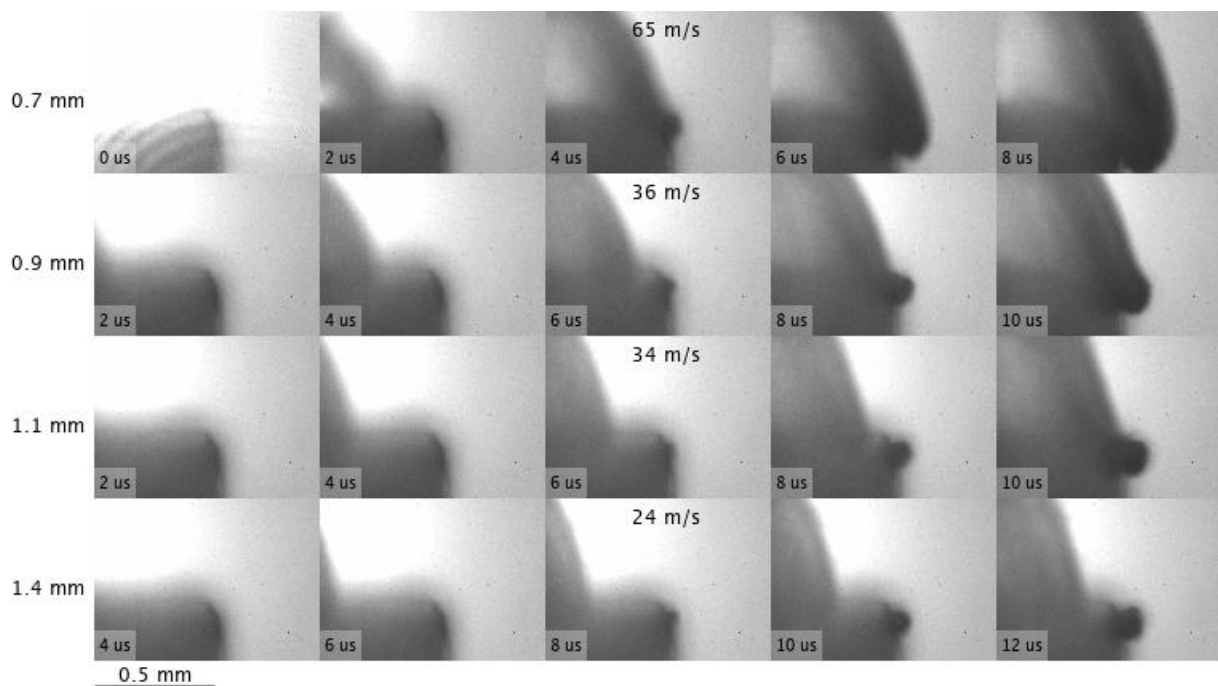


Fig. S21. Development of secondary cavity in water at 25 mJ pulse energy.

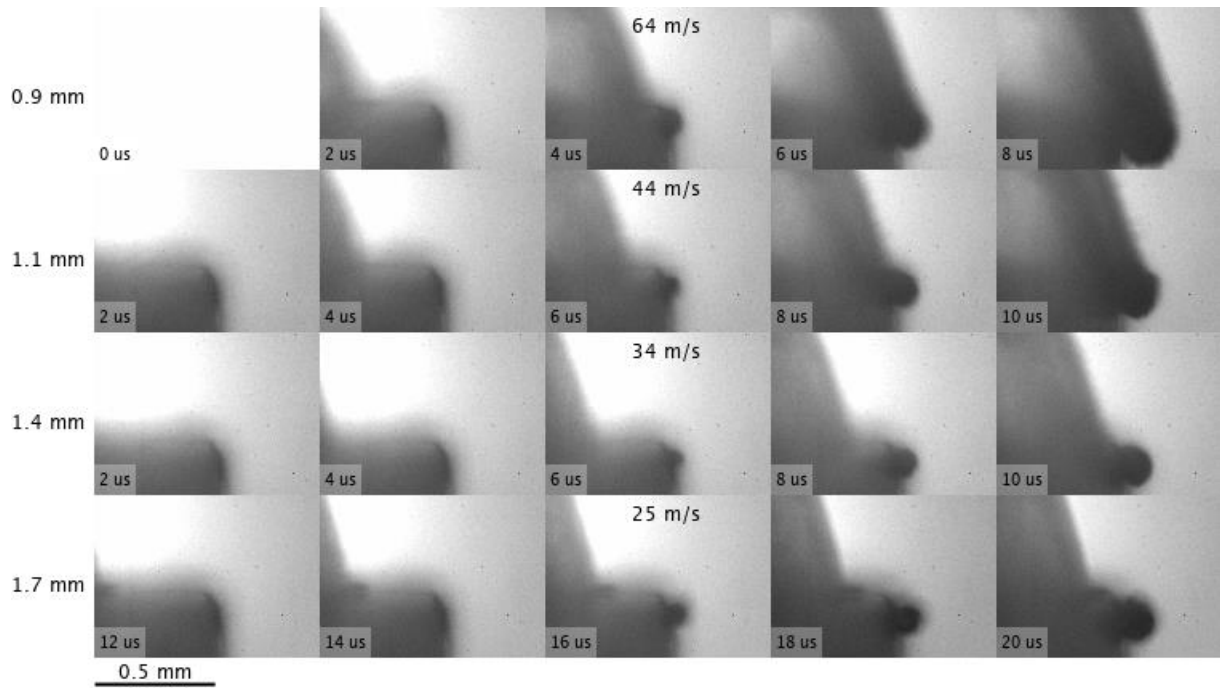


Fig. S22. Development of secondary cavity in water at 55 mJ pulse energy.

S4.2 Ethanol

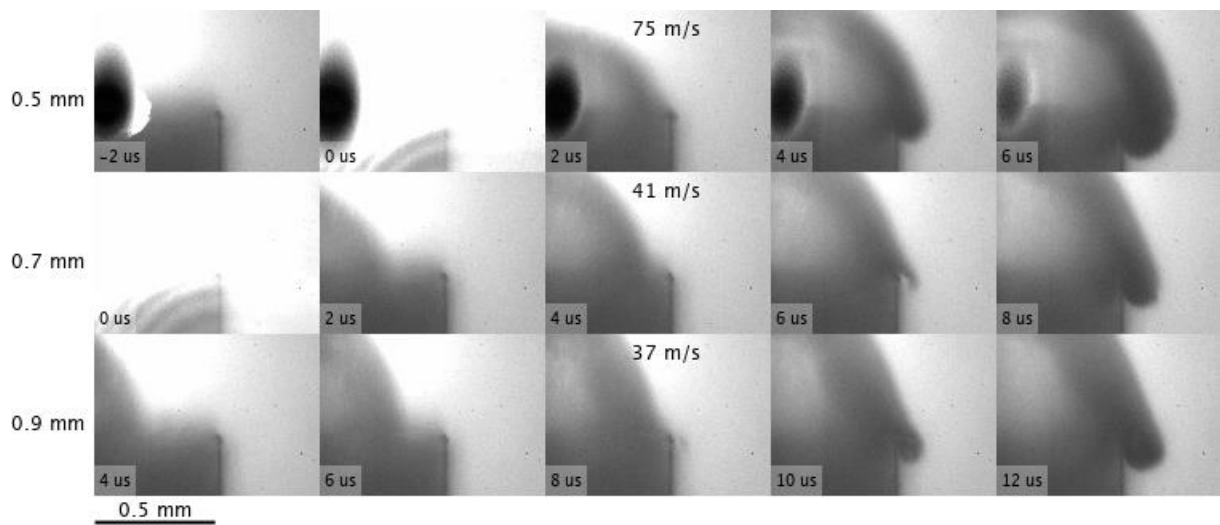


Fig. S23. Development of secondary cavity in ethanol at 10 mJ pulse energy.

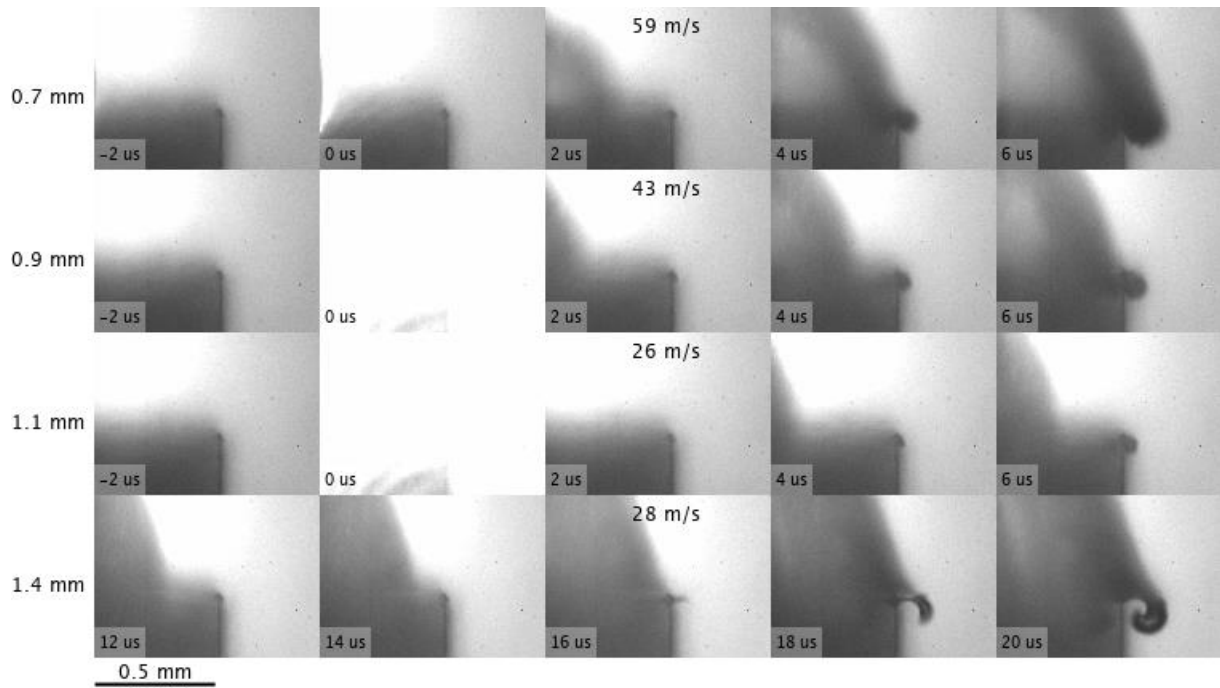


Fig. S24. Development of secondary cavity in ethanol at 25 mJ pulse energy.

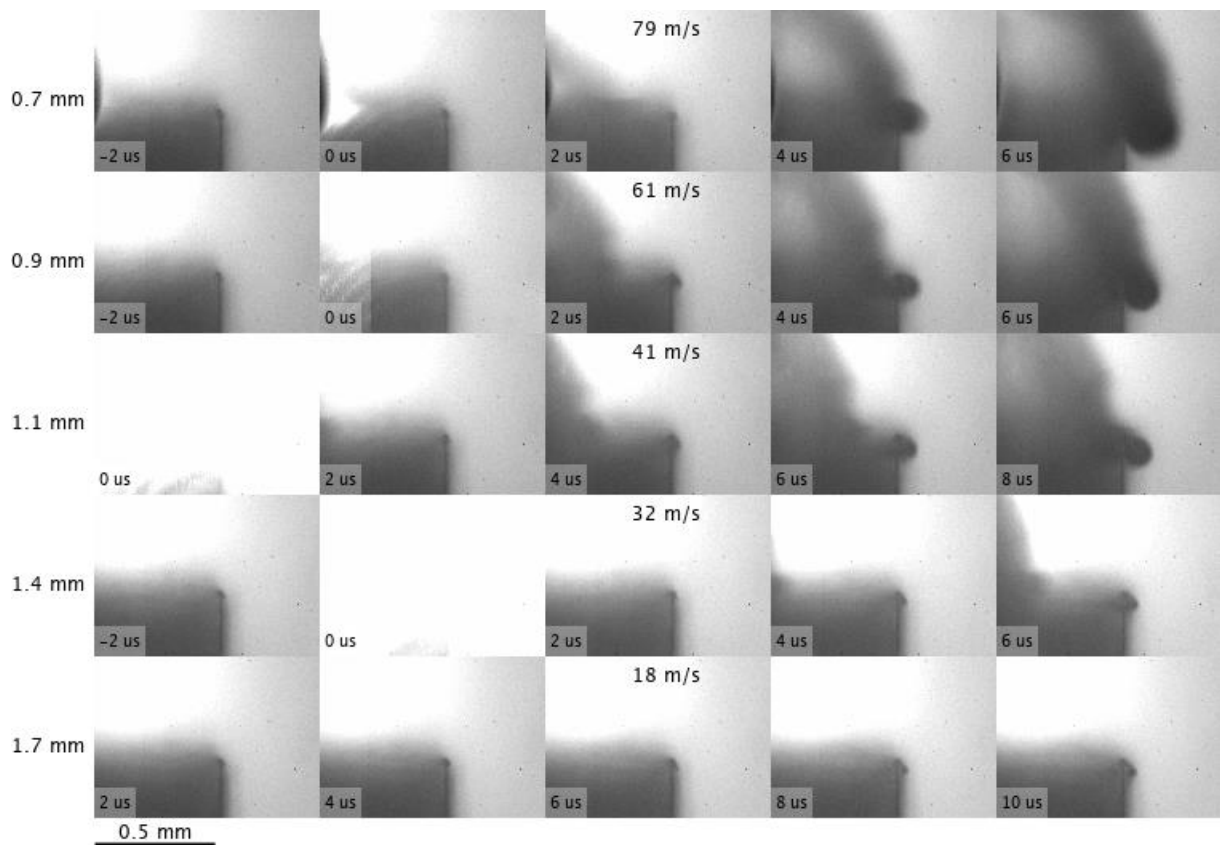


Fig. S25. Development of secondary cavity in ethanol at 55 mJ pulse energy.

S4.3 Polyethylene glycol

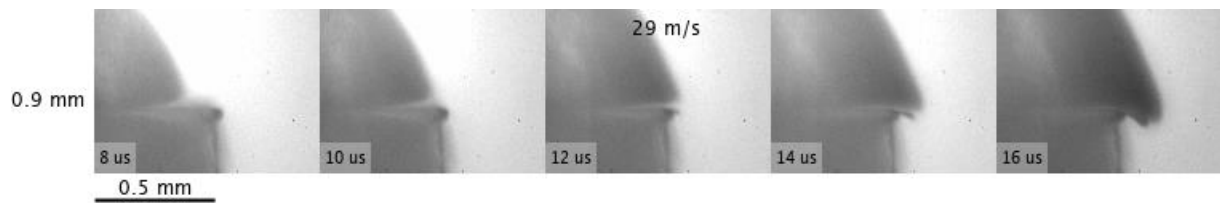


Fig. S26. Development of secondary cavity in PEG at 10 mJ pulse energy.

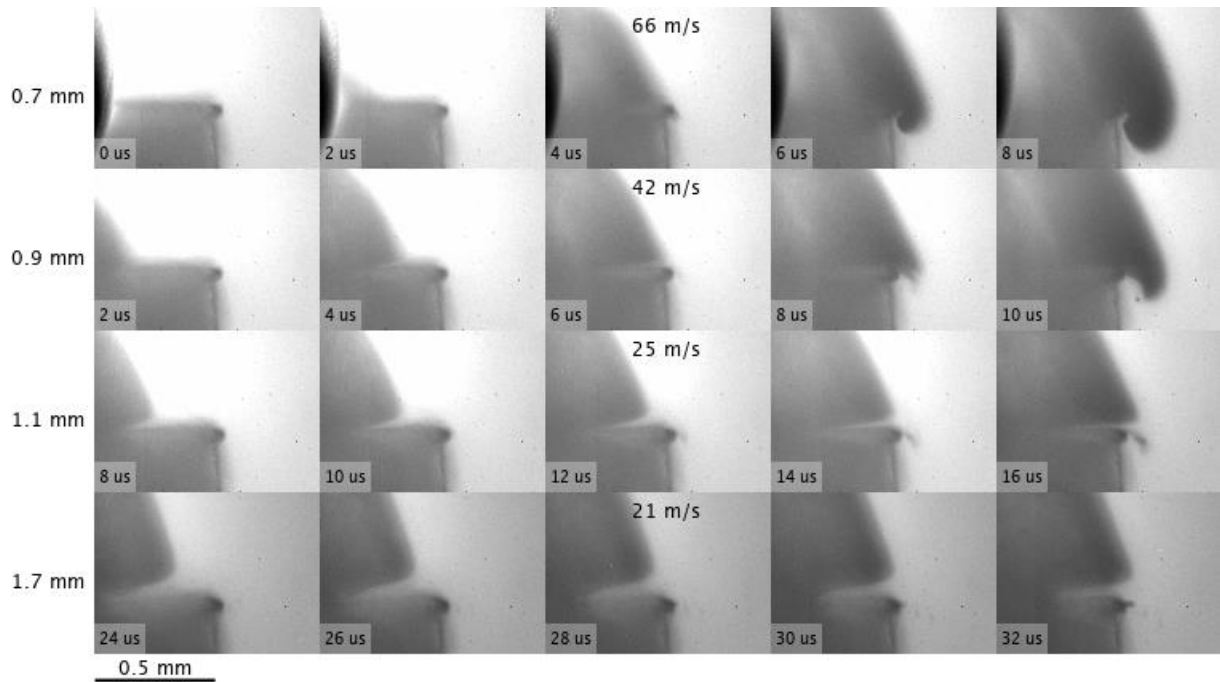


Fig. S27. Development of secondary cavity in PEG at 25 mJ pulse energy.

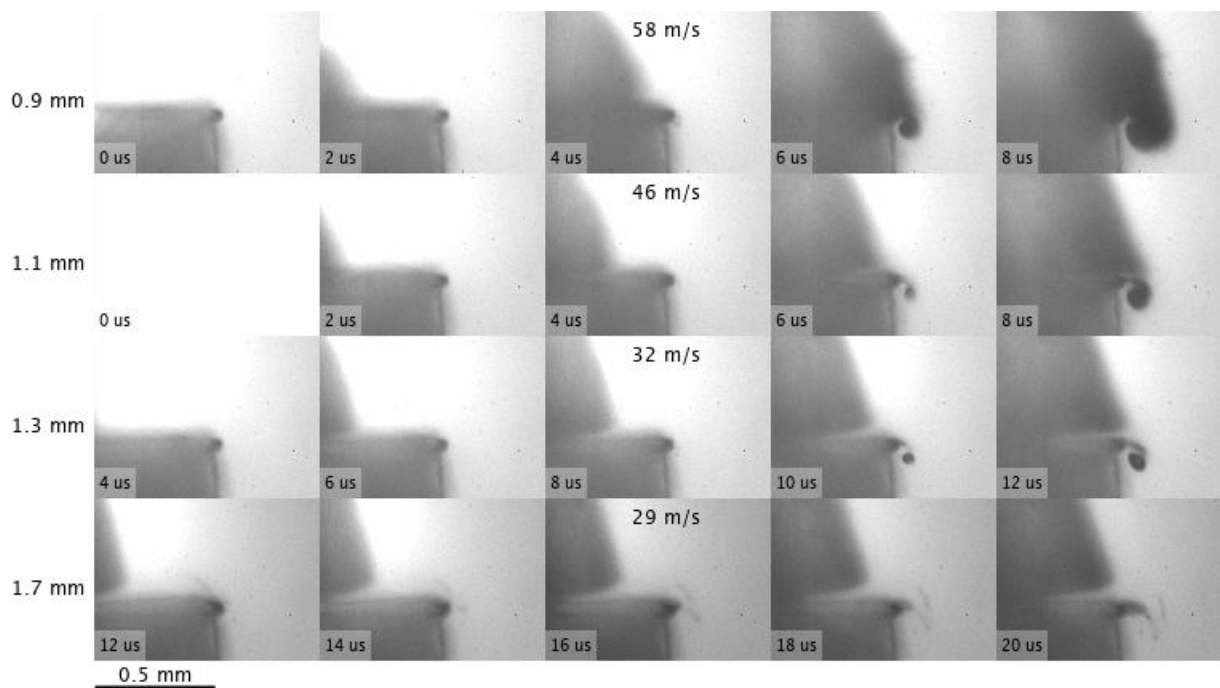


Fig. S28. Development of secondary cavity in PEG at 55 mJ pulse energy.

S5 Liquid injection into the cavitation bubble

This section shows the dynamics of laser-induced cavitation bubbles from either the front or the side, captured with an ultrafast camera (experimental setup #1). Images were captured at 500 kfps. Thus, the time between two consecutive frames equals $2 \mu\text{s}$. The image size equals $2.09 \times 1.74 \text{ mm}^2$.

S5.1 Observation from the side

Figure S29 shows the liquid injection in ethanol observed from the side, induced under the same conditions as those in Fig. 7c, i.e., $l = 0.9 \text{ mm}$ and 25 mJ pulse energy. Injection can be seen propagating at a slight angle with respect to the vertical sample surface. Injections that can be seen left of the marked injection in Fig. S29 at $120 \mu\text{s}$ result from the same phenomena that occur at the edge (horizontal dashed line of the sample mark) of the sample surface facing the ultrafast camera.

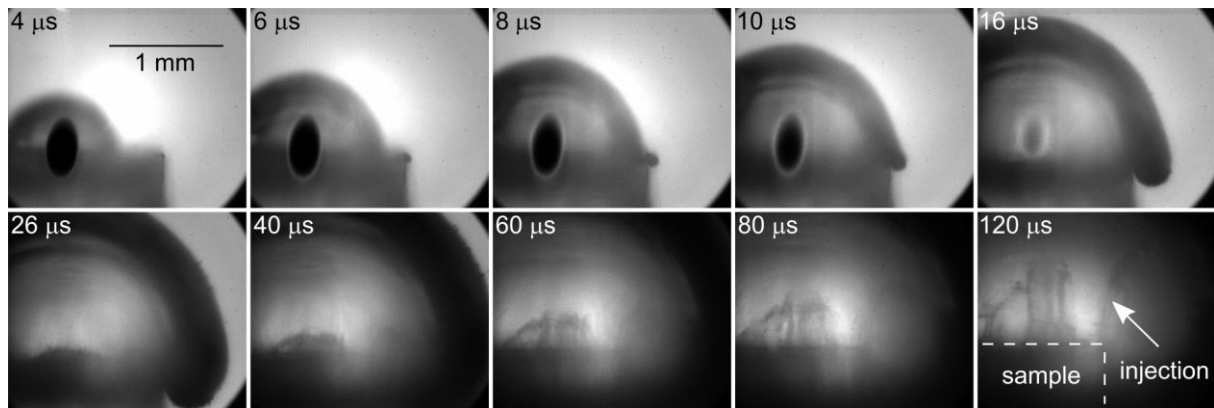


Fig. S29. Imaging of the liquid injection in ethanol from the side (same parameters as in Fig. 7c).

S5.2 Influence of surrounding liquid

Figure S30 shows comparison of bubble dynamics induced in water, ethanol, and PEG. Pulse energy equals 25 mJ, while $l = 0.9$ mm.

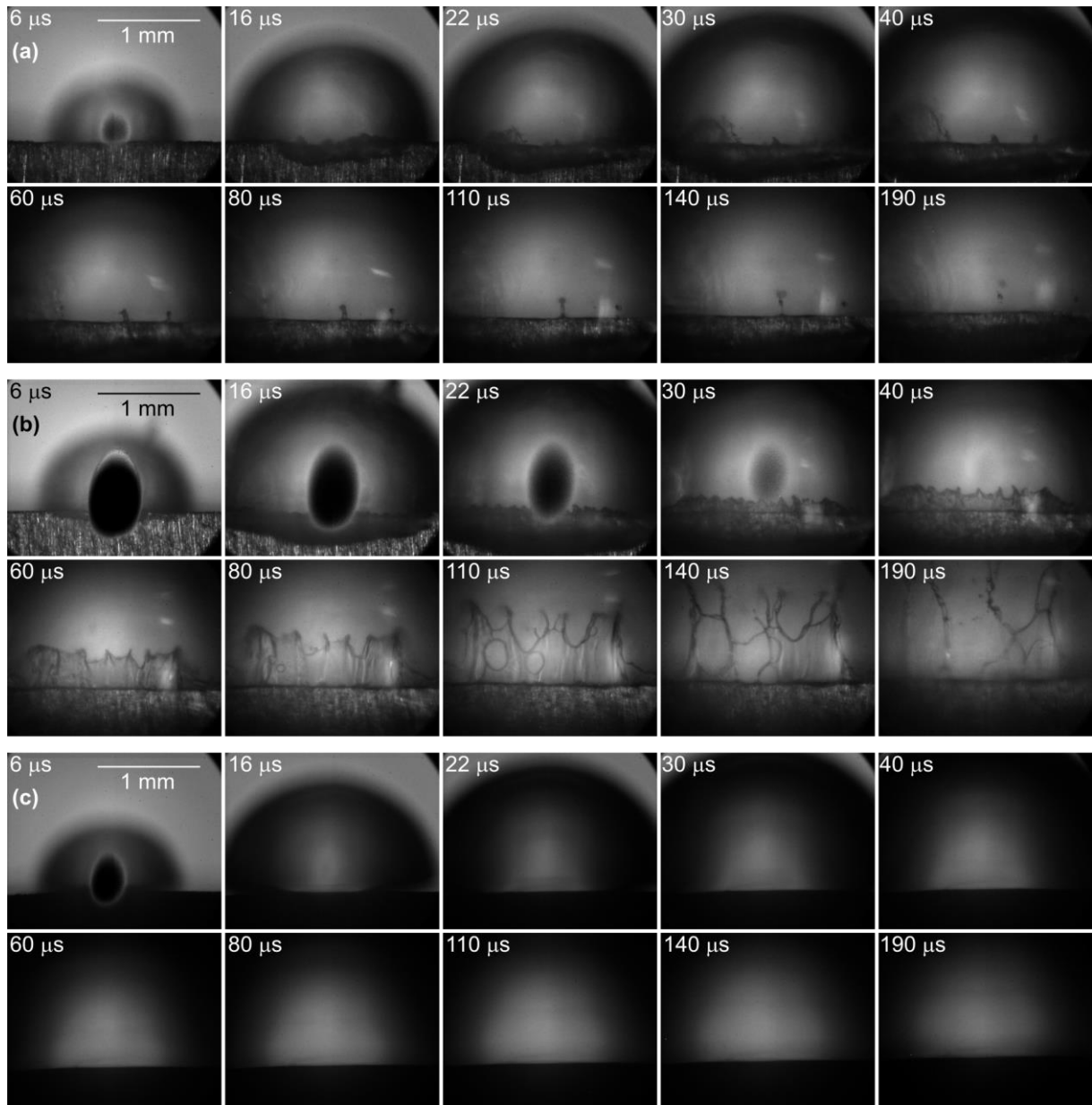


Fig. S30. Direct comparison of bubble dynamics induced in (a) water, (b) ethanol, and (c) PEG under same conditions. Image (c) is only illuminated from the back due to technical issues that could not be addressed in due time.

S5.3 Influence of breakdown-edge distance

Figure S31 shows the case when the distance between the breakdown and the edge is insufficient for visible liquid injection in water and ethanol.

Figure S32 shows an asymmetrical re-entrant injection that occurred at $l = 1.1$ mm in water at 25 mJ pulse energy.

Figure S33 supports Fig. 8 in the main paper. Full temporal evolution of each individual injection from the inset images in Fig. 8 is presented.

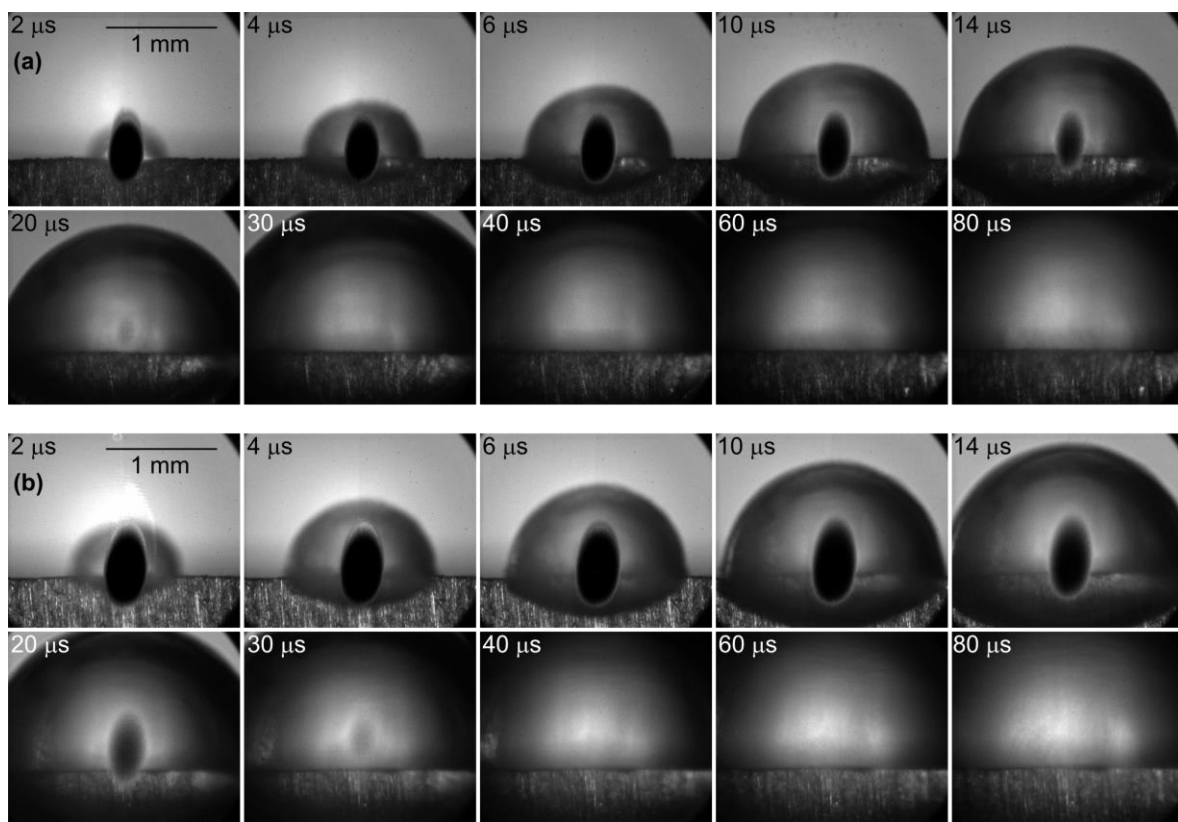


Fig. S31. Bubble dynamics of bubbles induced in (a) water ($l = 0.2$ mm) and (b) ethanol ($l = 0.3$ mm). Laser pulse energy equals 25 mJ.

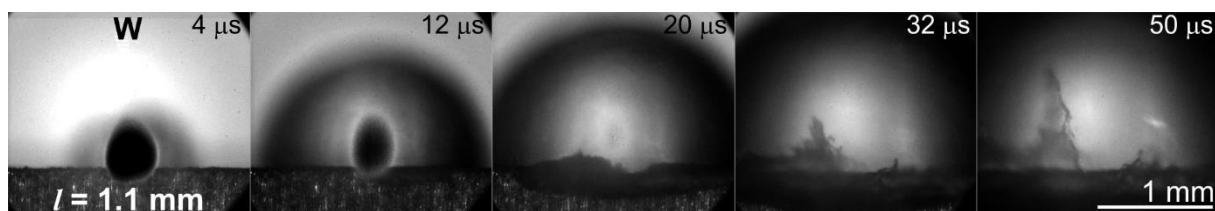


Fig. S32. Asymmetrical re-entrant injection dynamics in a bubble at $l = 1.1$ mm in water. Laser pulse energy equals 25 mJ.

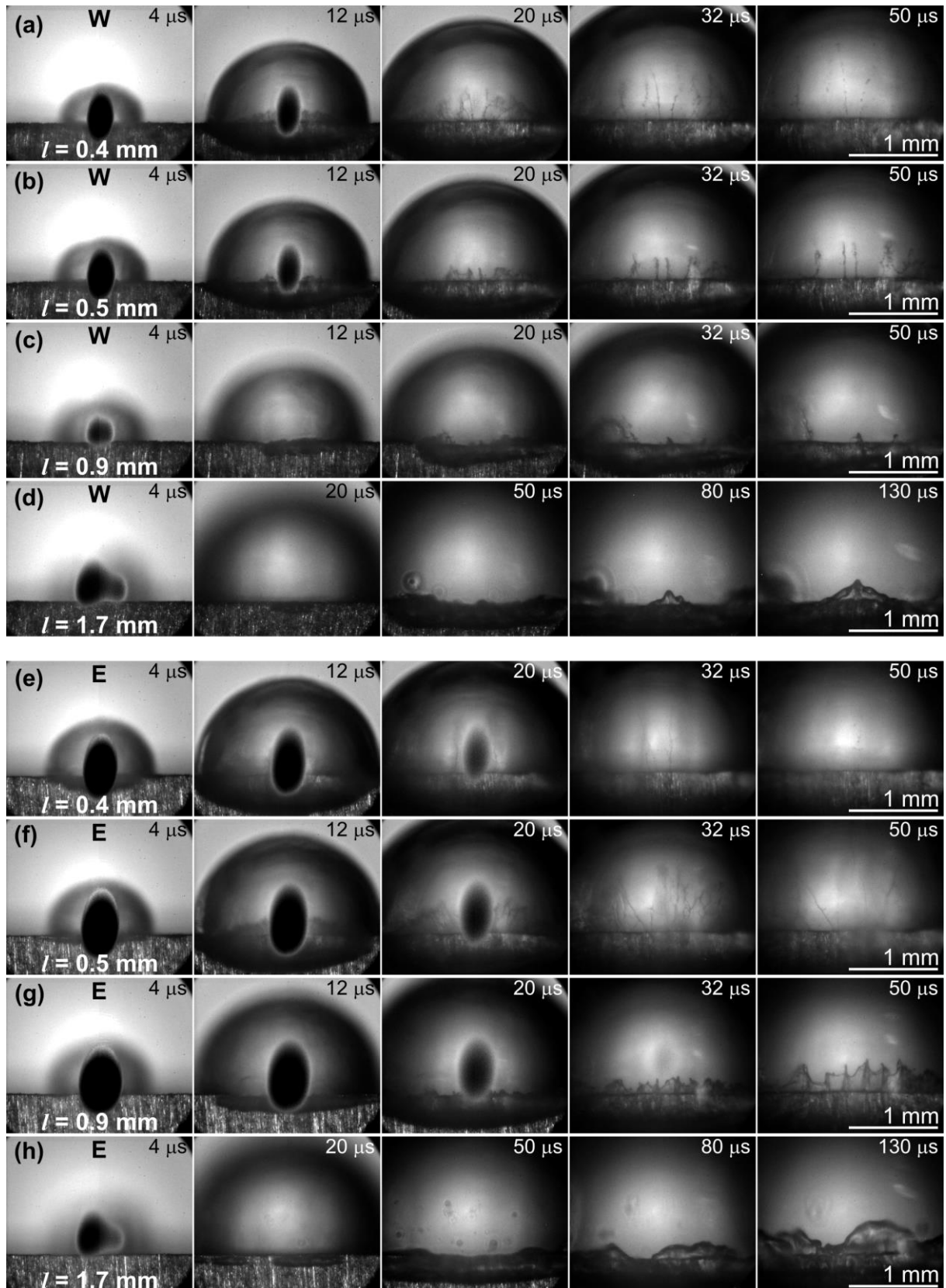


Fig. S33. Re-entrant injection dynamics in bubbles induced at $l = 0.4$ mm – 1.7 mm in (a-d) water and (e-h) ethanol. Laser pulse energy equals 25 mJ. Note the different time scale of (d) and (h) compared to others.

S5.4 Influence of pulse energy

Figures S34 and S35 show the influence of changing solely the pulse energy. As can be seen from Fig. S34 ($l = 0.3$ mm), increasing the pulse energy increases the jet velocity v_j and promotes more significant dispersion of the injection into smaller droplets (Fig. S34b, 40 μ s). Similar effect is observed when decreasing the breakdown-edge distance at constant pulse energy. Decreasing the pulse energy, on the other hand, also decreases the jet velocity (Fig. S35a). The latter is also observed when l is increased at constant pulse energy.

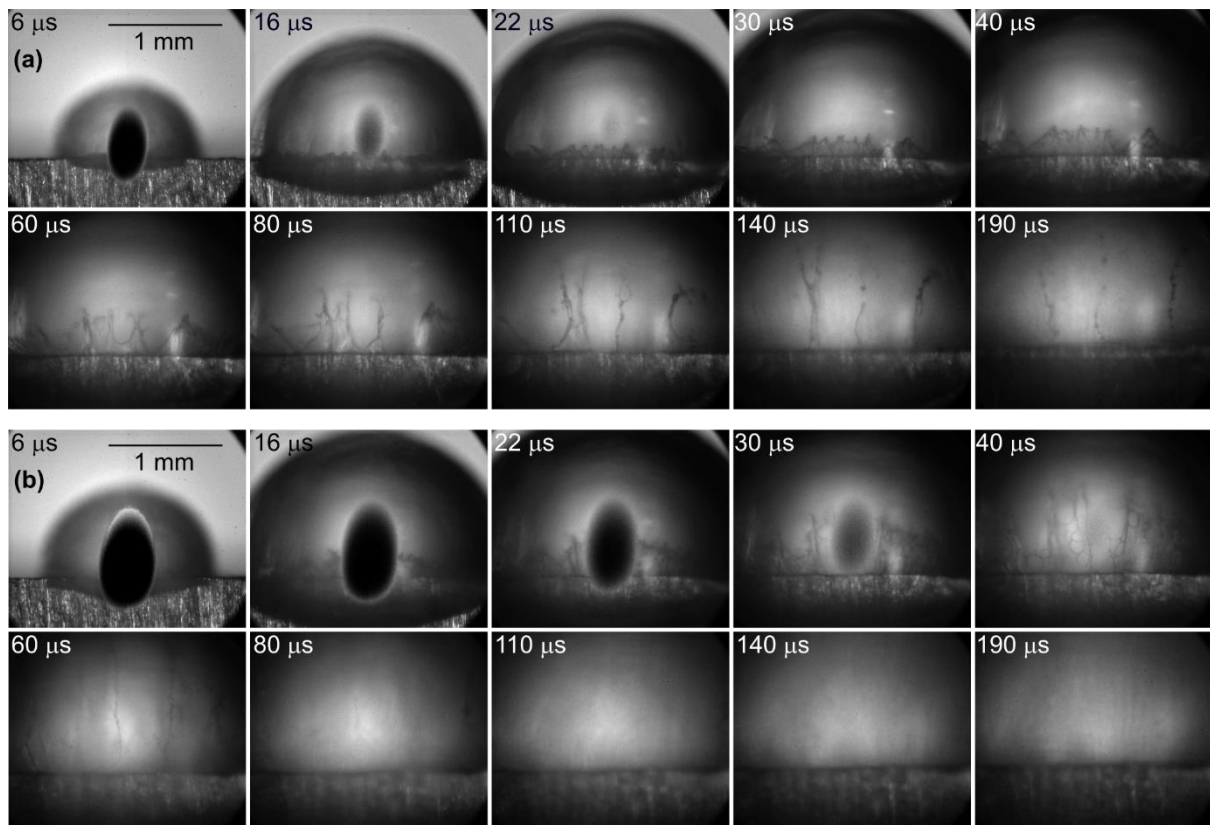


Fig. S34. Comparison of liquid injections in ethanol induced by laser pulses with pulse energies of (a) 10 mJ and (b) 25 mJ. Distance between the breakdown and the edge equals 0.3 mm.

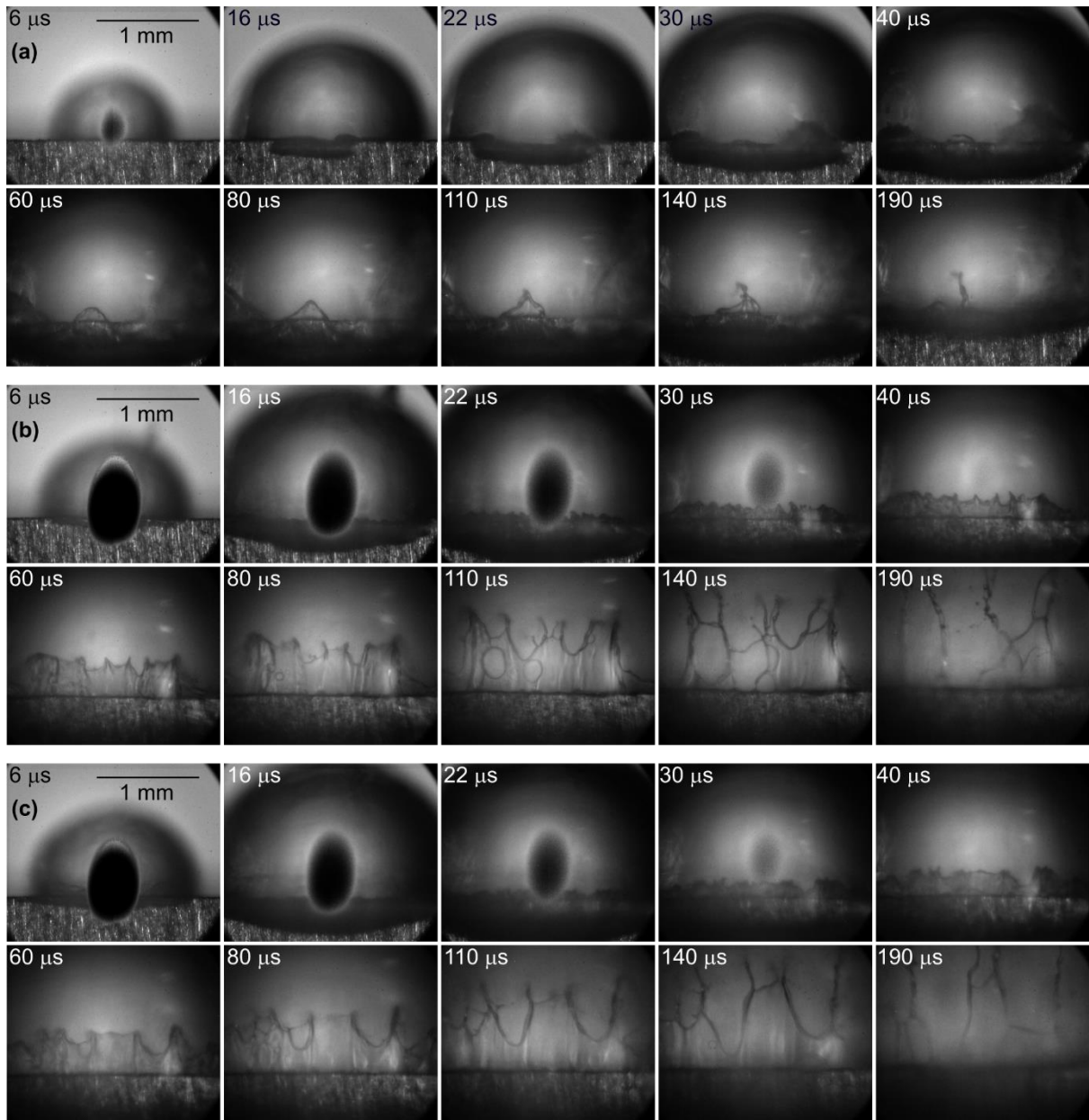


Fig. S35. Comparison of liquid injections in ethanol for pulse energies of (a) 10 mJ, (b) 25 mJ, and (c) 55 mJ. The breakdown-edge distance equals 0.9 mm.

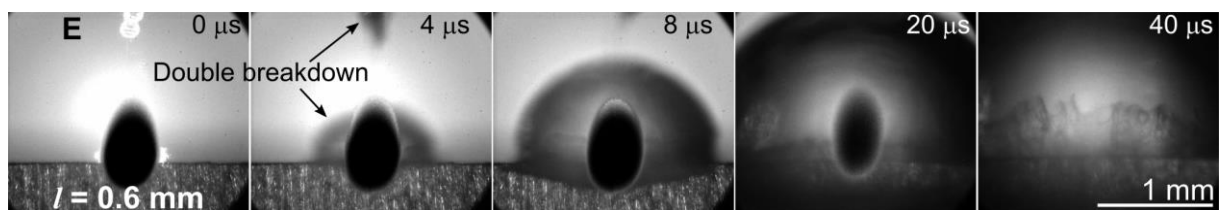


Fig. S36. Double breakdown in ethanol at pulse energy of 55 mJ and $l = 0.6$ mm.

S6 Influence of sample thickness

The effective distance between the position of breakdown and the edge was also varied by changing the thickness of the sample, denoted by d in Fig. S1. In this case, we clamped the sample in an “H” configuration (Fig. S1a) and the breakdown was induced in the middle of the sample, meaning $l = a = d/2$ according to notation in Fig. S1a.

The energy of the cavitation bubble in Fig. S37a is significantly lower due to smaller sample width compared to the laser spot size. Similarly to the already presented results of the influence of the breakdown-edge distance, the jet only appears when this distance is in the order of a few hundred micrometers, as seen in Fig. S37c. However, in this case, the “threshold” thickness of the sample, that is required for formation of liquid injection into the cavitation bubble, was not determined with good accuracy since we had no foil samples with thicknesses between 0.38 mm and 1 mm. Nevertheless, we presume that the mechanism of the jet formation is similar to that with the breakdown not induced in the middle of the sample, concluding that the jets at these laser parameters should occur at sample thicknesses exceeding ~ 0.6 mm (thickness equal to the shortest breakdown-edge distance of the detected injections, multiplied by two).

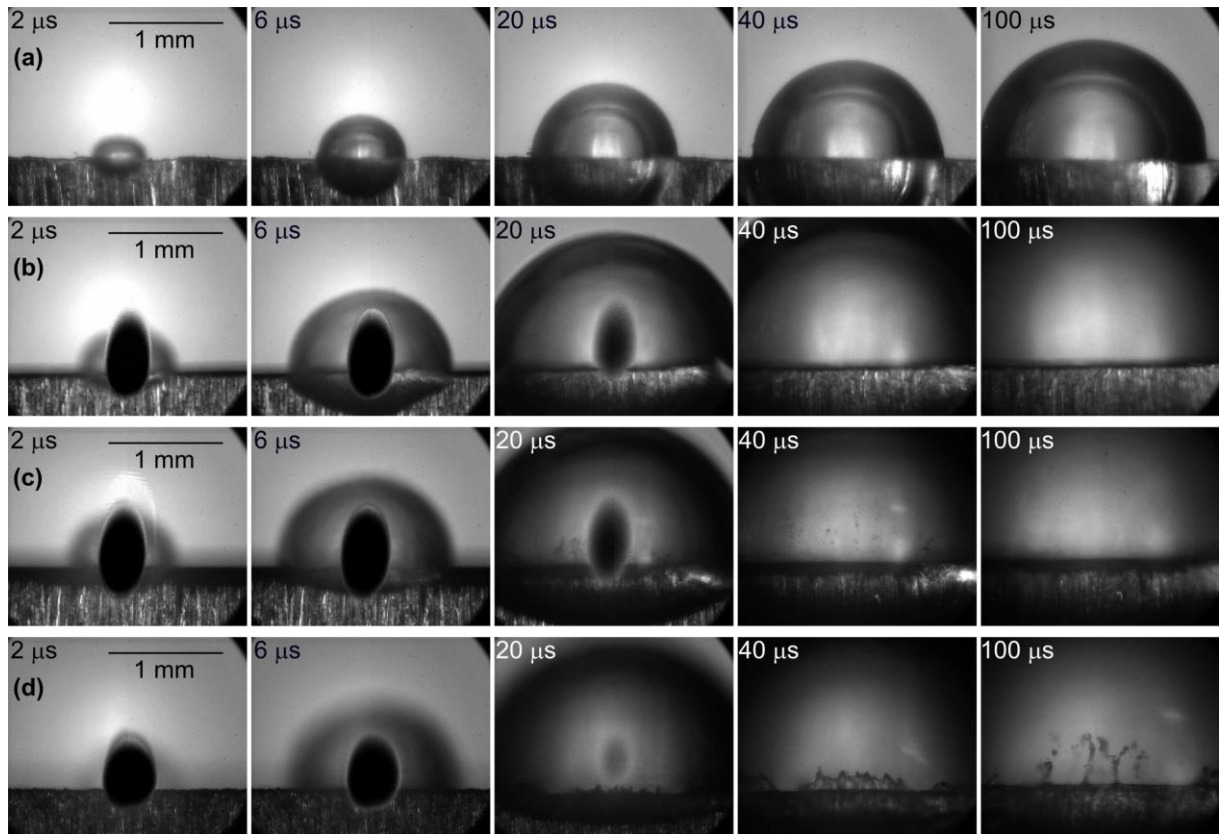


Fig. S37. Comparison of the bubble dynamics in water at different thicknesses of the samples. Pulse energy equals 25 mJ. Breakdown is induced in the middle of the sample with thickness of (a) 25 μm , (b) 0.38 mm, (c) 1 mm, and (d) 2 mm.

References

[S1] M. Born, E. Wolf, Principles of optics: electromagnetic theory of propagation, interference and diffraction of light, Elsevier, 2013.

[S2] C. Bongiovanni, A. Dominguez, J.-P. Chevillier, Understanding images of bubbles, European Journal of Physics, 21 (2000) 561-570. <https://doi.org/10.1088/0143-0807/21/6/307>

[S3] D.L. Jones, Intermediate Strength Blast Wave, The Physics of Fluids, 11 (1968) 1664-1667. <https://doi.org/10.1063/1.1692177>.